

# Mathematical Modelling of Solar Plasma Jets

JOSEPH SCALISI

Supervised by Professor ROBERTUS ERDÉLYI

and Professor MICHAEL RUDERMAN



University of Sheffield

School of Mathematics and Statistics

Submitted March 2023 for the degree of

Doctor of Philosophy



---

## Acknowledgements

---

I would like to give thanks to my two excellent supervisors: to Prof. Robertus Erdélyi, whose constant encouragement and support allowed me to become a better researcher and to persevere through difficult times, and who introduced me to the world of solar physics in the first place; and to Prof. Michael Ruderman, whose expertise and guidance was invaluable during my PhD.

Thank you also to my examiners, Prof. Andrew Hillier and Dr. Yi Li, whose comments were very much appreciated and have greatly improved this thesis.

I owe a great deal to my partner, Xander. Thank you for standing by me and creating a home for us in Sheffield despite everything, and for being so patient and supportive — especially during the process of writing this thesis.

Thank you to my friends, Poppy, Hope, James, Vinh, Elliot, Matt, Gaspard, Max, Callum, and all of the other wonderful people I have met during my time here, for making the PhD journey so much more bearable. I have enjoyed our climbing sessions, walks, and fun lunches, and I appreciated the frequent excuses for procrastination via crosswords and increasingly complex forms of Wordle. Thanks to Noemi and Tamás for your help in the early days of my academic journey. Thanks also to my friends elsewhere, for offering respite from PhD work and for the good times we have shared.

To my family, thank you for your belief in me and for being an anchor for me to depend on, even when I don't visit as often as I should.

Finally, I wish to thank the University of Sheffield and the Science and Technology Facilities Council (STFC) for making this research possible.



---

## Declaration

---

I hereby declare that except where specific reference is made to the work of others, the contents of this dissertation are original and have not been submitted in whole or in part for consideration for any other degree or qualification in this, or any other university. This dissertation is my own work and contains nothing which is the outcome of work done in collaboration with others, except as specified in the text. This dissertation contains fewer than 80,000 words including appendices, bibliography, footnotes, tables and equations.

Joseph Scalisi,  
March 2023.



---

## Abstract

---

Solar jets have been studied for over 100 years and may hold the key to some of the most long-standing questions in solar physics. Analytical models are well established as a useful tool for examining solar phenomena, many of which exhibit magnetohydrodynamic wave behaviour. In this thesis we investigate a potential mechanism by which solar jets are formed and explore the connection between features such as spicules and magnetic bright points in the lower solar atmosphere.

A model is created, utilising a perturbation method and adapting the system of MHD equations in the context of a magnetic flux tube in order to explore the generation of mass flux due to torsional Alfvén waves. Using the zero-beta approximation to model these intensely magnetic regions, we derive that the presence of such waves can result in field-aligned plasma motion formed non-linearly as a result of the Lorentz force. Comparisons are made with observed properties of spicules.

In the next iteration we include a density discontinuity, representing the solar transition region. The initial upward-propagating Alfvén pulse is reflected from this discontinuity, resulting in a reversal of the flux which may be identified with the behaviour of spicules. The relative mass of plasma lifted by the transmitted and reflected waves is estimated as a ratio, and comparison is made between the relative total mass of spicules and the solar wind.

Finally, the model is augmented with a finite transitional layer in which the atmospheric density decreases exponentially. The Alfvén pulse interacts with and is partially reflected by this layer. We find that the wave transmitted into the upper solar atmosphere results in greater mass flux when compared with the previous model. We examine how varying the parameters of this transitional layer affects the ratio of the flux above and below the layer.

---

## List of publications

---

Parts of this Thesis are based on the following publications:

- Joseph Scalisi, William Oxley, Michael S. Ruderman, and Róbert Erdélyi. Propagation of Torsional Alfvén Pulses in Zero-beta Flux Tubes. *Astrophysical Journal*, 911(1):39, April 2021.
- Joseph Scalisi, Michael S. Ruderman, and Róbert Erdélyi. Reflection and Evolution of Torsional Alfvén Pulses in Zero-beta Flux Tubes. *Astrophysical Journal*, 922(2):118, December 2021.
- Joseph Scalisi, Michael S. Ruderman, and Róbert Erdélyi. Generation of Vertical Flows by Torsional Alfvén Pulses in Zero-beta Tubes with a Transitional Layer. *Astrophysical Journal*, 951(1):60, July 2023.

The following publication is not included in this Thesis:

- William Oxley, Joseph Scalisi, Michael S. Ruderman, and Róbert Erdélyi. Formation of Chromospheric Spicules in Magnetic Bright Points: An Analytical Approach Using Cartesian Slab Geometry. *Astrophysical Journal*, 905(2):168, December 2020.



---

# Contents

---

<b>List of figures</b>	<b>xiv</b>
<b>1 Introduction</b>	<b>1</b>
1.1 The Sun . . . . .	1
1.2 Solar Interior . . . . .	2
1.3 Solar Atmosphere . . . . .	3
1.3.1 Photosphere . . . . .	3
1.3.2 Chromosphere . . . . .	5
1.3.3 Corona . . . . .	7
1.4 Magnetohydrodynamics . . . . .	9
1.4.1 Solar Plasma . . . . .	10
1.4.2 Electromagnetic equations . . . . .	11
1.4.3 Induction Equation . . . . .	12
1.4.4 Plasma equations . . . . .	13
1.4.5 Plasma Beta . . . . .	14
1.4.6 Linear MHD . . . . .	14
1.5 MHD in the Solar Atmosphere . . . . .	16
1.6 Jets . . . . .	17
1.6.1 Spicules and Chromospheric Jets . . . . .	18
1.6.2 Generation of Jets . . . . .	21
1.7 Thesis Outline . . . . .	22

---

<b>2</b>	<b>Propagation of Torsional Alfvén Pulses in Zero-<math>\beta</math> Flux Tubes</b>	<b>25</b>
2.1	Background and motivation . . . . .	26
2.2	Model . . . . .	28
2.2.1	Physical Considerations . . . . .	29
2.2.2	The MHD framework . . . . .	31
2.2.3	First-order approximation . . . . .	32
2.2.4	Second-order approximation . . . . .	33
2.3	General case . . . . .	34
2.3.1	Radial velocity perturbation . . . . .	35
2.3.2	Perturbation of total pressure . . . . .	36
2.3.3	Boundary conditions . . . . .	37
2.3.4	Vertical velocity perturbation . . . . .	38
2.3.5	Inverse Laplace transform for the external region solution	39
2.4	Zero-beta approximation . . . . .	42
2.4.1	Relating to the general case . . . . .	44
2.4.2	Example solution and restrictions . . . . .	44
2.4.3	Results . . . . .	45
2.5	Discussion . . . . .	47
<b>3</b>	<b>Reflection and Evolution of Torsional Alfvén Pulses</b>	<b>53</b>
3.1	Background and motivation . . . . .	54
3.2	Reflected wave model . . . . .	55
3.2.1	Model formulation . . . . .	56
3.2.2	First-order approximation . . . . .	58
3.2.3	Second-order approximation . . . . .	61
3.3	Mass flux . . . . .	63
3.4	Pulse example . . . . .	63
3.5	Restrictions . . . . .	66
3.6	Discussion . . . . .	70
<b>4</b>	<b>Torsional Alfvén Pulses with a Transitional Layer</b>	<b>73</b>
4.1	Background and motivation . . . . .	74
4.2	Transitional layer model . . . . .	75
4.3	First-order approximation . . . . .	77

---

4.3.1	Fourier transform . . . . .	78
4.3.2	Inverse Fourier transforms . . . . .	81
4.4	Second-order approximation . . . . .	82
4.5	Mass flux ratio . . . . .	83
4.6	Discussion . . . . .	87
4.6.1	Alvén speed and density . . . . .	87
4.6.2	Thickness of the transitional layer . . . . .	88
4.6.3	Length of the pulse . . . . .	90
4.6.4	Limitations . . . . .	93
<b>5</b>	<b>Conclusions and future work</b>	<b>95</b>
5.1	Conclusions . . . . .	95
5.2	Future work . . . . .	97
	<b>Appendices</b>	<b>101</b>
	<b>A Verification of continuity of <math>V_{Z2}</math></b>	<b>101</b>
	<b>References</b>	<b>105</b>



---

## List of Figures

---

1.1	Diagram of the structure of the Sun . . . . .	2
1.2	Temperature and density of the solar atmosphere . . . . .	3
1.3	The photosphere . . . . .	6
1.4	Diagram of the solar atmosphere . . . . .	8
1.5	Spicules . . . . .	19
2.1	Flux tube . . . . .	30
2.2	Contour diagram . . . . .	41
2.3	Pulse example . . . . .	46
2.4	Pulse example $z$ and $r$ dependence . . . . .	46
2.5	Mass flux . . . . .	48
2.5	Mass flux (Caption) . . . . .	49
3.1	Flux tube with discontinuity . . . . .	57
3.1	Flux tube with discontinuity (Caption) . . . . .	58
3.2	Mass flux ratio . . . . .	64
3.3	Mass flux with reflection from discontinuity . . . . .	67
3.3	Mass flux with reflection from discontinuity (Caption) . . . . .	68
3.4	Wave interaction diagram . . . . .	69
4.1	Plot of the mass flux ratio $R$ against $\alpha$ . . . . .	86
4.2	Ratio with varying thickness of transitional layer and $\alpha$ . . . . .	89
4.3	Ratio with varying pulse duration and $\alpha$ . . . . .	91

4.3 Ratio with varying pulse duration and  $\alpha$  (Caption) . . . . . 92

# CHAPTER 1

---

## Introduction

---

### 1.1 The Sun

Throughout human history the Sun has been an object of great interest: once worshipped by ancient cultures around the world, it later became the literal centre of controversy when Copernicus presented his heliocentric model of the planets, and is still an influence on aspects of everyday life from the weather to satellite communications. The Sun is also a fascinating system of complex physical processes originating with the nuclear fusion reaction that is the source of the star's extreme heat and energy, causing atoms themselves to separate into ionised nuclei and electrons in the form of plasma. Far from being the static sphere that is apparent to the naked eye, even more interesting behaviour is exhibited by the constantly changing magnetic fields and charged plasma of the solar atmosphere, which is akin to a cosmic laboratory of exotic magnetohydrodynamic effects. Recent developments in technology have allowed for increasingly high-resolution observations of the solar atmosphere and of the dynamic features that take place there on various scales, from large coronal mass ejections (CMEs) that can extend far into the solar system, to relatively small spicules and fibrils that are close to the limit of our observational capabilities.

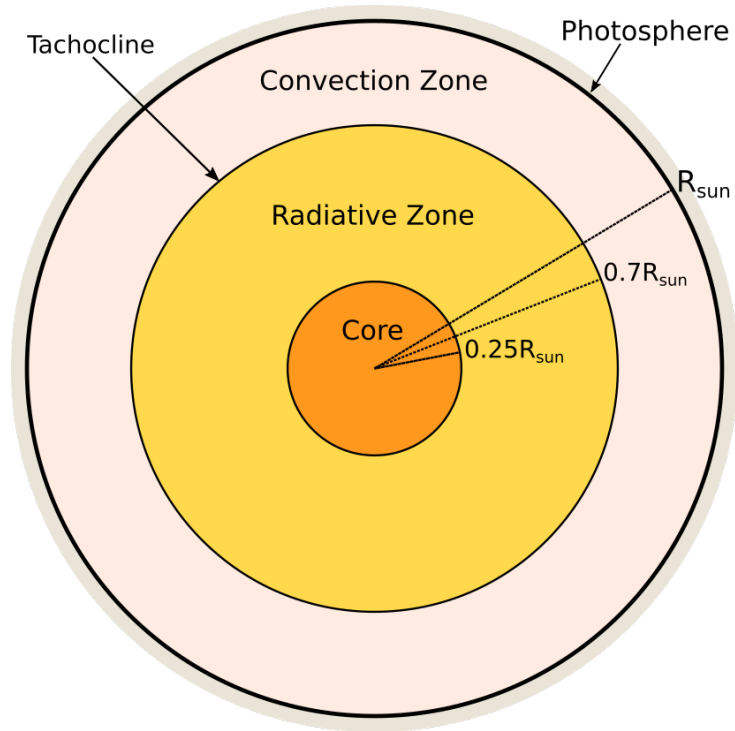


Figure 1.1: A diagram of the structure of the Sun, showing the scale of the different regions of the solar interior.

## 1.2 Solar Interior

Like all stars, the Sun was born from the gravitational collapse of a giant molecular cloud of gas and dust. It is composed of 92% hydrogen (in the plasma state, i.e. as ionised gas), which it converts into helium primarily via a type of nuclear fusion reaction known as the proton-proton chain. This reaction takes place in the *core* of the Sun, releasing massive amounts of energy in the form of photons and resulting in temperatures of up to 15 million Kelvin (Priest, 2014). This energy slowly makes its way through the *radiative zone*, an incredibly dense and opaque region where the photons are absorbed and re-emitted repeatedly, before they reach the *convection zone*. Here plasma can move more freely and therefore can transport energy more quickly via convection. Similar to the motion of a lava lamp, material at the base of the convection zone is heated and rises, then emits the energy as it approaches the surface, and falls as it cools. Even below the surface,

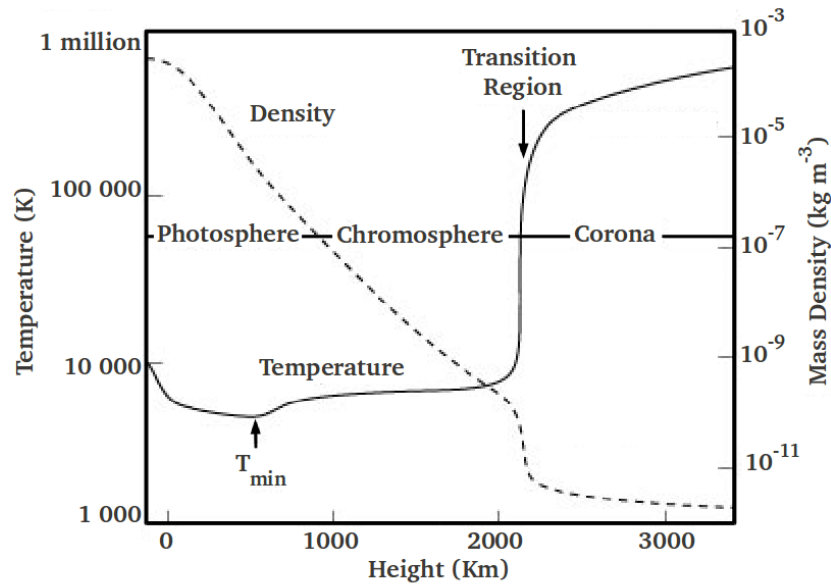


Figure 1.2: A graph of the temperature and density variation with height in the solar atmosphere, according to the VAL model (Vernazza et al., 1973). Image source Lang (2001).

waves propagate through the plasma and are reflected and refracted by the stratified structure of the solar interior (Leighton et al., 1962). The study of such waves via helioseismology allows us to infer properties of solar plasma and the structure of the Sun (Claverie et al., 1979; Fossat et al., 2017).

## 1.3 Solar Atmosphere

### 1.3.1 Photosphere

The heat and energy generated in the core is transferred outward towards the surface of the Sun via a process that can take around 170,000 years (Mitalas and Sills, 1992). However, the temperature actually falls to its minimum of around 4000 Kelvin just above the lowest region of the solar atmosphere, the *photosphere*.

The radius of the Sun is 695,500 km, or around 109 times that of the Earth. However, unlike the Earth, the radius of a star is not defined by a solid

surface but is generally thought of as the point at which the plasma becomes opaque to visible light, or as the point at which the local temperature equals the solar effective temperature (Brown and Christensen-Dalsgaard, 1998). The photosphere is thus the apparent surface of the Sun from which visible light is emitted. This region is relatively thin, with a thickness of only a few hundred kilometers (Priest, 2014). Many solar phenomena originate from or are ‘anchored’ in the photosphere.

In this base layer of the solar atmosphere, we can observe features such as granulation, a pattern of tightly packed irregular shapes across the entire photosphere. Granulation is the evidence of convective plasma cells rising to the surface, formed by columns of convective material that extend from deep within the solar interior — these shapes, or granules, are only the visible top of the columns. The hot plasma rises in the bright center of each granule, then moves outwards towards the edges into the *intergranular lanes* where it flows downwards again (Hathaway et al., 2002).

Magnetic bright points (MBPs) are relatively compact<sup>1</sup> regions of concentrated magnetic flux (Dunn and Zirker, 1973; Berger et al., 1995; Crockett et al., 2010; Keys, 2013; Liu et al., 2018) with field strengths on the order of a kilogauss (Keys et al., 2013, 2019; Vargas Domínguez and Utz, 2022) and with reduced density compared to the surrounding atmosphere, allowing observation deeper into the photosphere (De Wijn et al., 2009). Magnetic forces dominate inside MBPs, and they can be modelled as thin flux tubes (Cranmer and van Ballegoijen, 2005). They are thought to be the source of certain MHD waves (Jess et al., 2009; Fedun et al., 2011; Keys et al., 2011), and may be important in the transfer of kinetic energy through the otherwise turbulent lower solar atmosphere into higher regions. They have also been associated with the appearance of jets (Stenflo, 1973; Jess et al., 2012a), perhaps acting as anchor points — they occur frequently at intergranular lanes

---

<sup>1</sup>Like spicules, MBPs are close to the lower limit of the resolution we can currently observe even with the SST, Big Bear Solar Observatory (BBSO), or New Vacuum Solar Telescope (NVST), but it is possible that the Daniel K. Inouye Solar Telescope (DKIST) will enable a breakthrough on the observational side of this — see DKIST Science Use Cases (<https://nso.edu/telescopes/dkist/csp>) e.g. SUC178

and supergranule boundaries (Dunn and Zirker, 1973; De Wijn et al., 2009), the same regions we observe high concentrations of spicules (Tsiropoula et al., 2012).

Sunspots are relatively cool and dark regions of concentrated magnetic flux where energy transport by convection is inhibited. They can be observed in the photosphere in visible light and can sometimes even be seen without a telescope (using a solar filter to protect the eyes). As a result, they have been observed by astronomers for hundreds of years. Sunspots are an indicator of the *solar activity cycle* and are associated with *active regions* of the solar atmosphere, where strong magnetic fields occur in complex configurations of opposing polarity. It is also in these regions that extremely energetic events such as solar flares are most likely to occur, when the magnetic energy and material stored in the twisted magnetic field lines is released during the process of magnetic reconnection.

The Sun’s activity — including sunspot number, solar flare occurrence, magnetic flux, and radiation output — periodically changes over an 11-year duration. Solar maximum is the point in the cycle at which the Sun is most active, and it is at this time that large solar flares occur more frequently (Aschwanden, 2005). Solar activity can have an impact on space weather in the solar system and can adversely affect modern communications systems and technology; observing the photosphere is one way to monitor this activity cycle, which may allow us to predict these effects.

### 1.3.2 Chromosphere

The *chromosphere* is a highly dynamic region of the atmosphere and is the location of a variety of jets such as *spicules* (Beckers, 1968; Sterling, 2000) which form a ‘forest’ of constantly rising and falling energetic material. In addition, the region is characterised by plasma flows such as swirls (Wedemeyer-Böhm and Rouppe van der Voort, 2009; Liu et al., 2019a), and wave motions between the photosphere and the outer atmosphere (Jess et al., 2015). The intergranular magnetic field of the photosphere continues and expands upwards as the chromospheric *network*.

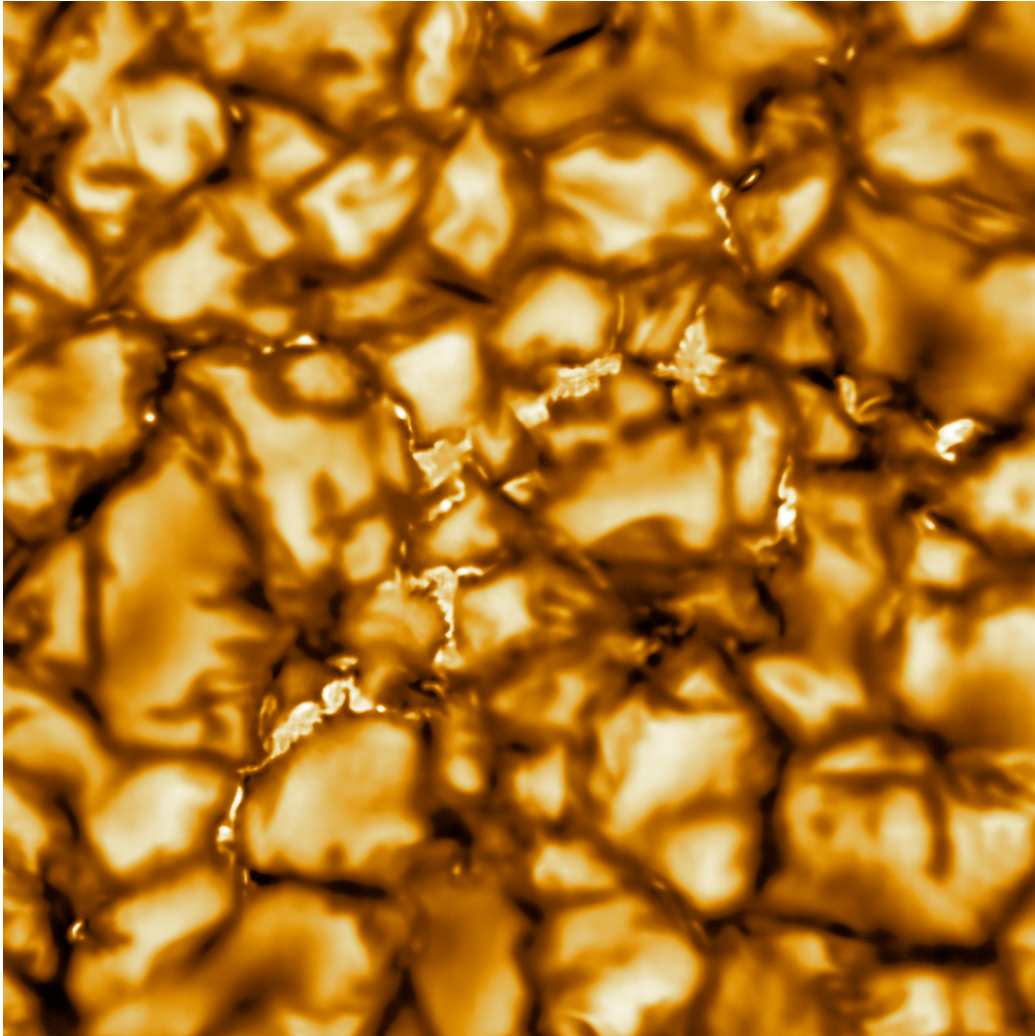


Figure 1.3: An image of the solar surface showing granulation, with magnetic bright points visible in the intergranular lanes. This image was taken by the Daniel K. Inouye Solar Telescope (credit due to NSO/NSF/AURA).

This layer of the atmosphere is around 2–3 Mm thick and can be observed in a wide range of electromagnetic wavelengths from visible light to EUV (De Pontieu et al., 2014). During a solar eclipse, the chromosphere is visible as a pink glow at the limb of the Sun due to its emission of the 656 nm wavelength of visible light known as H-alpha. Space-based platforms including the Solar and Heliospheric Observatory (SOHO) and Solar Dynamics Observatory (SDO) allow for advanced spectral imaging, enabling us to view the solar atmosphere at certain wavelengths not visible from Earth.

The lower chromosphere is dominated largely by plasma pressure forces rather than magnetic forces, except perhaps in certain localised phenomena such as flux tubes. This begins to change higher up in the region, giving rise to complex magnetic behaviour such as twisting, expansion, and reconnection (Ayres et al., 2009) while the field also interacts with the constantly moving plasma jets. Above the temperature minimum at the lower end of the chromosphere, the temperature rises with height and notably undergoes an extreme increase in the *transition region* between the chromosphere and the outer part of the solar atmosphere, starting around 3 Mm above the photosphere (Alissandrakis, 2022). Meanwhile the density decreases severely with height in the chromosphere, dropping by around 6–7 orders of magnitude from the photosphere to the corona (Priest, 2014; Roberts, 2019).

### 1.3.3 Corona

Named after the Latin word for ‘crown’, the corona is the outermost layer of the Sun’s atmosphere proper, although the heliosphere continues much further out into the solar system as the *solar wind* (Parker, 1958; Marsch, 2006). This region is visible during solar eclipses (or with a *coronagraph*) as a glowing halo around the Sun consisting of wispy strands of plasma. Coronal holes, areas of open field lines located at the poles of the Sun, are present for most of the solar cycle except during the solar maximum (Priest, 2014).

The corona is highly ionised, has low plasma density, and reaches a local temperature maximum on the order of 1 million Kelvin (Aschwanden, 2005). As a result, magnetic forces dominate (low plasma-beta) in the majority of

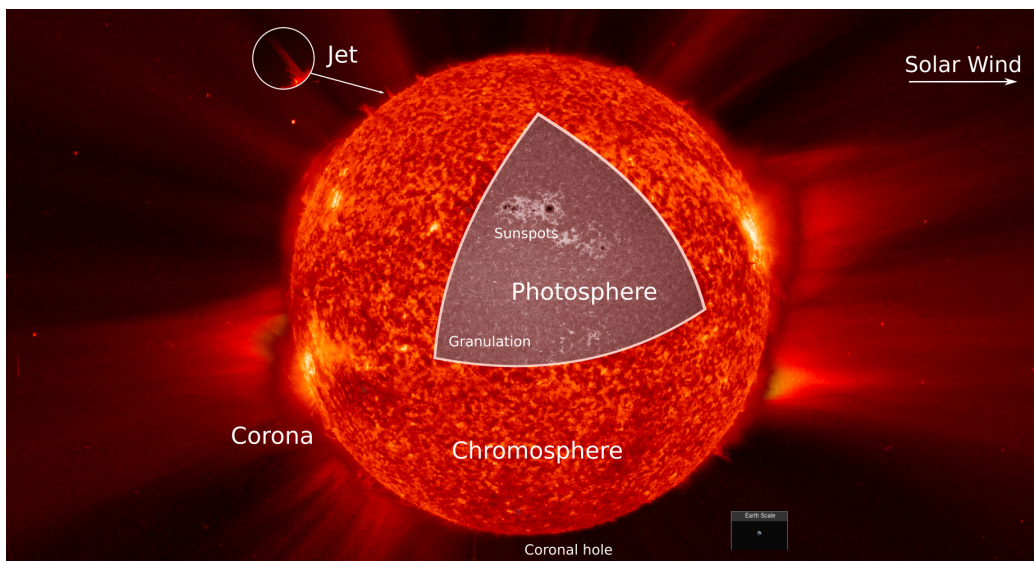


Figure 1.4: A diagram of the solar atmosphere, composed of images from space-based observatories. The images of the chromosphere and underlying photosphere are sourced from NASA's SDO using the AIA instrument to observe different wavelengths of light, at  $304\text{\AA}$  and  $1700\text{\AA}$  respectively. The background image of the corona was observed by ESA's SOHO using the LASCO instrument (and is not to scale). Helioviewer.org was used to obtain the images.

this region, and plasma forms large oscillating loops as it follows the arcing magnetic field lines anchored in the active regions of opposite polarity in the photosphere. Areas of closed magnetic field lines outside of coronal holes or active regions are known as the *Quiet Sun*, although these areas are still host to dynamic features such as jets, nanoflares, bright points, and loops (Aschwanden, 2005).

One of the major goals within the field of solar physics is to fully explain how the chromosphere and corona are heated to such extreme temperatures, such a short distance from the temperature minimum in the cooler photosphere. This is known as the *coronal heating problem* (Withbroe and Noyes, 1977; Zirker, 1993; Heyvaerts, 2000). Various mechanisms are expected to play a role in heating the chromosphere and corona, for example magnetic reconnection (Cirtain et al., 2013), Alfvén waves (Taroyan and Erdélyi, 2009; McIntosh et al., 2011), and chromospheric jets (Athay and Holzer, 1982; De Pontieu et al., 2011).

The solar wind is another subject of ongoing research, as the source of its heating and acceleration is complex and many different processes are involved. The boundary between the corona and solar wind is called the *Alfvén surface*, occurring in an irregular region at around 12–20 solar radii above the photosphere, at which point the bulk solar wind speed surpasses the Alfvén speed (typically on the order of  $300 \text{ km s}^{-1}$ , depending on the underlying corona) (DeForest et al., 2014; Adhikari et al., 2019). There are fast and slow components of the solar wind, which originate from different local magnetic field configurations in the corona (open or closed) - CMEs also have a large but transient effect on the solar wind (Marsch, 2006). The interaction of the solar wind with the Earth’s atmosphere and magnetic field gives rise to aurorae and geomagnetic storms.

## 1.4 Magnetohydrodynamics

Due to its ionised nature, the movement of plasma (described by its velocity field  $\mathbf{v}$ ) is influenced by, and affects, the magnetic field  $\mathbf{B}$ . The system of equations that govern plasma motion must therefore be adapted from the

equations of fluid dynamics and Maxwell's equations of electromagnetism, along with Ohm's law and physical conservation laws. The combined system is known as magnetohydrodynamics (MHD).

### 1.4.1 Solar Plasma

First, let us define the parameters and properties of the plasma.

The solar atmosphere, although comprised of plasma made up of charged electrons and ions, is considered to be almost electrically neutral on average, over a macroscopic scale. Local fluctuations result in charge imbalance, producing an electric field over a small region. A free charge in a plasma will become surrounded by particles of the opposite charge, shielding the free charge from the plasma at distances much greater than  $\lambda_D$ , a scale known as the *Debye length* (Goedbloed and Poedts, 2004). In this way, the plasma reacts to and compensates for local charge imbalances, and so is considered to be *quasi-neutral*.

In solar plasma, the number of particles inside a sphere of radius  $\lambda_D$  is large (Priest, 2014). The characteristic time scale  $t_0$  of plasma behaviour is short in comparison to the average time between collisions of charged and neutral particles, and the characteristic length scale  $l_0$  is large in comparison to the Debye length. It is also reasonable to assume that ions and electrons have similar velocities, and that MHD interaction takes place over non-relativistic timescales, i.e.

$$\frac{l_0}{t_0} \ll c, \quad (1.1)$$

where  $c$  is the speed of light. (Goedbloed and Poedts, 2004).

### 1.4.2 Electromagnetic equations

Now, let us introduce Maxwell's equations:

$$\nabla \cdot \mathbf{B} = 0 \quad (1.2)$$

$$\nabla \cdot \mathbf{E} = \frac{\rho^*}{\epsilon} \quad (1.3)$$

$$\nabla \times \mathbf{E} = -\frac{\partial \mathbf{B}}{\partial t} \quad (1.4)$$

$$\nabla \times \mathbf{B} = \mu \mathbf{j} + \frac{1}{c^2} \frac{\partial \mathbf{E}}{\partial t}. \quad (1.5)$$

Equation (1.2) is the *solenoidal constraint*, also known as Gauss' law of magnetism; this establishes the fact that there must be no magnetic monopoles in the system because the divergence of the magnetic field  $\mathbf{B}$  is zero.

Gauss' law (or Gauss' flux theorem) in Eq. (1.3) states that the divergence of the electric field  $\mathbf{E}$  is equal to the charge density  $\rho^*$  divided by the permittivity of free space  $\epsilon$ . Due to our assumption of charge neutrality, the right-hand side of this equation can be neglected for our purposes and so we have  $\nabla \cdot \mathbf{E} = 0$ .

Faraday's law in Eq. (1.4) states that a time-varying magnetic field also results in the presence of an electric field that is rotational, i.e. it varies in space in such a way that it is non-conservative.

Ampere's law, given by Eq. (1.5), relates the curl of the magnetic field to the current density  $\mathbf{j}$ . Here,  $\mu$  is the magnetic permeability, and  $c$  is the speed of light in a vacuum. Due to the assumption that we made in Eq. (1.1), we can neglect the second term on the right-hand side of Ampere's law and write  $\nabla \times \mathbf{B} = \mu \mathbf{j}$ .

In addition, we introduce Ohm's law:

$$\mathbf{j} = \sigma(\mathbf{E} + \mathbf{v} \times \mathbf{B}), \quad (1.6)$$

where  $\sigma$  is the electrical conductivity. This defines the total electric current as the total of the current due to the electric field  $\mathbf{E}$  acting on the plasma at rest, plus the additional current caused by the plasma moving through the magnetic field.

### 1.4.3 Induction Equation

Combining Ampere's law (1.5) with Ohm's law (1.6), along with the MHD assumptions we made in Section 1.4.1, results in

$$\eta(\nabla \times \mathbf{B}) = \mathbf{E} + \mathbf{v} \times \mathbf{B}, \quad (1.7)$$

where  $\eta = 1/\mu\sigma$  is the magnetic diffusivity. Next, we take the curl of Eq. (1.7) and substitute in Eq. (1.4), also using the vector identity

$$\nabla^2 \mathbf{B} = \nabla(\nabla \cdot \mathbf{B}) - \nabla \times \nabla \times \mathbf{B}, \quad (1.8)$$

along with Eq. (1.2). Then, after rearranging, we obtain the *induction equation*,

$$\frac{\partial \mathbf{B}}{\partial t} = \nabla \times (\mathbf{v} \times \mathbf{B}) + \eta(\nabla^2 \mathbf{B}). \quad (1.9)$$

The relationship between the magnetic field and the plasma velocity, defined by the induction equation, is key to magnetohydrodynamics. The first term on the right-hand side of Eq. (1.9) describes the effects of magnetic induction on the plasma, while the second relates to magnetic diffusion; the ratio between these terms is called the *magnetic Reynolds number*  $R_m$ , and can be approximated using characteristic values of the plasma speed  $v_0$  and length scale  $l_0$  as

$$R_m = \frac{v_0 l_0}{\eta}. \quad (1.10)$$

In most solar physics contexts,  $R_m$  is very large and therefore advection dominates over diffusion, thus we can neglect the second term on the right-hand side of the induction equation. In this case, we consider the plasma to be a perfectly conductive and ideal gas, which is known as *ideal* MHD. This also leads to Alfvén's Frozen-in Flux Theorem (Alfvén, 1943), which suggests that in the limit of  $R_m \rightarrow \infty$ , magnetic flux will be conserved and plasma will be 'fixed' to the magnetic field lines. Plasma in this case can only move parallel to the field lines; bulk motion perpendicular to the field lines will drag the field along with the plasma. In reality, some particles will still cross magnetic field lines, and processes such as magnetic reconnection demonstrate that the frozen-in theorem does not always apply. However, the theorem is often useful as an approximation when considering large length scales, such as in the solar atmosphere.

### 1.4.4 Plasma equations

Since we will be treating solar plasma as a perfect gas, we can introduce the *ideal gas law*,

$$p = \frac{k_B T}{m} \rho, \quad (1.11)$$

relating the pressure  $p$  and mass density  $\rho$  of the plasma, where  $T$  is the temperature,  $k_B$  is the Boltzmann constant, and  $m$  is the mean particle mass.

As usual, we must impose the physical constraint that mass is constant within the system, so there are no sources or sinks of matter. This is described by the *continuity equation*,

$$\frac{\partial \rho}{\partial t} + \nabla \cdot (\rho \mathbf{v}) = 0. \quad (1.12)$$

Applying Newton's second law to an ionised fluid in the presence of a magnetic field gives the equation of motion for a plasma,

$$\rho \frac{\partial \mathbf{v}}{\partial t} + \rho (\mathbf{v} \cdot \nabla) \mathbf{v} = -\nabla p + \mathbf{j} \times \mathbf{B} + \rho \mathbf{g}. \quad (1.13)$$

Similar to the Navier-Stokes equation describing fluid motion, Eq. (1.13) expresses that the change in the momentum of the plasma is proportional to the total of the forces acting on it: the force due to the gradient of the plasma pressure  $p$ , the *Lorentz force*  $\mathbf{j} \times \mathbf{B}$  due to the charged plasma moving through the magnetic field, and the force due to the effect of gravity  $\mathbf{g}$  directed towards the centre of the Sun.

Finally, we introduce the energy equation,

$$\frac{D}{Dt} \left( \frac{p}{\rho^\gamma} \right) = -\mathcal{L}, \quad (1.14)$$

where  $\gamma = 5/3$  is the ratio of specific heats for fully ionised plasma (Roberts, 2019), and  $\mathcal{L}$  is the energy loss function. We will consider only the adiabatic case  $\mathcal{L} = 0$ , which means that there is no energy loss or gain in the system.

### 1.4.5 Plasma Beta

Note that, using Faraday's law (1.4) with the MHD approximation and appropriate vector identities, the Lorentz force can be written as

$$\mathbf{j} \times \mathbf{B} = \frac{1}{\mu} (\nabla \times \mathbf{B}) \times \mathbf{B} = \frac{1}{\mu} (\mathbf{B} \cdot \nabla) \mathbf{B} - \nabla \left( \frac{\mathbf{B}^2}{2\mu} \right). \quad (1.15)$$

The two terms on the right-hand side of Eq. (1.15) are the magnetic tension force and the magnetic pressure force. Then, taking the ratio of the magnetic pressure force and the plasma pressure term in Eq. (1.13), we obtain an important dimensionless parameter, the *plasma beta*,

$$\beta = \frac{\text{gas pressure}}{\text{magnetic pressure}} = \frac{2\mu_0 p_0}{B_0^2}, \quad (1.16)$$

where the zero subscript represents the equilibrium value of the parameters. If  $\beta \ll 1$ , then magnetic forces dominate over pressure forces and thus the pressure gradient term in Eq. (1.13) can be neglected. This occurs in the corona and in other regions of low gas pressure and high magnetic field strength, including the Earth's ionosphere.

### 1.4.6 Linear MHD

Starting from the system of ideal MHD, we can *linearise* the equations by assuming an initial state of equilibrium and then perturbing the system, so that all quantities are defined as  $f = f_0 + f_1$ , where  $f_1$  is a small quantity. Since the system is initially static, the velocity is defined such that  $\mathbf{v}_0 = 0$ . We will also consider the plasma to be homogeneous and the equilibrium magnetic field to be constant and uniform in the  $z$ -direction,  $\mathbf{B}_0 = B_0 \hat{\mathbf{z}}$ . Then, neglecting all non-linear (small) terms as well as gravity, we obtain

the system of linear ideal MHD,

$$\nabla \cdot \mathbf{B}_1 = 0 \quad (1.17)$$

$$\frac{\partial \mathbf{B}_1}{\partial t} = \nabla \times (\mathbf{v}_1 \times \mathbf{B}_0) \quad (1.18)$$

$$\frac{\partial \rho_1}{\partial t} + \rho_0 \nabla \cdot \mathbf{v}_1 = 0 \quad (1.19)$$

$$\rho_0 \frac{\partial \mathbf{v}_1}{\partial t} = -\nabla p_1 + \frac{1}{\mu_0} (\nabla \times \mathbf{B}_1) \times \mathbf{B}_0 \quad (1.20)$$

$$\frac{\partial p_1}{\partial t} + \gamma p_0 \nabla \cdot \mathbf{v}_1 = 0. \quad (1.21)$$

Differentiating the equation of motion with respect to  $t$ , we can then combine Eq. (1.20) with Eqs. (1.19) and (1.18) to obtain a wave equation,

$$\frac{\partial^2 \mathbf{v}_1}{\partial t^2} - c_s^2 \nabla (\nabla \cdot \mathbf{v}_1) = \frac{1}{\mu_0 \rho_0} (\nabla \times (\nabla \times (\mathbf{v}_1 \times \mathbf{B}_0))) \times \mathbf{B}_0, \quad (1.22)$$

where  $c_s = \sqrt{\gamma p_0 / \rho_0}$  is the sound speed. If we also neglect the pressure perturbation, so  $p_1 = 0$ , then the second term on the left-hand side of Eq. (1.22) becomes zero.

Now, consider plane-wave solutions so that  $\mathbf{v}_1$  is of the form

$$\mathbf{v}_1 = (v_x, v_y, v_z) e^{i(\mathbf{k} \cdot \mathbf{r} - \omega t)}, \quad (1.23)$$

where  $v_x, v_y, v_z$  are constants,  $\mathbf{k}$  is the wave-vector and  $\omega$  is the frequency. This allows us to replace  $\partial_t$  with  $-i\omega$ , and  $\nabla$  with  $i\mathbf{k}$ . Therefore, taking into account the  $p_1 = 0$  condition, Eq. (1.22) becomes an eigenvalue problem,

$$\omega^2 \mathbf{v}_1 = \frac{B_0^2}{\mu_0 \rho_0} \left( \left( \mathbf{k} \times (\mathbf{k} \times (\mathbf{v}_1 \times \hat{\mathbf{z}})) \right) \times \hat{\mathbf{z}} \right). \quad (1.24)$$

This implies that  $\mathbf{v}_1$  is orthogonal to  $\hat{\mathbf{z}}$ , and so the plasma velocity is perpendicular to the equilibrium field  $\mathbf{B}_0$ . If we define the vector  $\mathbf{k}$  to be in the  $x-z$  plane and consider the  $y$ -component of  $\mathbf{v}_1$ , we find a dispersion relation

$$(\omega^2 - v_A^2 k_z^2) v_y = 0, \quad (1.25)$$

where

$$v_A = \frac{B_0}{\sqrt{\mu_0 \rho_0}} \quad (1.26)$$

is the *Alfvén speed*. Therefore we have found that the perturbation results in Alfvén waves, which propagate along the magnetic field lines with phase velocity  $v_A$  and with magnetic tension as their restoring force.

## 1.5 MHD in the Solar Atmosphere

Throughout the solar atmosphere, magnetohydrodynamic waves are ubiquitous (Erdélyi, 2008; Mathioudakis et al., 2013; Jess et al., 2015; Srivastava et al., 2021). Structures formed in the solar atmosphere can act as waveguides for MHD waves. For example, cylindrical magnetic features such as sunspots or jets can be modelled as *magnetic flux tubes* in which the magnetic field lines are parallel to the tube axis and the field has a discontinuity at the tube boundary; other structures such as prominences may be modelled as *magnetic slabs*, where layers of plasma meet at planar discontinuities.

Waves in magnetic configurations such as these have been studied in great detail. For example, Defouw (1976) studied wave propagation in a magnetic flux tube and later Roberts and Webb (1978, 1979) described more generally the governing equations and dispersion relations for flux tube waves; Roberts (1981a,b) and Edwin and Roberts (1982) examined surface waves at a magnetic interface and waves in a magnetic slab; Hollweg (1978, 1981) and Hollweg et al. (1982) investigated propagating nonlinear Alfvén waves with numerical methods; and Spruit (1981, 1982) studied the properties of waves in thin flux tubes. More recently, Allcock (2020) studied magnetohydrodynamic wave theory with a focus on asymmetric waveguides.

In solar jets, various waves have been observed to occur (Zaqarashvili and Erdélyi, 2009; Bate et al., 2022). The purely magnetic Alfvén wave described in Section 1.4 is one example of an MHD wave mode, but when pressure and other factors are taken into account we obtain other types of wave such as the fast and slow *magneto-acoustic waves* (MAWs). These are MHD waves with both the plasma pressure gradient and the Lorentz force as the restoring forces. Magneto-acoustic *kink modes* are transverse motions found in flux tubes, which involve oscillation of the axis of the tube (Edwin and Roberts, 1983; Morton et al., 2014), while *sausage modes* are symmetric

oscillations that perturb the magnetic interface. These have been observed in chromospheric jets (Kuridze et al., 2012; Shetye et al., 2021) and coronal loops (Nakariakov and Verwichte, 2005).

Torsional waves are a type of Alfvén wave that are thought to occur in footpoints of dynamic features (Ruderman et al., 1997; Mathioudakis et al., 2013), and are thought to play a role in coronal heating (Antolin and Shibata, 2010; Srivastava et al., 2017; Soler et al., 2019; Kohutova et al., 2020). Torsional Alfvén waves are known to occur in photospheric magnetic bright points and related features (Jess et al., 2009; Stangalini et al., 2021), and have been observed in many small-scale solar phenomena including spicules (De Pontieu et al., 2012). The relationship between these features is a subject of ongoing investigation; MBPs have been observed to exhibit oscillations that may be funnelled higher into the atmosphere through spicules (Jess et al., 2012a).

Vortex motions, occurring concurrently with magnetic swirls (Liu et al., 2019a), have been observed in association with bright points in the lower solar atmosphere (Wang et al., 1995; Wedemeyer-Böhm and Rouppe van der Voort, 2009; Liu et al., 2019b). These swirls are also associated with magnetic flux tubes (Kitiashvili et al., 2012). They are thought to have the potential to excite Alfvén waves (Fedun et al., 2011; Battaglia et al., 2021), in particular torsional Alfvén pulses, that propagate upwards from the photosphere (Liu et al., 2019c) and may transport energy to the upper chromosphere (Yadav et al., 2021), the corona (Wedemeyer-Böhm et al., 2012), and the solar wind (Finley et al., 2022). A major motivation for the research presented in this thesis is the need to improve our understanding of the role that these dynamic and magnetic features may have in the generation of solar jets.

## 1.6 Jets

A solar jet is characterised by a collimated, fast-moving flow of plasma originating from the lower solar atmosphere, resulting in a short-lived structure resembling a ‘spike’ of plasma.

Jets of plasma are particularly common throughout the chromosphere. There are various names for chromospheric jets, including *fibrils*, *mottles*, *straws*, *rapid blue-shifted excursions* (RBEs), and *spicules*. Many of these jets may in fact be very similar features viewed from different angles (Tsiropoula and Tziotziou, 2004; Rouppe van der Voort et al., 2009; Kuridze et al., 2015). Different solar jets are also observed on larger scales, e.g. macrospicules (Bohlin et al., 1975; Withbroe et al., 1976; Kiss et al., 2017; Kiss, 2019; Duan et al., 2023), and in other regions of the atmosphere, e.g. coronal X-ray jets (Shibata et al., 1992) and switchbacks (Magyar et al., 2021).

Solar jets, and spicules in particular, are an important part of the solar and heliospheric system due to their extreme prevalence on the Sun and their highly dynamic nature. Understanding the relationship between localised solar features may be the key to explaining the larger scale phenomena. A subject of great interest is the role of spicules in transferring energy, momentum, and mass into the upper solar atmosphere (McIntosh et al., 2011). Greater knowledge of the dynamics and processes which govern the behaviour of relatively small but energetic events, such as spicules, may shed light on the question of chromospheric and coronal heating and the origin of the mass flux of the solar wind.

### 1.6.1 Spicules and Chromospheric Jets

Spicules are an especially well-studied class of solar jet, as they were first observed in 1877 by Angelo Secchi (Secchi, 1877) and have since been the subject of much research (Beckers, 1968; Sterling, 2000; Zaqarashvili and Erdélyi, 2009; Tsiropoula et al., 2012). Although they have been observed for almost 150 years, they remain some of the smallest distinct features that can be observed in the solar atmosphere with diameters of only a few hundred kilometers. Appearing in the chromosphere in vast numbers, spicules create the appearance of ‘grass’, and are visible at the solar limb; although we can clearly see their vertical extents, it is difficult to observe their internal structures and the process of their formation. Spicules appear dark compared to the surrounding plasma of the chromosphere (see Fig. 1.5), suggesting cooler and denser plasma.

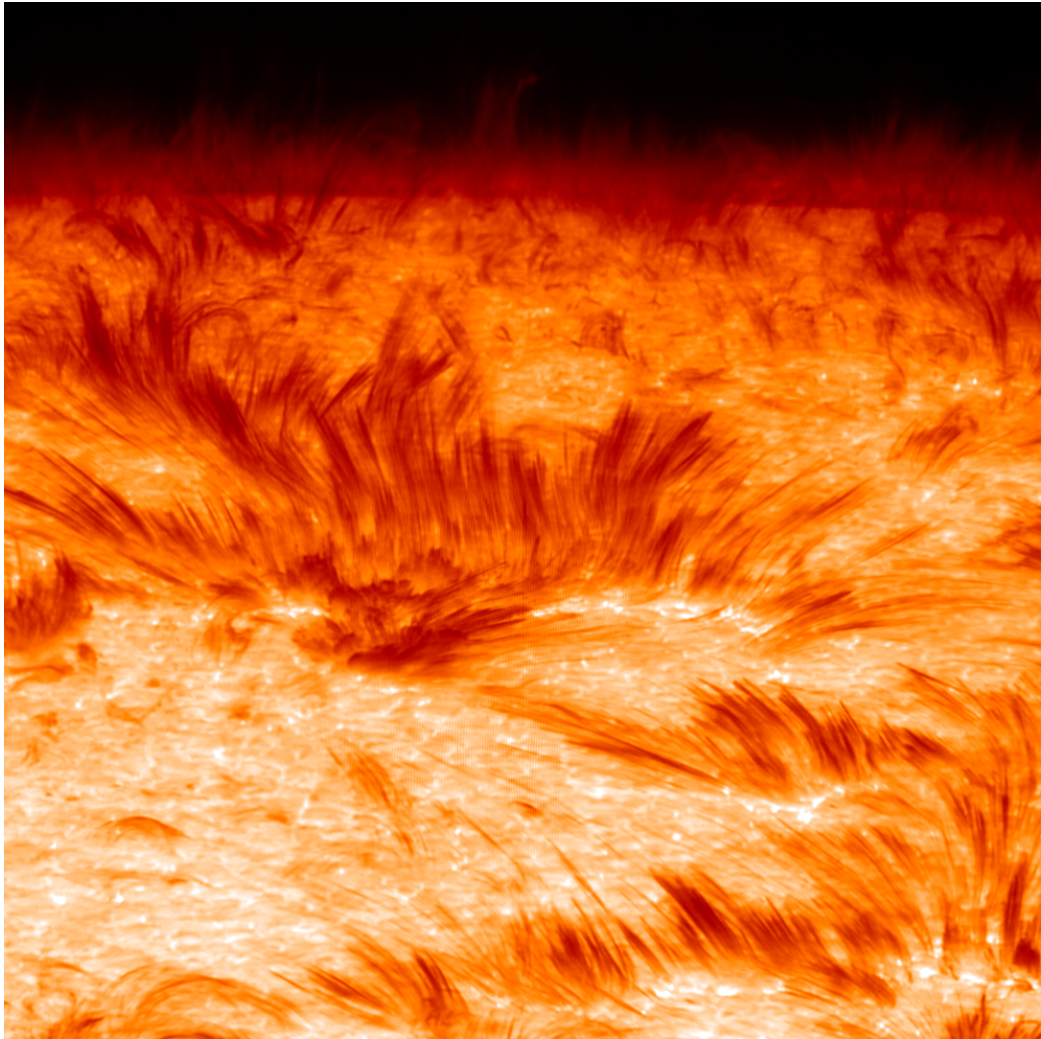


Figure 1.5: Spicules observed in the chromosphere. Source: EST, Swedish 1m Solar Telescope, Luc Rouppe van der Voort (CC BY-NC-ND 4.0)

It has been suggested that there are two main types of spicule (De Pontieu et al., 2007b). The traditional “Secchi-type” — or Type I — spicules have lifetimes of around 5 minutes on average, and exhibit rising and falling motion, moving at speeds on the order of  $20 \text{ km s}^{-1}$  (Sterling, 2000). Type II spicules, also referred to as rapid blue excursions (RBEs) (Roupe van der Voort et al., 2009; Kuridze et al., 2015), are distinguished by the way they are seen to fade away in hot coronal channels rather than falling back to the surface — this is thought to be due to these spicules being heated to the point that they disappear from the near-ultraviolet Ca II H passband while the jets themselves may continue to evolve, rising even higher into the atmosphere (Pereira et al., 2014). Type II jets are thought to be the faster of the two spicule classes, with speeds of around  $50\text{--}150 \text{ km s}^{-1}$ , and are described as ‘thin’ often with widths less than 200 km (De Pontieu et al., 2007b). They are also much more short-lived, often disappearing from (Ca II H) observations in under a minute (Roupe van der Voort et al., 2009). It should be noted that the existence of a clear distinction between Type I and II spicules has been called into question by Zhang et al. (2012). On the other hand, Pereira et al. (2012) found evidence to support the distinction and also suggested that Type II spicules were overwhelmingly more common than Type I in the quiet Sun (QS) and in coronal holes (CH), while Type I were more common in active regions.

The height of spicules can be difficult to measure since the ‘top’ is not clearly defined, but Beckers (1968) collected measurements of average spicule heights that range from 6.5 Mm to 9.5 Mm. The wavelength of light used to observe may make a difference — Pasachoff et al. (2009) found ranges for spicule height of 5.6–14.7 Mm when observed in 160 nm, and 4.1–12.2 Mm when observed in  $H\alpha$ . More recently, the maximum lengths of both types of spicules were found to be comparable by Pereira et al. (2012), but with some variation based on the local environment of the spicules; the average length in active regions was approximately 6.87 Mm for ‘parabolic’ (Type I) spicules and 7.75 Mm for ‘linear’ (Type II) spicules, while the average lengths were lower in the regions where Type II spicules dominate, at 5.48 Mm (QS) and 6.59 Mm (CH). The measured properties will depend on the spatial and temporal

resolution of the instrument as well as seeing conditions — older instruments may not observe smaller spicules and may even mistake several reoccurring jets for one long-lived ‘Type I’ spicule, while newer space-based instruments are more able to find jets matching the description of Type II spicules (Pereira et al., 2013).

### 1.6.2 Generation of Jets

The process that leads to the formation of solar jets is still a topic of active research, even though jets have been observed for over a century. It is reasonable to assume that more than one process is involved — some of these formation mechanisms and potentially related phenomena are discussed here.

Due to their presence in the majority of dynamic solar features, Alfvén waves are naturally thought to contribute to jet formation (Haerendel, 1992; Dover et al., 2020). Building on the preceding work of Hollweg et al. (1982), Hollweg (1982) provides an example of a numerical approach to the study of spicule formation with a focus on the role of Alfvén waves which, when non-linear processes are taken into account, may result in rebound shocks. The excitation of vertically propagating shocks in chromospheric flux tubes was studied further in Hollweg (1992), and was suggested as a driver for spicules. Using a similar numerical model, Kudoh and Shibata (1999) suggested that torsional Alfvén waves generated by random motions in the photosphere may lift the transition region in a motion consistent with the appearance of spicules. Later, Matsumoto and Shibata (2010) used a numerical flux tube model and found that Alfvén wave resonance may explain the dynamics of spicules and their potential to heat the corona.

One suggestion for the spicule mechanism proposed by Haerendel (1992) was that momentum may be transferred to the plasma by the damping of upwards-moving Alfvén waves, due to ion-neutral collisions. This was explored further via numerical simulations — for example, James and Erdélyi (2002) and James et al. (2003) found that spicules could not be convincingly recreated with their model, but also stated that the mechanism may still play a part in spicule formation due to the temperatures achieved in their simula-

tions. A later study by Martínez-Sykora et al. (2017) found that ion-neutral interactions allowed magnetic tension to be transported upwards and may be important for spicule formation. Overall, it appears that Alfvén waves may indeed be important in the formation of spicules, though the effect of ion-neutral interaction is yet to be fully determined.

Magnetically-driven jets have also been studied in the context of astrophysical phenomena of various scales (Shibata and Uchida, 1985; Innes et al., 1997; Smith, 2012), in addition to solar jets. Building on their earlier work relating to other astrophysical jets, Shibata and Uchida (1986) suggested a mechanism for solar jets involving a packet of magnetic twist driving mass along a flux tube, which they studied numerically.

Different mechanisms may be more likely to occur in certain regions of the solar atmosphere, which could have an influence on the diversity of the various classes of solar jets. The leakage of sub-photospheric *p-modes* into the atmosphere is an example of a mechanism that has been suggested to be able to drive plasma upwards and generate jets such as Type I spicules (Suematsu, 1980; De Pontieu et al., 2004) and fibrils (Hansteen et al., 2006). It has been theorised that global surface oscillations due to plasma motion in the convection zone may be responsible for the ‘forest’-like appearance of spicules in the chromosphere (Dey et al., 2022). Magnetic reconnection is another example of a mechanism that may drive jets (Samanta et al., 2019). This process has been explored as a possible mechanism for the formation of Type II spicules using numerical MHD simulations (González-Avilés et al., 2018), and has been observed to be associated with the formation of macrospicules (Duan et al., 2023). Other proposed mechanisms include granular buffeting (Roberts, 1979).

## 1.7 Thesis Outline

### Chapter 2

An analytical model is introduced to study torsional perturbations in flux tubes, and their ability to create vertical mass flux with the potential to

drive solar jets. The ideal MHD system is approximated via the use of a perturbation method to include limited non-linear effects. An Alfvén pulse is introduced at the lower boundary of a flux tube as a magnetic shear perturbation. Initially, Fourier and Laplace transforms are employed to solve the equations in the general case, along with continuity and boundary conditions. A relation is found for the vertically propagating waves. Complications arise when we attempt to apply the Laplace transform, establishing the premise for our use of the zero-beta approximation. Suitable stipulations are considered for the physical context of spicules, allowing us to simplify the MHD equations and look for solutions. We find that vertical plasma flux is formed as a result of a ponderomotive force.

### Chapter 3

Building on the previous iteration of the model, we utilise a flux tube model including a density discontinuity located at an upper boundary, corresponding to the transition region of the solar atmosphere. The propagating Alfvén wave is partially reflected from this boundary, and as a result the initial induced upwards mass flux is followed by the reversal of the flux, consistent with observed behaviour of jets. An example solution is used to study the properties of the pulse. The ratio of the transmitted and reflected mass flux is found and compared with the estimated relative total mass of spicules compared to that of the solar wind.

### Chapter 4

We expand on the model with the inclusion of a vertically stratified atmosphere in the form of a three-layered system, which specifies a decreasing function of height for the density in the intermediary layer between two constant-density layers. This is intended to better represent the conditions in the locality of solar jets in the lower solar atmosphere, improving on our previous analysis. We utilise the Fourier transform to find solutions for the induced vertical perturbations, and calculate the ratio of the mass flux above and below the transitional layer. We discuss the effect of varying the parameters of the transitional layer and make comparison with the expected physical

conditions of the solar atmosphere.

## **Chapter 5**

Finally, we summarise the results of the preceding chapters and discuss possible future work.

## CHAPTER 2

---

### Propagation of Torsional Alfvén Pulses in Zero-beta Flux Tubes

---

Our initial investigation into mathematically modelling solar features was developed into two papers, both published in *The Astrophysical Journal* (ApJ). Primarily, Scalisi et al. (2021a) will form the basis of this chapter, but Oxley et al. (2020) is also referenced. In addition, the development process of the model is explored in more detail than in the published paper.

In this chapter, we motivate and introduce an analytical flux tube model, which is then refined using the zero-beta approximation. We investigate analytically the generation of mass flux due to a torsional Alfvén pulse introduced at the lower boundary of the tube as a magnetic shear perturbation. Suitable assumptions are made for the physical context of spicules, allowing us to simplify the MHD equations and look for solutions. Boundary conditions are specified to create an example solution, and comparison is made with known properties of solar jets.

We derive that the presence of torsional Alfvén waves can result in vertical plasma motions; field-aligned plasma flux is formed non-linearly as a result of the Lorentz force generated by the perturbations. The formation of this mass flux may be a viable contribution to the generation of chromospheric

mass transport and could be consistent with the early stages of spicule evolution, thus playing potential roles in the formation of localised lower solar atmospheric jets.

These results are encouraging, but we acknowledge that a more complex model is required for the full evolution of a spicule. Critical discussion of the model follows, including suggestions for improvements to determine the entire evolution of a jet.

### 2.1 Background and motivation

Understanding different types of jets, particularly spicules and macrospicules, is a major goal for solar research given their ubiquity and therefore their role in the mass, momentum, and energy transport of the lower solar atmosphere. The process by which these jets form is not certain, but over the years there have been a wide range of theoretically proposed mechanisms. The non-linear MHD system involved in this formation process is difficult to solve even numerically, let alone analytically, although access to greater computing power has enabled the development of MHD simulations of jets. See Section 1.6.2 for a brief review of jet formation.

In spite of the theoretical challenges, analytical modelling allows us to consider a simpler version of this complex system, for example with an initial equilibrium state, and then introduce perturbations or controlled changes in order to examine the effect of specific phenomena without those features of interest being obscured by other effects. This can be useful as a first approximation for the behaviour of the system and gives an important alternative perspective to observations and simulations. In order to refine and improve our knowledge of the dynamic features of the solar atmosphere, we must use a variety of methods to consider all components of the system as well as the interactions between different processes.

An analytical study of note is Hollweg (1971), in which a perturbation method is utilised to investigate the second-order non-linear effects of Alfvén waves propagating in the direction of a background magnetic field, by con-

sidering multiple perturbation scales. The study concentrates on density perturbations, but the method could also be adapted to jets or spicules. We have employed similar techniques in our work, with applications such as different equilibrium conditions and perturbation structure, and a 3D coordinate system rather than only transverse and longitudinal components.

The same author provides an example of a numerical approach to the study of spicule formation in Hollweg (1982) with a focus on the role of Alfvén waves which, when non-linear processes are taken into account, may result in rebound shocks. The study presents the concept that spicules may form when the chromosphere is thrust upwards by these rebound shocks. In our analytical work, however, we find and argue that these shocks may not be necessary for spicule formation. Instead, weakly non-linear Alfvén waves may drive secondary perturbations *without* the development of shocks, directly triggering plasma movement which then may be identified with spicules. This also highlights the importance of using various approaches to study these features, as it is likely that multiple processes contribute to the excitation of jets.

The evolution of an Alfvén pulse was studied in Verwichte et al. (1999), using both analytical and numerical methods. This study utilised a perturbation method and assumed a homogeneous cold plasma, i.e. zero-beta. Although the study was not specific to solar jets, it was found that density perturbations and field-aligned plasma flows were possible as a result of this type of Alfvén wave. Consequently, a similar concept could be applicable to spicules and so we incorporate some aspects from this into our model.

Taking a different approach, Goodman (2012) attempted to model the acceleration of spicules by specifying a current which would generate an associated Lorentz force, and used the momentum equation to obtain the plasma velocity. Unfortunately, the method implemented by Goodman (2012) may not be valid, as the full MHD system is not considered properly in that paper (e.g. the induction equation is not mentioned). Hence, the specified current and results may not be applicable to solar plasma or spicule formation. The concept itself is reasonable, however, and should be explored further with mathematical rigour. Consequently, we re-evaluate the approach of Good-

man (2012) as part of the inspiration for the study presented here.

Shear flows, or equivalently a shear in the magnetic field due to the highly frozen-in property of the lower solar atmospheric plasma, may be capable of exciting vertical plasma motion, i.e. mass and momentum transport, due to the rise of the local Lorentz force. The idea of spicules driven by the Lorentz force (see e.g. Shibata and Uchida (1986)) requires further research and inspired us to construct our own model. In particular, we focus on the role of torsional Alfvén waves. Magnetic shear in the form of a torsional Alfvén wave pulse may provide the necessary Lorentz force.

Recent observational findings show strong links between torsional waves and magnetic flux concentrations, including magnetic bright points (Jess et al., 2009) and swirls (Liu et al., 2019c,a). It is thought that MBPs appear bright because through them we can observe deeper into the solar atmosphere (Berger et al., 2007; Sánchez Almeida et al., 2010), almost like looking through a tube. This, along with the nature of the jets themselves, will influence our choice of model. Our aim is to investigate the non-linear behaviour of a torsional Alfvén pulse to find a viable mechanism by which spicules may be formed, such that we account for their possible connection to localised magnetic waveguide features such as magnetic bright points.

## 2.2 Model

The model presented in this chapter uses an axially symmetric straight flux tube configuration and is an idealised description of the real solar atmosphere, assuming no stratification.

Using the regular perturbation method (Hinch, 1991) we model the effect of a localised magnetic field disturbance in the form of magnetic shear, and focus on the resulting Lorentz force. It should be emphasised that we use standard methods and the well-known ideal MHD equations, and as such the model discussed here shares properties with and builds on the methods of some works mentioned in Section 2.1 such as Hollweg (1971). However, our application is different and we specify the model for our purposes.

### 2.2.1 Physical Considerations

Flux tubes, as building blocks of the solar atmosphere, are a versatile tool for solar modelling applications (Mathioudakis et al., 2013; Ryutova, 2015) and a tube with a magnetic shear perturbation is a reasonable fit for the physical configuration we are interested in. The model could be applicable to the aforementioned magnetic bright points and swirls, which have the potential to generate magnetic wave fields comparable to the perturbation we consider. We will consider a cylindrical magnetic flux tube (see Figure 2.1) located in the lower solar atmosphere, anchored in a magnetic bright point and surrounded by the quiet Sun. Cylindrical coordinates  $(r, \theta, z)$  are hence defined such that the  $z$ -axis is directed vertically upwards along the centre of the tube, perpendicular to the solar surface.

Assuming a background state of equilibrium with a constant vertical magnetic field, we consider the effect of introducing a torsional Alfvén wave perturbation confined to a tube of radius  $R_0$ . Observations suggest MBPs have diameters up to around 0.6Mm (Berger et al., 1995; Liu et al., 2018), comparable to the observed width of spicules. Magnetic shear is introduced at the ‘base’ of the tube ( $z = 0$ ) which we consider to be at the height of the photosphere. The perturbation then propagates upwards as a pulse, travelling along the tube towards the upper chromosphere.

Although we are using a simplified model, the problem is complex in the general non-linear case, even when some higher order terms are neglected. One way to approach the problem is to consider the zero plasma-beta case, an approximation that is relevant in regions of dominant magnetic field strength when compared to the plasma pressure. Since MBPs are known to have considerably lower kinetic pressure than their surrounding plasma and have field strength on the order of a kilogauss (Keys et al., 2013), this approximation is appropriate for our purpose of modelling the lower atmospheric roots of MBPs. In the general case, we also assume total pressure is balanced at the boundary of the tube. Applying the zero-beta approximation inside the tube will allow us to consider this region independently and ignore the plasma pressure gradient, therefore enabling us to isolate the vertical component of the Lorentz force that directly results from the shear perturbation.

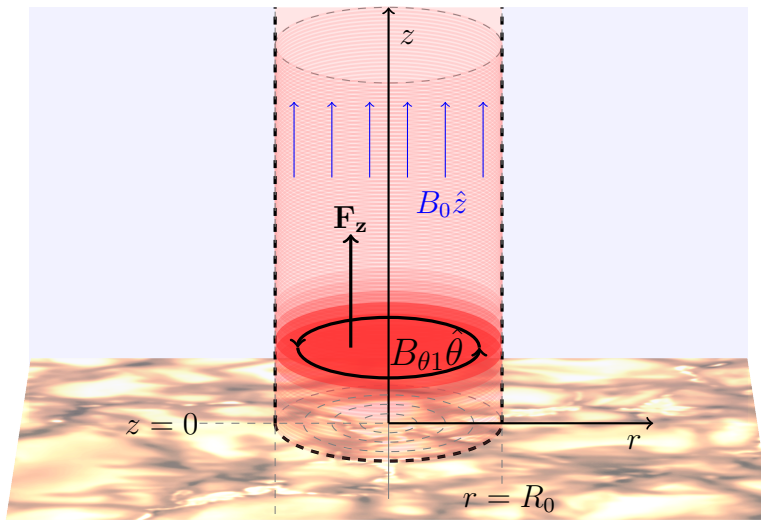


Figure 2.1: The flux tube in the region  $r < R_0$  and  $z > 0$ , with the torsional perturbation shown in darker red. The perturbation is an Alfvén pulse originating at  $z = 0$  and propagating vertically up the tube. The vertical force  $F_z = (\mathbf{j} \times \mathbf{B})_z$  is the  $z$ -component of the Lorentz force. The vertical magnetic field  $B_0 \hat{z}$ , shown by the blue arrows, is constant inside the tube. The image showing photospheric granulation and bright points is used for illustrative purposes only, to represent the photosphere at  $z = 0$ , and is adopted from the Daniel K. Inouye Solar Telescope (credit due to NSO/NSF/AURA).

### 2.2.2 The MHD framework

The standard ideal MHD equations (Goedbloed and Poedts (2004), see also Chapter 1) are used along with the solenoidal constraint  $\nabla \cdot \mathbf{B} = 0$ , but gravity is neglected, so we have

$$\rho \frac{\partial \mathbf{v}}{\partial t} + \rho(\mathbf{v} \cdot \nabla)\mathbf{v} = -\nabla p + \mathbf{j} \times \mathbf{B} \quad (2.1)$$

$$\frac{\partial \rho}{\partial t} + \nabla \cdot (\rho \mathbf{v}) = 0 \quad (2.2)$$

$$\frac{\partial \mathbf{B}}{\partial t} = \nabla \times (\mathbf{v} \times \mathbf{B}) \quad (2.3)$$

$$\frac{D}{Dt} \left( \frac{p}{\rho^\gamma} \right) = 0, \quad (2.4)$$

with the assumption that all quantities are independent of  $\theta$ , so  $\partial/\partial\theta = 0$ . The quantities  $\mathbf{B}$ ,  $\mathbf{v}$ ,  $\rho$ ,  $p$  are, respectively, the magnetic field, plasma velocity, mass density, and plasma pressure, and  $\mathbf{j} = \nabla \times \mathbf{B}/\mu_0$  is the current density (where  $\mu_0$  is the magnetic permeability of free space). Also, we assume that temperature is constant, and  $c = \sqrt{\gamma p/\rho}$  is the sound speed, where  $\gamma$  is the adiabatic gas index.

#### Perturbations

In order to begin studying the non-linear behaviour of the Alfvén wave, we use the regular perturbation method (Hinch, 1991). Let us define that each of the variables take the following functional form,

$$f(r, z, t) = f_0 + \sum_{i=1}^{\infty} \varepsilon^i f_i(r, z, t), \quad (2.5)$$

where  $\varepsilon$  is a small expansion parameter. Here,  $\varepsilon$  is the ratio of the strength of the torsional magnetic field perturbation to that of the vertical background field within the tube. The ‘zero-order’ quantities are assumed to be constant and in equilibrium, so  $\mathbf{v}_0 = 0$  and we define the equilibrium magnetic field  $\mathbf{B}_0 = B_0 \hat{z}$  to be constant and vertically aligned. The general case would require the background field and pressure to depend on  $r$  because they would be different in the interior versus the exterior region, but due to the zero-beta approximation which is assumed in this study, we find it is not necessary to

## 32 Propagation of Torsional Alfvén Pulses in Zero- $\beta$ Flux Tubes

make this distinction in the notation because we are able to focus only on the interior region (see Section 2.4).

In the linear approximation, we assume only a decoupled torsional Alfvén wave, which is the primary perturbation of order  $\varepsilon$ . By introducing terms of order  $\varepsilon^2$ , we now begin to consider the non-linear behaviour of the system, where we see the effect of the Lorentz force on the plasma, i.e. the manifestation of the second-order perturbation. Quantities are only defined up to order  $\varepsilon^2$ . The variables are thus perturbed in the following way,

$$\begin{aligned} v_r &= \varepsilon^2 V_{R2}, & v_\theta &= \varepsilon V_{\theta 1} + \varepsilon^2 V_{\theta 2}, & v_z &= \varepsilon^2 V_{Z2}, \\ B_r &= \varepsilon^2 B_{R2}, & B_\theta &= \varepsilon B_{\theta 1} + \varepsilon^2 B_{\theta 2}, & B_z &= B_0 + \varepsilon^2 B_{Z2}, \\ p &= p_0 + \varepsilon^2 p_2, & \rho &= \rho_0 + \varepsilon^2 \rho_2. \end{aligned} \quad (2.6)$$

The perturbed quantities are then substituted into the MHD equations. Since the features we wish to model are characterised by vertical motion of plasma according to observations, finding a solution for  $v_z$  is of particular interest.

### 2.2.3 First-order approximation

First, we neglect all terms involving square and higher powers of  $\varepsilon$ . Only the azimuthal components of the momentum and induction equations have terms of order  $\varepsilon$ ,

$$\frac{\partial V_{\theta 1}}{\partial t} = \frac{B_0}{\mu_0 \rho_0} \frac{\partial B_{\theta 1}}{\partial z} \quad (2.7)$$

$$\frac{\partial B_{\theta 1}}{\partial t} = B_0 \frac{\partial V_{\theta 1}}{\partial z}. \quad (2.8)$$

These equations can then be combined into the wave equations for  $B_{\theta 1}$ , e.g.

$$\frac{\partial^2 B_{\theta 1}}{\partial t^2} = \frac{B_0^2}{\mu_0 \rho_0} \frac{\partial^2 B_{\theta 1}}{\partial z^2}. \quad (2.9)$$

The solutions to Eq. (2.9) are waves propagating in the  $z$  direction at the Alfvén speed  $v_A$ , where  $v_A^2 = B_0^2 / \mu_0 \rho_0$ . For our purposes, we consider  $r, z, t \geq 0$  and use a solution for  $B_{\theta 1}$  of the form

$$B_{\theta 1}(r, z, t) = f(t - z/v_A)g(r). \quad (2.10)$$

Note we will only consider the wave travelling in the positive  $z$ -direction, so we introduce Elsässer variables (Elsässer, 1956),

$$R_{\pm} = v_{\theta} \pm \frac{v_A}{B_0} B_{\theta}. \quad (2.11)$$

Using the MHD equations we find solutions for  $R_{\pm}$  of the form

$$R_+ = R_+(t + z/v_A), \quad R_- = R_-(t - z/v_A). \quad (2.12)$$

Since we are only interested in the wave travelling in the positive  $z$ -direction, we will set  $R_- = 0$  and thus we obtain

$$v_{\theta} = -\frac{v_A}{B_0} B_{\theta}. \quad (2.13)$$

The relationship between  $v_{\theta}$  and  $B_{\theta}$  means that introducing a magnetic shear perturbation has the same effect as introducing a shear flow (velocity) perturbation.

### 2.2.4 Second-order approximation

Now, we collect terms of order  $\varepsilon^2$  in the MHD equations. The resulting system of equations shows how the torsional Alfvén waves affect the other quantities in the system. The  $\varepsilon^2$ -order equations (including the solenoidal constraint) are

$$\frac{\partial B_{R2}}{\partial r} + \frac{B_{R2}}{r} + \frac{\partial B_{Z2}}{\partial z} = 0, \quad (2.14)$$

$$\rho_0 \left( \frac{\partial V_{R2}}{\partial t} - \frac{V_{\theta 1}^2}{r} \right) = -\frac{\partial p_2}{\partial r} - \frac{1}{\mu_0} \left( \frac{\partial B_{\theta 1}}{\partial r} B_{\theta 1} + \frac{B_{\theta 1}^2}{r} - B_0 \left( \frac{\partial B_{R2}}{\partial z} - \frac{\partial B_{Z2}}{\partial r} \right) \right), \quad (2.15)$$

$$\rho_0 \left( \frac{\partial V_{\theta 2}}{\partial t} \right) = \frac{B_0}{\mu_0} \left( \frac{\partial B_{\theta 2}}{\partial z} \right), \quad (2.16)$$

$$\rho_0 \left( \frac{\partial V_{Z2}}{\partial t} \right) = -\frac{\partial p_2}{\partial z} - \frac{1}{\mu_0} \left( \frac{\partial B_{\theta 1}}{\partial z} B_{\theta 1} \right), \quad (2.17)$$

$$\frac{\partial \rho_2}{\partial t} + \rho_0 \left( \frac{\partial V_{R2}}{\partial r} + \frac{V_{R2}}{r} + \frac{\partial V_{Z2}}{\partial z} \right) = 0, \quad (2.18)$$

$$\frac{\partial B_{R2}}{\partial t} = B_0 \left( \frac{\partial V_{R2}}{\partial z} \right), \quad (2.19)$$

$$\frac{\partial B_{\theta 2}}{\partial t} = B_0 \left( \frac{\partial V_{\theta 2}}{\partial z} \right), \quad (2.20)$$

$$\frac{\partial B_{Z2}}{\partial t} = -B_0 \left( \frac{\partial V_{R2}}{\partial r} + \frac{V_{R2}}{r} \right), \quad (2.21)$$

$$\frac{\partial p_2}{\partial t} - \frac{\gamma p_0}{\rho_0} \frac{\partial \rho_2}{\partial t} = 0. \quad (2.22)$$

From here, we wish to find out whether the torsional perturbation  $B_{\theta 1}$  could result in jet-like motion by obtaining a solution for  $V_{Z2}$ . We could either attempt a general solution by combining the equations and using integral transforms, or we could look for a way to simplify the mathematical framework with suitable approximations. In our initial investigations we considered the first option, but unfortunately this quickly becomes a rather complex problem because the equations are coupled (see Section 2.3). As a result we were motivated to explore the latter option, presented in Section 2.4. Additionally, we are able to confirm that the approximation is compatible with the general case, shown in Section 2.4.1.

## 2.3 General case

Although approximations can be useful, it would be preferable to solve the general case of the problem. In the general case of the model, we must consider the radial as well as the vertical perturbation of the plasma, along with continuity and boundary conditions for the flux tube. The system of equations from the  $\epsilon^2$  approximation can be combined into fourth-order PDEs. Equations (2.16) and (2.20) are already decoupled from the rest of the system. First, we find an equation involving only  $V_{R2}$ ,  $B_{\theta 1}$ , and  $V_{\theta 1}$ . Fourier and Laplace transforms are needed to simplify the expression for  $V_{R2}$ . From this, we will be able to find expressions for the transforms of  $V_{Z2}$  and  $\rho_2$  in terms of  $V_{R2}$ , and apply boundary conditions to solve for the transform of  $V_{Z2}$ . Finally we will need to apply the appropriate inverse transformations to recover the original parameters. However, the inverse Laplace transform may present additional challenges given the need to connect the Riemann

sheets and due to the possibility of leaky waves, motivating our use of the zero-beta approximation as an alternative method.

### 2.3.1 Radial velocity perturbation

The fourth order PDE involving  $V_{R2}$  is

$$\begin{aligned} & \frac{\partial^4 V_{R2}}{\partial t^4} + \left( c^2 v_A^2 \frac{\partial^2}{\partial z^2} - (c^2 + v_A^2) \frac{\partial^2}{\partial t^2} \right) \left[ \frac{\partial^2 V_{R2}}{\partial z^2} + \frac{\partial}{\partial r} \left( \frac{1}{r} \frac{\partial}{\partial r} (r V_{R2}) \right) \right] \\ & = -\frac{1}{\mu \rho_0 r} \frac{\partial}{\partial t} \left[ \frac{\partial^2}{\partial t^2} \left( r B_{\theta 1} \frac{\partial B_{\theta 1}}{\partial r} \right) + \left( \frac{\partial^2}{\partial t^2} - c^2 \frac{\partial^2}{\partial z^2} \right) (B_{\theta 1}^2 - \mu \rho_0 V_{\theta 1}^2) \right] \end{aligned} \quad (2.23)$$

Note that the last term of Eq. (2.23) can be cancelled due to Eq. (2.13).

Define a Fourier transform for an even function  $f(z) = f(-z)$

$$\hat{f}(k) = \int_{-\infty}^{\infty} f(z) e^{-ikz} dz = 2 \int_0^{\infty} f(z) \cos(kz) dz, \quad (2.24)$$

and a Laplace transform for  $g(t)$ ,

$$\tilde{g}(s) = \int_0^{\infty} g(t) e^{-st} dt, \quad \Re(s) > 0. \quad (2.25)$$

When both transforms are applied to a function  $f(z, t)$  in either order,  $f$  is transformed to  $\bar{f}(k, s)$ . Apply both transforms to Eq. (2.23), using the assumption that  $V_{R2}$  is an even function of  $z$  with  $\frac{\partial^n}{\partial t^n} V_{R2} = 0$  at  $t = 0$  for  $n = 0, 1, 2, 3$ . Then  $V_{R2}(r, z, t)$  becomes  $\bar{V}_{R2}(r, k, s)$  while  $\frac{\partial}{\partial z}$  is replaced by  $ik$  and  $\frac{\partial}{\partial t}$  is replaced by  $s$ . Let  $\xi(r, z, t) = B_{\theta 1}^2$ . Thus Eq. (2.23) rearranges to

$$\frac{\partial^2 \bar{V}_{R2}}{\partial r^2} + \frac{1}{r} \frac{\partial \bar{V}_{R2}}{\partial r} - \left( \frac{1}{r^2} + a^2 \right) \bar{V}_{R2} = \alpha \frac{\partial \bar{\xi}}{\partial r}, \quad (2.26)$$

where

$$a^2 = \frac{(s^2 + v_A^2 k^2)(s^2 + c^2 k^2)}{s^2 c^2 + (s^2 + c^2 k^2) v_A^2}, \quad \alpha = \frac{s^3}{2\mu \rho_0 (s^2 c^2 + (s^2 + c^2 k^2) v_A^2)}. \quad (2.27)$$

If we set the RHS equal to zero then Eq. (2.26) is a modified Bessel equation with general solution  $\bar{V}_{R2} = P I_1(ar) + Q K_1(ar)$  where  $P$  and  $Q$  are constants

### 36 Propagation of Torsional Alfvén Pulses in Zero- $\beta$ Flux Tubes

in  $r$ . Using variation of constants we can find solutions for Eq. (2.26) of the form

$$\bar{V}_{R2} = u_1(r)I_1(ar) + u_2(r)K_1(ar), \quad \text{s.t.} \quad \frac{\partial u_1}{\partial r}I_1(ar) + \frac{\partial u_2}{\partial r}K_1(ar) = 0. \quad (2.28)$$

After some rearranging and use of integration by parts we find

$$\begin{aligned} \bar{V}_{R2} = & \left[ P + a\alpha \int_{R_0}^r r' K_0(ar') \bar{\xi}(r', k, s) dr' \right] I_1(ar) \\ & + \left[ Q + a\alpha \int_{R_0}^r r' I_0(ar') \bar{\xi}(r', k, s) dr' \right] K_1(ar). \end{aligned} \quad (2.29)$$

#### Internal and external regions

We will consider the behaviour of the system inside and outside a tube of radius  $R_0$ . Quantities inside the tube are given the subscript  $i$  while those outside are denoted  $e$ . For example

$$\bar{V}_{R2} = \begin{cases} \bar{V}_{R2_i}, & 0 \leq r \leq R_0, \\ \bar{V}_{R2_e}, & r > R_0. \end{cases} \quad (2.30)$$

For simplicity, the  $B_{\theta 1}$  magnetic field will be assumed to be negligible outside the tube. As a result the Alfvén speed will be zero for  $r > R_0$ , so  $v_A$  is only relevant in the interior region and does not need a subscript. Thus

$$a_e^2 = \frac{s^2 + c_e^2 k^2}{c_e^2}, \quad \alpha_e = \frac{s}{2\mu\rho_0 c_e^2}. \quad (2.31)$$

#### 2.3.2 Perturbation of total pressure

Total pressure is defined as

$$p_T = p_{T0} + \epsilon^2 p_{T2} = c^2 \rho + \frac{\mathbf{B} \cdot \mathbf{B}}{2\mu}. \quad (2.32)$$

Using the MHD equations and taking the Fourier and Laplace transforms, then substituting in  $\bar{V}_{Z2}$  from Eq. (2.47), we obtain an expression for the perturbation quantity  $\bar{p}_{T2}$  in terms of only  $\bar{V}_{R2}$  and  $\bar{\xi}$ ,

$$\bar{p}_{T2} = -\frac{s^2}{2\mu(s^2 + c^2 k^2)} \left[ \frac{1}{\alpha r} \frac{\partial}{\partial r} (r \bar{V}_{R2}) - \bar{\xi} \right]. \quad (2.33)$$

Then, using Eq. (2.29), we find

$$\bar{p}_{T2} = \Lambda \left\{ \left[ P + a\alpha \int_{R_0}^r r' K_0(ar') \bar{\xi} dr' \right] I_0(ar) - \left[ Q + a\alpha \int_{R_0}^r r' I_0(ar') \bar{\xi} dr' \right] K_0(ar) \right\}, \quad (2.34)$$

$$\Lambda = -\frac{s^2 a}{2\mu\alpha(s^2 + c^2 k^2)}; \quad \Lambda_i = -\frac{\rho_{0i}}{s a_i} (s^2 + v_A^2 k^2), \quad \Lambda_e = -\frac{s \rho_{0e}}{a_e}. \quad (2.35)$$

The total pressure must be continuous at the boundary of the tube,  $r = R_0$ .

### 2.3.3 Boundary conditions

Now, we introduce the boundary conditions for  $V_{R2}$  and  $p_{T2}$ ; the same conditions apply to  $\bar{V}_{R2}$  and  $\bar{p}_{T2}$ .

1.  $V_{R2} = 0$  at  $r = 0$ ,
2.  $V_{R2} \rightarrow 0$  as  $r \rightarrow \infty$ ,
3.  $V_{R2}$  and  $p_{T2}$  are continuous at  $r = R_0$ .

The first condition concerns only  $\bar{V}_{R2_i}$ . Note that  $K_1(x) \rightarrow \infty$  as  $x \rightarrow 0$ , while  $I_1(0) = 0$ . Therefore to satisfy the first condition we must have

$$Q_i - a_i \alpha_i \int_0^{R_0} r' I_0(a_i r') \bar{\xi}_i(r', k, s) dr' = 0. \quad (2.36)$$

Similarly for the second condition, we consider only  $\bar{V}_{R2_e}$ . Note that  $K_1(x) \rightarrow 0$  as  $x \rightarrow \infty$ , while  $I_1(x) \rightarrow \infty$ . Therefore to satisfy the second condition, assuming  $a_e > 0$ , we must have

$$P_e = -a_e \alpha_e \int_{R_0}^{\infty} r' K_0(a_e r') \bar{\xi}_e(r', k, s) dr' \quad (2.37)$$

However, the magnetic field perturbation is zero in this region, which means  $\bar{\xi}_e = 0$ . Thus  $P_e = 0$ .

To satisfy the third condition we must have

$$\bar{V}_{R2_i}(R_0, k, s) = \bar{V}_{R2_e}(R_0, k, s), \quad \text{and} \quad \bar{p}_{T2_i}(R_0, k, s) = \bar{p}_{T2_e}(R_0, k, s). \quad (2.38)$$

### 38 Propagation of Torsional Alfvén Pulses in Zero- $\beta$ Flux Tubes

Due to their limits at  $r$  and  $R_0$ , the integrals in  $\bar{V}_{R2i}$  and  $\bar{V}_{R2e}$  vanish at  $r = R_0$ , so

$$P_i I_1(a_i R_0) + Q_i K_1(a_i R_0) = P_e I_1(a_e R_0) + Q_e K_1(a_e R_0). \quad (2.39)$$

Again, the integrals in  $\bar{p}_{T2}$  (see Eq. (2.34)) are zero at the boundary, resulting in

$$\Lambda_i [P_i I_0(a_i R_0) - Q_i K_0(a_i R_0)] = \Lambda_e [P_e I_0(a_e R_0) - Q_e K_0(a_e R_0)]. \quad (2.40)$$

#### Finding constants

We have now explicitly found  $P_e$  and  $Q_i$ ,

$$P_e = 0, \quad (2.41)$$

$$Q_i = a_i \alpha_i \int_0^{R_0} r' I_0(a_i r') \bar{\xi}_i(r', k, s) dr'. \quad (2.42)$$

From these we can find  $P_i$  and  $Q_e$  by rearranging Eq. (2.39) and Eq. (2.40),

$$P_i = a_i \alpha_i \left( \frac{\Lambda_i K_0(a_i R_0) K_1(a_e R_0) - \Lambda_e K_0(a_e R_0) K_1(a_i R_0)}{\Lambda_e K_0(a_e R_0) I_1(a_i R_0) + \Lambda_i I_0(a_i R_0) K_1(a_e R_0)} \right) \int_0^{R_0} r' I_0(a_i r') \bar{\xi}_i dr', \quad (2.43)$$

$$Q_e = \frac{1}{R_0} \left( \frac{\alpha_i \Lambda_i}{\Lambda_e K_0(a_e R_0) I_1(a_i R_0) + \Lambda_i I_0(a_i R_0) K_1(a_e R_0)} \right) \int_0^{R_0} r' I_0(a_i r') \bar{\xi}_i dr', \quad (2.44)$$

where we have also used an identity from Abramowitz and Stegun (1964),

$$K_0(x) I_1(x) + K_1(x) I_0(x) = \frac{1}{x}. \quad (2.45)$$

#### 2.3.4 Vertical velocity perturbation

An equation for  $V_{Z2}$  in terms of  $V_{R2}$  is found by combining the  $t$  derivative of Eq. (2.17) with the  $z$  derivative of Eq. (2.18),

$$\frac{\partial^2 V_{Z2}}{\partial t^2} - c^2 \frac{\partial^2 V_{Z2}}{\partial z^2} = \frac{c^2}{r} \frac{\partial}{\partial r} \left( r \frac{\partial V_{R2}}{\partial z} \right) - \frac{1}{2\mu\rho_0} \frac{\partial^2}{\partial z \partial t} (B_{\theta 1}^2). \quad (2.46)$$

Take the Fourier and Laplace transform of this to obtain a relation between  $\bar{V}_{Z2}$  and  $\bar{V}_{R2}$ ,

$$\bar{V}_{Z2} = \frac{ik}{s^2 + c^2 k^2} \left[ \frac{c^2}{r} \frac{\partial}{\partial r} (r \bar{V}_{R2}) - \frac{s}{2\mu\rho_0} \bar{\xi} \right]. \quad (2.47)$$

Using the general solution for  $\bar{V}_{R2}$  found in Eq. (2.29) and the constants we derived in Section 2.3.3, solutions can be found for  $\bar{V}_{Z2}$ . The general form of  $\bar{V}_{Z2_j}$ , for  $j \in \{i, e\}$ , is

$$\begin{aligned} \bar{V}_{Z2_j} = & \frac{ik a_j c_j^2}{s^2 + c_j^2 k^2} \left\{ \left[ P_j + a_j \alpha_j \int_{R_0}^r r' K_0(a_j r') \bar{\xi}_j dr' \right] I_0(a_j r) \right. \\ & \left. - \left[ Q_j + a_j \alpha_j \int_{R_0}^r r' I_0(a_j r') \bar{\xi}_j dr' \right] K_0(a_j r) \right\} - \frac{ik \alpha_j v_A^2}{s^2} \bar{\xi}_j. \end{aligned} \quad (2.48)$$

Thus in the internal region,

$$\begin{aligned} \bar{V}_{Z2_i} = & \frac{-iks}{2\mu\rho_{0i}(c_i^2 + v_A^2)(s^2 + c_T^2 k^2)} \left[ v_A^2 \bar{\xi}_i + \left\{ K_0(a_i r) \int_0^r r' I_0(a_i r') \bar{\xi}_i dr' \right. \right. \\ & \left. \left. - I_0(a_i r) \left( \int_{R_0}^r r' K_0(a_i r') \bar{\xi}_i dr' + C \int_0^{R_0} r' I_0(a_i r') \bar{\xi}_i dr' \right) \right\} (s^2 + v_A^2 k^2) s^2 c_i^2 \right], \end{aligned} \quad (2.49)$$

where  $c_T^2 = (c_i^2 v_A^2)/(c_i^2 + v_A^2)$  and

$$C = \left( \frac{\Lambda_i K_0(a_i R_0) K_1(a_e R_0) - \Lambda_e K_0(a_e R_0) K_1(a_i R_0)}{\Lambda_e K_0(a_e R_0) I_1(a_i R_0) + \Lambda_i I_0(a_i R_0) K_1(a_e R_0)} \right). \quad (2.50)$$

In the external region, where  $\bar{\xi}_e = 0$ ,

$$\bar{V}_{Z2_e} = \frac{1}{D} \left[ \frac{iks^3 a_i^2 K_0(a_e r)}{2\mu R_0 (s^2 + c_i^2 k^2) K_0(a_e R_0) I_0(a_i R_0)} \int_0^{R_0} r' I_0(a_i r') \bar{\xi}_i dr' \right]. \quad (2.51)$$

Here

$$D = \rho_{0i} a_e (s^2 + k^2 v_A^2) \frac{K_1(a_e R_0)}{K_0(a_e R_0)} + \rho_{0e} s^2 a_i \frac{I_1(a_i R_0)}{I_0(a_i R_0)}. \quad (2.52)$$

Note setting  $D = 0$  results in an equation similar to the dispersion relation for surface waves in Edwin and Roberts (1983). The solution for  $\bar{V}_{Z2_e}$  has poles when  $D = 0$ .

### 2.3.5 Inverse Laplace transform for the external region solution

In order to recover  $V_{Z2}$  from  $\bar{V}_{Z2}$ , we must use the inverse Laplace and Fourier transforms. The inverse Laplace transform of a function  $\tilde{f}(s)$  is given by

$$f(t) = \frac{1}{2\pi i} \int_{\gamma - i\infty}^{\gamma + i\infty} \tilde{f}(s) e^{st} ds, \quad (2.53)$$

## 40 Propagation of Torsional Alfvén Pulses in Zero- $\beta$ Flux Tubes

such that  $\gamma > \gamma_0$  where  $\gamma_0 \in \mathbb{R}$  depends on the function  $f$ . In order to calculate the inverse LT for  $\bar{V}_{Z2}$  we will use contour integration. Recall from Section 2.3.1 that the Laplace transform was defined for  $\Re(s) > 0$ , so we will need to extend  $\bar{V}_{Z2}$  to the region  $\Re(s) < 0$ .

First, we need to ensure that  $\bar{V}_{Z2}$  is analytic on the appropriate region of the complex  $s$ -plane (Priestley., 2005). Although the complex square root would be needed to define  $a_i$ , it only appears raised to even powers in the solution for  $\bar{V}_{Z2}$ . This can be seen if we write the modified Bessel functions of the first kind, which in this case are analytic, as their power series expansions. However, the Bessel function  $K_\nu(a_e R_0)$  has a branch point at  $a_e = 0$  for all  $\nu \in \mathbb{C}$ . The principle branch corresponds to the principle value of the complex square root, which we will take to have positive real part. Therefore  $\bar{V}_{Z2}$  will have branch points at  $s = \pm ikc_e$ .

Consider an arbitrary point  $s \in \mathbb{C}$  and define

$$W_1 = s - ikc_e = |W_1|e^{i\phi_1}, \quad W_2 = s + ikc_e = |W_2|e^{i\phi_2}. \quad (2.54)$$

Take branch cuts in the complex  $s$ -plane starting from the branch points and extending along the imaginary axis to  $\pm i\infty$  as illustrated in Figure 2.2(a). This means we have restricted  $s$  so that  $\phi_1 \in (-\frac{3\pi}{2}, \frac{\pi}{2})$  and  $\phi_2 \in (-\frac{\pi}{2}, \frac{3\pi}{2})$ . Note that

$$a_e^2 = \frac{(s - ikc_e)(s + ikc_e)}{c_e^2} = \frac{|W_1||W_2|e^{i(\phi_1+\phi_2)}}{c_e^2}, \quad (2.55)$$

and therefore  $\arg(a_e) = \frac{1}{2}(\phi_1 + \phi_2)$ . Then if  $\Re(s) > 0$ , we have both  $\phi_1$  and  $\phi_2$  restricted to  $(-\frac{\pi}{2}, \frac{\pi}{2})$ , and we must have  $\arg(a_e) \in (-\frac{\pi}{2}, \frac{\pi}{2})$  i.e.  $\Re(a_e) > 0$ . Similarly if  $\Re(s) < 0$ , we find we still have  $\arg(a_e) \in (-\frac{\pi}{2}, \frac{\pi}{2})$  and so we find that the real part of  $a_e$  is always non-negative, as required.

So, the complex  $s$ -plane is restricted to the region

$$\mathbb{C}_1 = \mathbb{C} \setminus \{il \mid l \in (-\infty, -kc_e] \cup [kc_e, \infty)\}. \quad (2.56)$$

We establish a contour  $\Gamma$  as shown in Figure 2.2(b), which closes the Bromwich contour as required for the inverse Laplace transform. The complex function  $\bar{V}_{Z2}$  is not analytic, only because of its complex poles; it is meromorphic on the region inside  $\Gamma$ . The residue theorem will be used to account for these

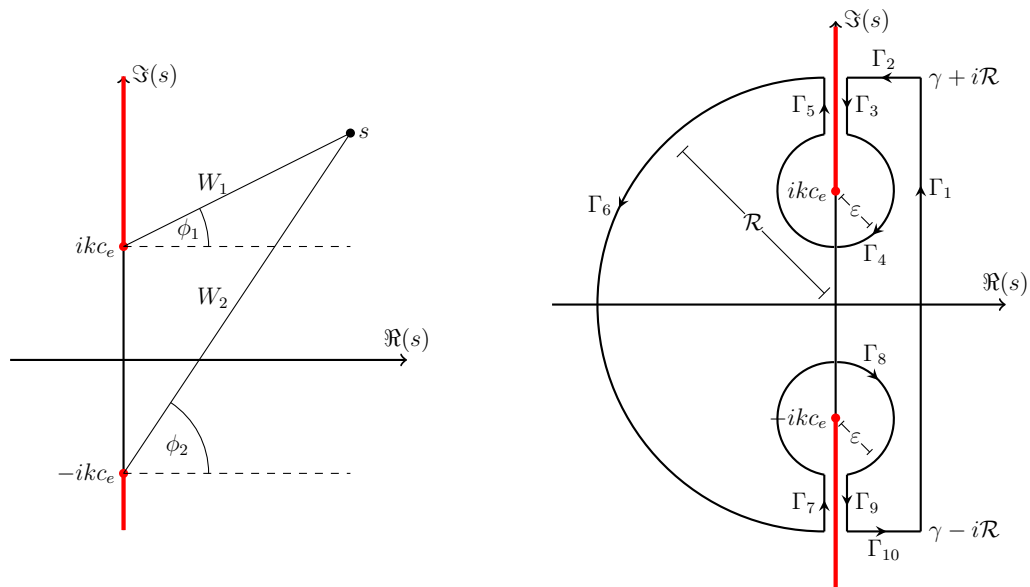


Figure 2.2: Left: the region  $\mathbb{C}_1$  of the complex plane is displayed. The red lines illustrate the branch cuts. Right: the contour  $\Gamma = \Gamma_1 + \dots + \Gamma_{10}$  in the complex  $s$ -plane, used to evaluate the inverse Laplace transform. Arrows show the direction of the contour.

poles and find the inverse LT. We only consider poles related to the eigenfrequencies of the function, which must be located on the imaginary axis. Therefore the condition  $\gamma > \gamma_0$  becomes  $\gamma > 0$ , and we can take  $\gamma \rightarrow 0$ . We take the radius of the contour to be  $\mathcal{R} \rightarrow \infty$  and the radii of the contours around the branch points to be  $\varepsilon \rightarrow 0$ .

Using Cauchy’s residue theorem (Ablowitz and Fokas, 2003), the contour integral is

$$\oint_{\Gamma} \bar{V}_{Z2} e^{st} ds = \sum_{n=1}^{10} \int_{\Gamma_n} \bar{V}_{Z2} e^{st} ds = 2\pi i \sum \text{res}(\bar{V}_{Z2}), \quad (2.57)$$

where  $\text{res}(\bar{V}_{Z2})$  is the sum of all the residues of the poles of  $\bar{V}_{Z2}$ , not including the poles on the branch cuts as they are outside the contour. Note that the integral along  $\Gamma_1$  is the integral required for the inverse Laplace transform, so if we can show that each of the remaining parts of the contour ( $\Gamma_2, \dots, \Gamma_{10}$ ) give no contribution to the whole contour integral, then

$$\hat{V}_{Z2} = \sum \text{res}(\bar{V}_{Z2}). \quad (2.58)$$

From here, we can apply the inverse Fourier transform and recover  $V_{Z2e}$ . A similar (more complicated) process could be used to find  $V_{Z2i}$ . However, it is difficult to determine if the remaining parts of the contour give a contribution to the integral. Therefore, we may need to use a different method to find  $V_{Z2}$  — for example, the zero-beta approximation. In particular, this will be necessary in order to refine our model so that it more accurately represents the conditions of the solar atmosphere, and to consider waves propagating in more than one direction.

## 2.4 Zero-beta approximation

The zero-beta approximation is applied to the region inside the tube. If the magnetic pressure dominates the plasma pressure ( $\beta \ll 1$ ) one can neglect the pressure term in the equation of motion and so for the interior region, Eq. (2.17) becomes

$$\frac{\partial V_{Z2}}{\partial t} = -\frac{1}{2\mu_0\rho_0} \frac{\partial}{\partial z} (B_{\theta 1}^2). \quad (2.59)$$

This equation is then decoupled from the rest of the MHD equations, so  $v_r$  does not need to be considered. In addition, since there are no  $r$  derivatives in Eq. (2.59) and if  $B_{\theta 1}$  is non-zero only within the tube,  $V_{Z2}$  is unaffected by anything in the region outside the tube in the zero-beta approximation. Note that the right-hand side of Eq. (2.59) comes from the  $z$ -component of the Lorentz force,

$$\mathbf{F}_z = (\mathbf{j} \times \mathbf{B})_z = -\varepsilon^2 \frac{1}{\mu_0} \frac{\partial B_{\theta 1}}{\partial z} B_{\theta 1}, \quad (2.60)$$

up to  $\varepsilon^2$  order. This force exists due to the torsional perturbation (or equivalently the shear flow  $V_{\theta 1}$ ) and is the sole driver for the vertical acceleration of the jet in this approximation.

Once  $B_{\theta 1}$  is defined (via the  $\varepsilon$ -order approximation in Section 2.2.3),  $V_{Z2}$  can be found directly by integration. However, boundary conditions must also be applied. Differentiating Eq. (2.13) with respect to  $t$  and then using Eq. (2.7), we find Eq. (2.59) becomes

$$\frac{\partial V_{Z2}}{\partial t} = \frac{1}{2\mu_0\rho_0v_A} \frac{\partial}{\partial t}(B_{\theta 1}^2). \quad (2.61)$$

We apply the conditions that both  $V_{Z2}$  and  $B_{\theta 1}$  are zero at  $t = 0$ . Integrating Eq. (2.61) directly with respect to  $t$ , we can then negate any constants of integration, so we have

$$V_{Z2}(r, z, t) = \frac{B_{\theta 1}^2}{2\mu_0\rho_0v_A}. \quad (2.62)$$

Note from Eq. (2.6) that  $B_{\theta}^2 = \varepsilon^2 B_{\theta 1}^2 + \mathcal{O}(\varepsilon^3)$  and so, if  $\varepsilon$  is small, we find that  $v_z \approx B_{\theta}^2/(2\mu_0\rho_0v_A)$  to leading order.

### 2.4.1 Relating to the general case

Combining the  $\varepsilon^2$ -order MHD equations from Section 2.2.4 allows us to find a fourth-order partial differential equation relating  $V_{Z2}$  and  $B_{\theta 1}$ ,

$$\begin{aligned} & \left[ \frac{\partial^4}{\partial t^4} + \left( c^2 v_A^2 \frac{\partial^2}{\partial z^2} - (c^2 + v_A^2) \frac{\partial^2}{\partial t^2} \right) \left( \frac{\partial^2}{\partial z^2} + \frac{1}{r} \frac{\partial}{\partial r} \left( r \frac{\partial}{\partial r} \right) \right) \right] (V_{Z2}) \\ &= - \frac{1}{2\mu_0 \rho_0} \frac{\partial^2}{\partial t \partial z} \left\{ \left[ \frac{\partial^2}{\partial t^2} - v_A^2 \left( \frac{1}{r} \frac{\partial}{\partial r} \left( r \frac{\partial}{\partial r} \right) + \frac{\partial^2}{\partial z^2} \right) \right] (B_{\theta 1}^2) \right. \\ & \quad \left. + \frac{2c^2}{r} \frac{\partial}{\partial r} (B_{\theta 1}^2 - \mu_0 \rho_0 V_{\theta 1}^2) \right\}. \end{aligned} \quad (2.63)$$

The full general case requires us to also consider  $V_{R2}$  and the pressure continuity at the tube boundary, resulting in greater complexity: as well as the field-aligned force, radial forces may play a part in accelerating plasma via a ‘squeezing’ effect. This is explored in greater detail in Chapter 2.3. Here, we simply aim to show how the result achieved using the zero-beta approximation fits with the general case, without going into unnecessary detail.

Since we still require wave solutions to the first-order equations, we will use Elsässer variables as in Section 2.2.3. Then, from Eq. (2.13), we find that  $B_{\theta 1}^2 - \mu_0 \rho_0 V_{\theta 1}^2 = 0$ . Thus, the final term on the right-hand side of Eq. (2.63) can be cancelled. Now, let  $\xi = t - z/v_A$ . Redefine  $V_{Z2} = V_{Z2}(r, \xi)$  and  $B_{\theta 1} = B_{\theta 1}(r, \xi)$  so that  $\partial/\partial t = \partial/\partial \xi$  and  $\partial/\partial z = -(1/v_A)\partial/\partial \xi$ . Then we find that many terms in Eq. (2.63) cancel (including all terms involving the sound speed  $c$ ), and so the equation can be re-written as

$$\frac{\partial^2}{\partial \xi^2} \left[ \frac{\partial}{\partial r} \left( r \frac{\partial}{\partial r} \right) V_{Z2} \right] = \frac{1}{2\mu_0 \rho_0 v_A} \frac{\partial^2}{\partial \xi^2} \left[ \frac{\partial}{\partial r} \left( r \frac{\partial}{\partial r} \right) B_{\theta 1}^2 \right]. \quad (2.64)$$

It should be noted that the result from Eq. (2.62) is consistent with this equation. Indeed, with suitable boundary conditions, Eq. (2.64) could be directly integrated to provide the required consistency. Thus we have further evidence to support that our zero-beta approximation method is valid for the physical configuration we model here.

### 2.4.2 Example solution and restrictions

The perturbation should be localised within the tube (i.e. negligible everywhere else), and it must be an Alfvén wave travelling in the positive  $z$

direction. In order to make sense physically,  $B_{\theta 1}$  must be zero at  $r = 0$ . As previously mentioned in Section 2.2.3,  $B_{\theta 1}$  can be specified as a product of some functions  $f(z, t)$  and  $g(r)$ . We impose a boundary condition at  $z = 0$  such that  $f(0, t) = f_0(t)$  is non-zero only within a finite time period,  $0 < t < \tau$ , where  $\tau$  is the characteristic time.

The wave is introduced from the boundary at  $z = 0$ , before the driver is ‘switched off’ at the characteristic time. This results in a pulse that propagates along the flux tube, and we will have  $f = f_0(t - z/v_A)$ . By changing the value of  $\tau$  we can scale the length of the pulse. Additionally, we will require  $B_{\theta 1} = 0$  at  $t = 0$ , i.e.  $f(z, 0) = f_0(-z/v_A)$  must be zero for all positive  $z$ .

Next, since  $g$  is so far an arbitrary function, we will define  $g(r)$  so that it is only non-zero within a certain radius  $0 \leq r \leq R_0$  corresponding to the flux tube region. Then  $B_{\theta 1}$  is an Alfvén pulse which is localised in both  $z$  and  $r$ .

For a more specific example, define the pulse  $B_{\theta 1} = B_{\max} f(t - z/v_A) g(r)$  such that

$$f(t - z/v_A) = \sin\left(\frac{\pi(t - z/v_A)}{\tau}\right), \quad 0 \leq t - z/v_A \leq \tau, \quad (2.65)$$

$$g(r) = \sin\left(\pi(r/R_0)^\lambda\right), \quad 0 \leq r \leq R_0, \quad (2.66)$$

where  $f$  and  $g$  are otherwise zero and  $B_{\max}$ ,  $\lambda$  are constants. We choose  $\lambda$  so that the pulse is localised mostly within the inner part of the flux tube; in this example  $\lambda = 1/4$ . The function  $f(t - z/v_A)$  is non-zero only for  $0 \leq t - z/v_A \leq \tau$  and is specified such that the characteristic time is half the period of the sine function. Recall that we also restrict the domain to  $z \geq 0$  and  $t \geq 0$ , so  $B_{\theta 1}$  is actually non-zero only when both  $t \in (z/v_A, \tau + z/v_A)$  for any fixed  $z$ , and  $z \in (z_{\min}, v_A t)$  where  $z_{\min} = \max\{0, v_A(t - \tau)\}$ . Note that  $f$  is zero at the boundaries of these intervals and similarly  $g$  is zero at  $r = 0$  and  $r = R_0$ , so the functions are continuous.

### 2.4.3 Results

We solved for  $V_{Z2}$  in Eq. (2.62), in order to study the nature of the vertical motion induced by the magnetic shear and potentially explore the relation-

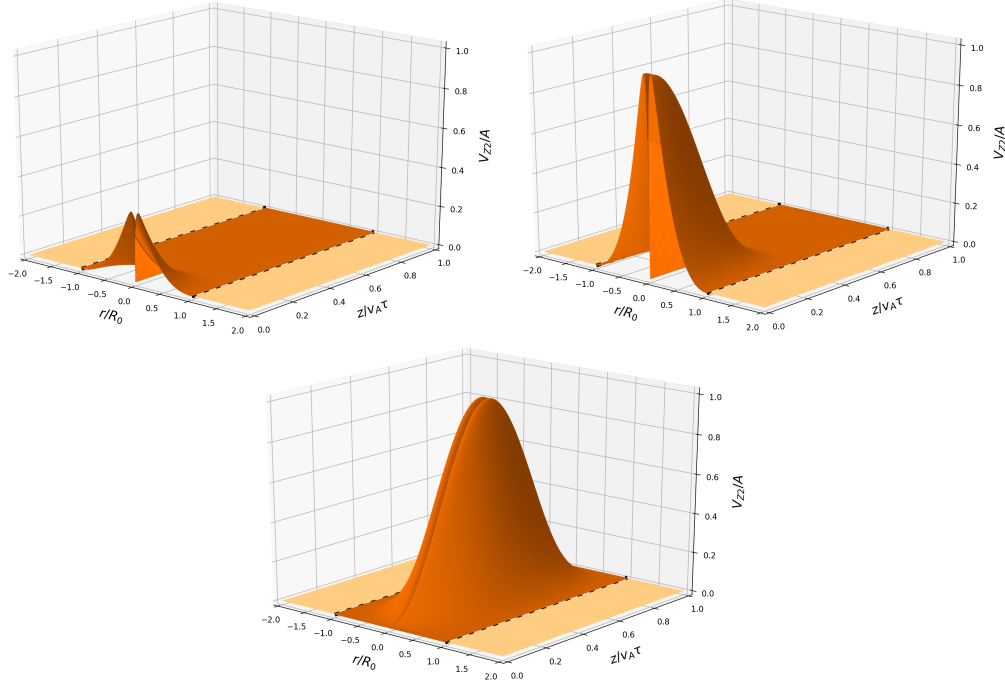


Figure 2.3: Above: a 2.5D representation of the given example of a  $V_{Z2}$  pulse from Section 2.4.2, at particular times  $t = 0.2\tau$ ,  $t = 0.5\tau$ , and  $t = \tau$ . The pulse appears as two peaks due to the axial symmetry around the  $z$  axis of the tube, and has been re-scaled so that the  $V_{Z2}$  (vertical) axis is in units of  $A = B_{\max}^2 / (2\mu_0\rho_0v_A)$ , while the  $r$  and  $z$  axis are in units of  $R_0$  and  $v_{AT}$  respectively. An animated version of this figure, showing the evolution of the pulse from  $t = 0$  to  $t = 2\tau$ , is available online.

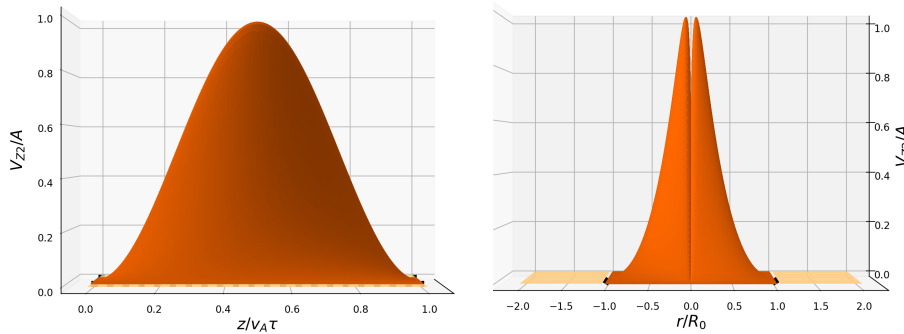


Figure 2.4: Rotated views of the 2.5D plot in Figure 2.3 at  $t = \tau$ , showing the  $z$  dependence (left) and the  $r$  dependence (right).

ship between this type of perturbation and the mass flux observed in the chromosphere in the form of jets. Using our example of  $B_{\theta 1} = B_{\max} f(t - z/v_A) g(r)$  from Section 2.4.2, the solution for  $V_{Z2}$  in the zero-beta case is simply proportional to the square of  $B_{\theta 1}$ ,

$$V_{Z2} = \frac{B_{\max}^2}{2\mu_0\rho_0v_A} \sin^2\left(\frac{\pi(t - z/v_A)}{\tau}\right) \sin^2\left(\pi(r/R_0)^\lambda\right), \quad (2.67)$$

for  $0 \leq t - z/v_A \leq \tau$  and  $0 \leq r \leq R_0$ , and zero otherwise - see Figures 2.3 and 2.4. Hence  $V_{Z2}$  will be of a similar form to  $B_{\theta 1}$ , i.e. a pulse propagating in the  $z$ -direction. We suggest that a pulse in the form of this example could possibly influence plasma and contribute to the formation of a jet. Using our perturbation model we can approximate the vertical mass flux of the plasma within the locality of the pulse,  $\phi_z = \rho v_z \approx \varepsilon^2 \rho_0 V_{Z2}$ .

Interestingly, the nature of the perturbation also suggests that there could be plasma with lower velocity near the centre of the flux tube, since we would have  $\phi_z = 0$  at  $r = 0$ . Once the pulse is fully formed at  $t = \tau$ , it will maintain its shape while it propagates in the positive  $z$  direction. For  $t \geq \tau$ ,  $\phi_z$  will be constant on concentric toroidal surfaces, which can be partially seen in Figure 2.5. The toroids degenerate into a cylinder, bounded by the limits for  $V_{Z2}$  stated in Eq. (2.67), as the magnitude of  $\phi_z$  approaches zero; outside of this cylinder there is no perturbation. The maximum magnitude of  $\phi_z$  is reached where both  $f$  and  $g$  are maximised, on the circle with radius  $r = R_0/(2^{1/\lambda})$  at  $z = v_A(t - \tau/2)$ . Other forms of the  $B_{\theta 1}$  pulse are of course possible as solutions to the first-order equations, but solutions which are suitable for the model are often similar to our example in form and behaviour.

## 2.5 Discussion

The actual velocity of the plasma would depend on the magnitude of the perturbation. Despite this, the results support the idea that a torsional Alfvén wave perturbation in the magnetic field could cause plasma to be set into motion by the Lorentz force. Even a small amount of plasma lifted from the photosphere would be significant in the chromosphere, thus it is possible that this mechanism could at least contribute to the initial formation of a

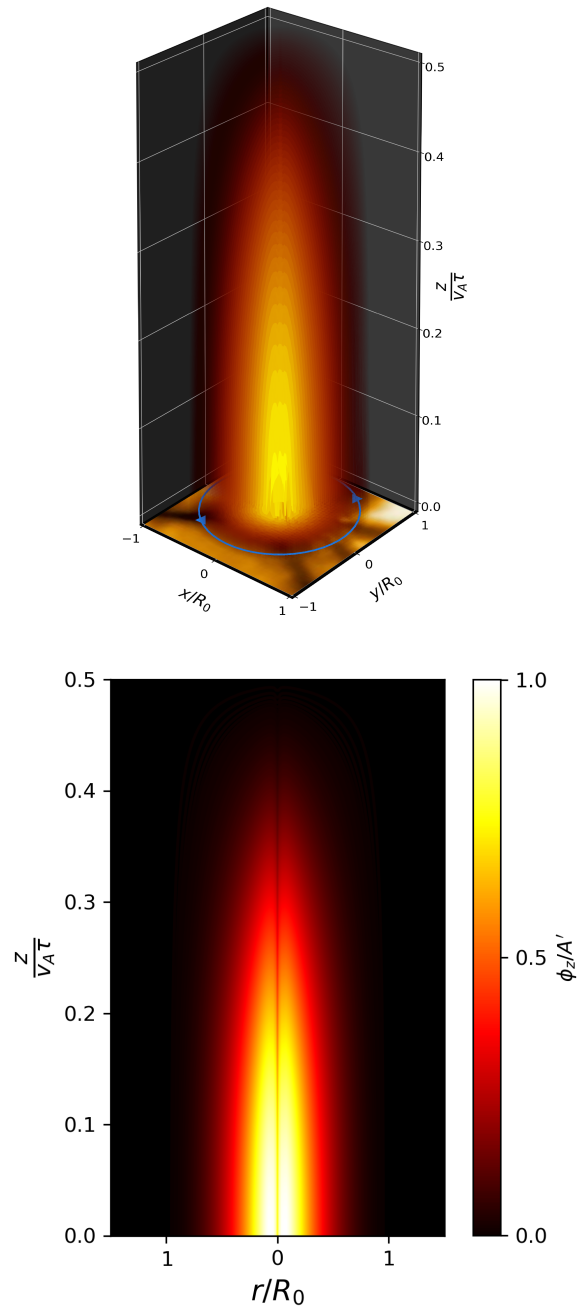


Figure 2.5: (Caption next page.)

Figure 2.5: (Previous page.) Upper image: a 3D plot of the vertical mass flux  $\phi_z$  at time  $t = \tau/2$ , for the example in Section 2.4.2 (with scaled Cartesian axes for simplicity). At this point the pulse is 'half formed' and there is positive mass flux for  $0 \leq z \leq v_A\tau/2$  within the tube. The blue arrows at the lower boundary represent the driver for the torsional magnetic field perturbation. An animated version of this figure, showing the evolution of the pulse from  $t = 0$  to  $t = \tau/2$ , is available online. Lower image: a cross section of the 3D plot (on a plane of constant  $\theta$ ), included to illustrate the structure of the perturbation. For both plots, lighter colours denote greater magnitude of  $\phi_z$ , but only a relative scale is given for this magnitude with  $A' = B_{\max}^2/(2\mu_0v_A)$ . The magnitude approaches zero at the boundaries for which the pulse was defined in Equations (2.65) and (2.66), and reaches its maximum value (dependent on the size of the perturbation of  $B_\theta$ ) in the interior, as shown.

solar jet, although the model is not intended to accurately describe the full evolution of a physical jet. The analysis is useful as a first approximation to explore this formation mechanism.

It is clear that the vertical extent of the pulse will be approximately  $v_A\tau$  simply due to the localised nature of the perturbation. We can gain more insight into this by comparing our results with observations of spicules and magnetic bright points. An Alfvén speed of 10–20 km s<sup>-1</sup> is feasible inside the flux tube, based on e.g. Jess et al. (2009); Cho et al. (2019) and estimations from data in Hewitt et al. (2014). This is assumed to be constant in the tube, which again is a simplification. Since our model focuses mainly on the chromosphere region, it is a reasonable assumption. Then, say, at  $t = 150$  s, possibly within the first half of the lifetime of a spicule and also within the range of expected lifetimes for MBPs (Keys et al., 2019), the pulse would reach a maximum vertical height of 1.5–3 Mm. Interestingly, this could also be a realistic height for a spicule in the early stages of its evolution, since spicules are observed to rise at speeds comparable to the Alfvén speed in this case (Sterling, 2000). This shows that the pulse could extend to a reasonable scale for a spicule within the time frame of the model, demonstrating a decent consistency between the model and observed properties of lower solar

## 50 Propagation of Torsional Alfvén Pulses in Zero- $\beta$ Flux Tubes

---

atmospheric jets.

The estimated value of the Alfvén speed may not be significantly greater than the sound speed expected in the general photosphere, which may be up to around  $10 \text{ km s}^{-1}$  (Jess et al., 2012b), perhaps suggesting that  $\beta \lesssim 1$ . However, it is expected that the conditions inside a magnetic bright point, partially evacuated of plasma and with high magnetic field strength (Shelyag et al., 2010), would result in a lower plasma beta than the surrounding atmosphere. The value of the plasma beta in a bright point was estimated by Cho et al. (2019) to be less than one on average, with estimated values as low as  $\beta = 0.2$ , therefore it is possible that the plasma beta is low enough for the zero-beta approximation to be useful, at least for the purposes of this model.

In this model, we assumed  $\rho_0$  to be constant due to the small scale of the processes we are considering compared to the height of the solar atmosphere. On a larger scale the density of the solar atmosphere decreases with height, so this model does not apply at higher elevations such as in the corona. Although the solution is a pulse which propagates to infinity, we know this would not occur in reality. For large  $t$  we expect that the solar atmosphere will deviate from the model, but the main objective was to study the effects in the photosphere and lower chromosphere since this is where the features of interest are likely to form. To improve the model, we could also take gravity and variable temperature into account. Including the  $\varepsilon^3$ -order perturbation terms would allow us to consider the back-reaction on the Alfvén wave, and we could also take into account reflection of the initial wave.

In the general case, without assuming  $\beta = 0$ , the model becomes more complex because the  $\varepsilon^2$ -order equations remain coupled. The equations of motion must be solved as fourth-order PDEs, and to solve for  $v_z$  we must apply the condition of continuous total pressure on both sides of the boundary of the tube in addition to boundary conditions for  $v_r$ . Due to the extra complexity it is possible that the plasma could be excited by both the Lorentz force acting vertically and by the radial ‘squeezing’ of the tube, causing material to be forced upwards due to the continuity of mass. The general case of this problem could be explored more thoroughly in future works.

The magnetic slab model may also be useful for investigating magnetic bright points and their role in the formation of spicules, especially the elongated bright points mentioned in Liu et al. (2018). A study using the slab model is conducted in a separate work (Oxley et al., 2020).



## CHAPTER 3

---

### Reflection and Evolution of Torsional Alfvén Pulses in Zero-beta Flux Tubes

---

This chapter is based on the paper of the same name, Scalisi et al. (2021b), published in *The Astrophysical Journal*.

Building on Chapter 2, we again utilise a flux tube model and study the behaviour of a torsional Alfvén pulse in the context of spicules. In order to account for the fact that most of the material in a spicule must fall back to the surface of the Sun, this model includes a density discontinuity located at an upper boundary, corresponding to the change in density found at the transition region of the solar atmosphere. A pulse is introduced at the lower, photospheric boundary of the tube as a magnetic shear perturbation and the resulting propagating Alfvén waves are reflected from the upper boundary. The induced upwards mass flux is thus followed by the partial reversal of the flux, which may be identified with the rising and falling behaviour of certain lower solar atmospheric jets.

We find the ratio of the mass flux present above the discontinuity compared to the mass flux resulting from the initial wave. This presents a method of estimating the relative total mass of spicules in relation to the total mass of the solar wind, and we find good agreement with previous estimations.

We also discuss the possibility that the interaction between the initial and reflected waves may create a localised flow that could persist after the initial pulse, and suggest that this could relate to the observation of distinct spicule types.

### 3.1 Background and motivation

In Chapter 2, we investigated torsional Alfvén waves, which are observed in the lower solar atmosphere and have long been theorised to be involved in the formation of spicules (see Section 1.6). We constructed a fundamental model as a starting point to explore the idea of an Alfvén wave perturbation originating in the vicinity of a MBP, notably utilising a perturbation method to include non-linear terms without excessive complexity, then considered the consequent vertical plasma motion and the possible connection to spicules based on their observed properties. The results were consistent with spicule formation as a first approximation, thus we now continue to advance the model to better represent the dynamics and later evolution of these features.

If the proposed mechanism is indeed related to jet formation then we should also account for the fact that not all of the material in solar jets can be transported into the higher atmosphere and solar wind. In fact, it has been suggested that spicules alone carry a mass flux into the low corona of 100 times that of the solar wind (De Pontieu et al., 2004), suggesting that spicules are a likely source for some of the material in the solar wind, but also that there must be a means to prevent the vast majority of their mass from reaching the outer solar atmosphere. Gravity is a known factor but, considering the nature of our model, wave reflection could also have a significant effect on the dynamics of jets and is another factor that should be taken into account.

There have been several studies on the reflection of Alfvén waves, for example recently Tsap and Kopylova (2021) provided an effective investigation involving reflection from a boundary at the transition region. Our model similarly considers a sharp boundary, although we use different methods for the model itself and our focus is on the possibility of application to jets. Certainly waves, in particular this type of torsional wave, seem to be a likely driver for

much of solar jet activity. In another example, Sterling and Hollweg (1984) suggest spicules may act as resonant cavities, with reflected torsional Alfvén waves resulting in heating and twisting of the spicule rather than the vertical motion. It is not certain if these different aspects could be caused by the same process acting differently at various stages of the evolution of the spicule, perhaps due to reflection, but the two ideas are not incompatible since our vertical mass flux is a secondary non-linear consequence of an initial magnetic perturbation. This vertical motion is due to the Lorentz force and is a known effect that has been studied in various MHD contexts. For example, see the study by Shibata and Uchida (1985), who numerically simulated jets driven in part by the Lorentz force. See also Rankin et al. (1994), where it is shown that a ponderomotive force due to shear Alfvén waves can drive plasma perturbations in the cold plasma of the Earth’s magnetosphere.

## 3.2 Reflected wave model

When considering waves on the scale of solar jets, which originate possibly from below the photosphere and extend well into the upper chromosphere, the stratification of the solar atmosphere should be taken into account. Waves may be affected by this stratification, especially in the transition region where the atmospheric density drops significantly. This somewhat sharp change in density may result in the reflection of a portion of the torsional Alfvén waves which originate from the solar surface or lower chromosphere, and propagate upwards. In fact, this may be a key part of the interaction between solar jets and this type of wave, which we began to study in our previous works Oxley et al. (2020); Scalisi et al. (2021a) (see Chapter 2).

Since certain jets are known to fall back after initially rising while others appear to fade, we would like to investigate how this behaviour can be attributed to wave reflection. It is of interest to determine whether wave reflection may affect jet dynamics, and to test if it could be a distinguishing factor between different types of jets. In particular, we want to know if a reflected wave may correspond to the falling motion of a jet.

### 3.2.1 Model formulation

The premise of this model is to examine the evolution of a wave that initially propagates vertically upwards and is then partially reflected downward from a boundary at  $z = L$ , representing the relatively sharp change in plasma density in the transition region.

The model that we use here is initially set up in a similar way to the model presented in Chapter 2. Inside the tube the plasma motion is described by the ideal magnetohydrodynamic (MHD) equations for zero-beta plasma,

$$\frac{\partial \rho}{\partial t} + \nabla \cdot (\rho \mathbf{v}) = 0, \quad (3.1)$$

$$\frac{\partial \mathbf{v}}{\partial t} = \frac{1}{\rho \mu_0} (\nabla \times \mathbf{B}) \times \mathbf{B}, \quad (3.2)$$

$$\frac{\partial \mathbf{B}}{\partial t} = \nabla \times (\mathbf{v} \times \mathbf{B}), \quad (3.3)$$

where  $\rho$  is the density,  $\mathbf{v}$  the velocity,  $\mathbf{B}$  the magnetic field, and  $\mu_0$  the magnetic permeability of free space. Note that we neglect the effect of gravity in the momentum equation. This is necessary due to our use of the zero-beta approximation and the fact that we initially have an equilibrium state; taking gravity into account would require a significantly more complex model. For the moment, we intend to focus solely on the effect of the reflected Alfvén wave. In the unperturbed state, there is a straight magnetic tube with the constant radius  $R$ . In cylindrical coordinates  $r, \theta, z$  with the  $z$ -axis coinciding with the tube axis, the equilibrium magnetic field is  $\mathbf{B}_0 = B_0 \hat{\mathbf{z}}$ , where  $\hat{\mathbf{z}}$  is the unit vector in the  $z$ -direction and  $B_0$  is a constant. We assume axial symmetry, so derivatives with respect to  $\theta$  are zero. The equilibrium density and velocity are  $\rho_0$  and zero, respectively. The magnetic field is confined inside the tube. The plasma outside the tube is magnetic-free and warm, and the equilibrium pressure of this plasma is equal to the magnetic pressure inside the tube. Hence, the total pressure at the tube boundary is continuous as required.

As in Chapter 2, we use the regular perturbation method and look for the solution to the system of equations (3.1)–(3.3) in the form of expansion with

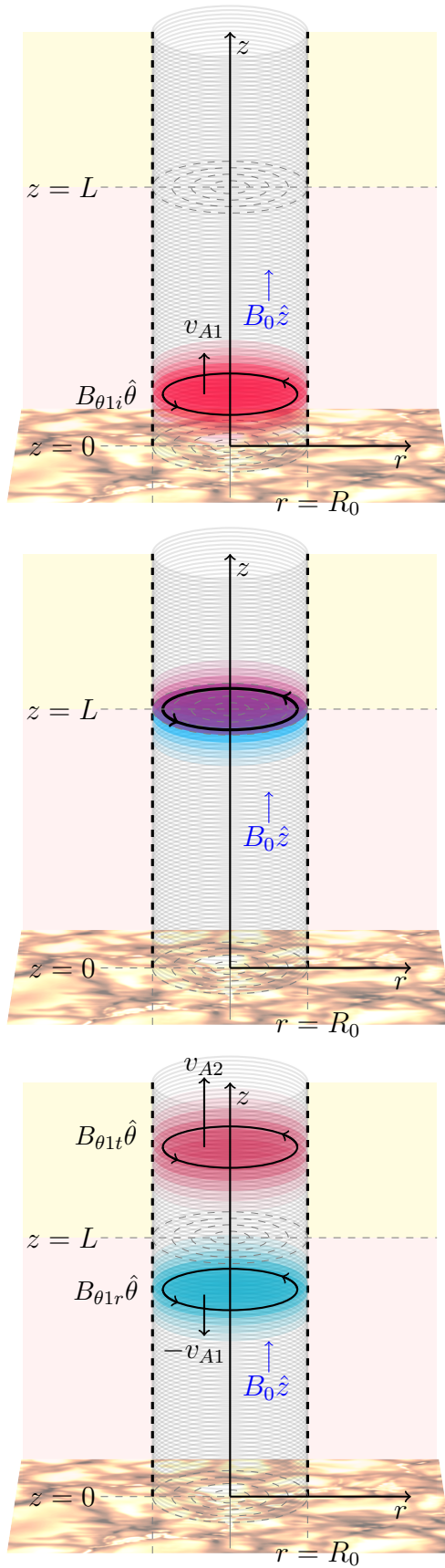


Figure 3.1: (Caption next page.)

Figure 3.1: (Previous page.) (a) The flux tube in the region  $r < R_0$  and  $z > 0$ , with the initial torsional perturbation shown in blue. The perturbation is an Alfvén pulse originating at  $z = 0$  and propagating vertically up the tube. The vertical magnetic field  $B_0\hat{z}$ , indicated by the blue arrow, is constant inside the tube. (b) The perturbation reaches the density discontinuity at  $z = L$  and is partially reflected. (c) The reflected and transmitted waves propagate in opposite directions. The image showing photospheric granulation and bright points is used for illustrative purposes only, to represent the photosphere at  $z = 0$ , and is adopted from the Daniel K. Inouye Solar Telescope (credit due to NSO/NSF/AURA).

respect to the small parameter  $\epsilon$ ,

$$f = f_0 + \epsilon f_1 + \epsilon^2 f_2 + \dots, \quad (3.4)$$

where  $f$  represents any of quantities  $\rho$ ,  $\mathbf{v}$ , or  $\mathbf{B}$  (see Eq. (2.6)). We recall that  $\mathbf{v}_0 = 0$ .

### 3.2.2 First-order approximation

At the surface  $z = 0$ , which we propose to be in the photosphere, we introduce an initial Alfvén wave perturbation in  $B_{\theta 1i}$  within the tube. Then, we assume that, in the first-order perturbation with respect to  $\epsilon$ , the solution is a torsional Alfvén wave where only the azimuthal components of the velocity and magnetic field perturbation are non-zero. The plasma outside of the magnetic tube is not perturbed. Then, the solution of the first-order approximation is the superposition of the incoming and reflected waves below the discontinuity and the transmitted wave above it. Hence, the expression for the azimuthal component of the magnetic field can be written as

$$B_{\theta 1} = \begin{cases} B_{\theta 1i}(t - z/v_{A1}) + B_{\theta 1r}(t + z/v_{A1}), & 0 \leq z < L, \\ B_{\theta 1t}(t - z/v_{A2}), & z > L. \end{cases} \quad (3.5)$$

Here, the subscripts  $i$ ,  $r$ , and  $t$  refer to the incoming, reflected, and transmitted waves, respectively. For  $z < L$  and  $z > L$  the Alfvén speeds are  $v_{A1}$  and

$v_{A2}$  respectively. We obtain from Eq. (3.2) in the first-order approximation that the azimuthal components of the velocity and magnetic field are related by

$$\frac{\partial V_{\theta 1}}{\partial t} = \frac{B_0}{\mu \rho_0} \frac{\partial B_{\theta 1}}{\partial z}. \quad (3.6)$$

It follows from Eqs. (3.5) and (3.6) that

$$V_{\theta 1} = \begin{cases} V_{\theta 1i}(t - z/v_{A1}) + V_{\theta 1r}(t + z/v_{A1}), & 0 \leq z < L, \\ V_{\theta 1t}(t - z/v_{A2}), & z > L. \end{cases} \quad (3.7)$$

Now, we specify the boundary conditions at the tube base and discontinuity:

- Introduce the torsional perturbation at  $z = 0$  as a localised ‘pulse’ driven from  $t = 0$  up until a characteristic time  $t = \tau$ , so we assume the form

$$B_{\theta 1} = F(t, r) \quad \text{at} \quad z = 0, \quad (3.8)$$

where  $F(t)$  is non-zero only for  $0 < t < \tau$ .

- Continuity of  $B_{\theta 1}$  and  $V_{\theta 1}$  at  $z = L$ , so

$$B_{\theta 1i}(t - L/v_{A1}) + B_{\theta 1r}(t + L/v_{A1}) = B_{\theta 1t}(t - L/v_{A2}), \quad (3.9)$$

$$V_{\theta 1i}(t - L/v_{A1}) + V_{\theta 1r}(t + L/v_{A1}) = V_{\theta 1t}(t - L/v_{A2}). \quad (3.10)$$

Initial condition:  $B_{\theta 1}(r, z, t = 0) = V_{\theta 1}(r, z, t = 0) = 0$ .

The incoming pulse arrives at the discontinuity at  $t = L/v_{A1}$  and, at this time, the reflected and transmitted waves appear. The incoming wave completely disappears at  $t = \tau + L/v_{A1}$ . The leading edge of the reflected pulse arrives at the  $z = 0$  boundary at  $t = 2L/v_{A1}$  and completely disappears at  $t = \tau + 2L/v_{A1}$  if we assume that the reflected pulse is completely absorbed at this boundary. The transmitted wave also appears at  $t = L/v_{A1}$  and exists for any  $t > L/v_{A1}$ . We will assume that  $\tau < L/v_{A1}$ .

From the first-order equation (3.6) and the definitions of  $B_{\theta 1}$  and  $V_{\theta 1}$ , we have

$$V_{\theta 1i} = -\frac{v_{A1}}{B_0} B_{\theta 1i}, \quad V_{\theta 1r} = \frac{v_{A1}}{B_0} B_{\theta 1r}, \quad V_{\theta 1t} = -\frac{v_{A2}}{B_0} B_{\theta 1t}. \quad (3.11)$$

Thus, Eq. (3.10) can be rewritten as

$$B_{\theta 1i}(t - L/v_{A1}) - B_{\theta 1r}(t + L/v_{A1}) = \frac{v_{A2}}{v_{A1}} B_{\theta 1t}(t - L/v_{A2}). \quad (3.12)$$

Using Eqs. (3.8), (3.9), and (3.12) we obtain

$$B_{\theta 1t}(t) = \frac{2v_{A1}}{v_{A2} + v_{A1}} F(t - L(1/v_{A1} - 1/v_{A2})), \quad (3.13)$$

$$B_{\theta 1r}(t) = \frac{v_{A1} - v_{A2}}{v_{A2} + v_{A1}} F(t - 2L/v_{A1}). \quad (3.14)$$

Using these equations we then also obtain that the azimuthal component of the magnetic field above the discontinuity ( $z > L$ ) is given by

$$B_{\theta 1}(t, z) = \frac{2v_{A1}}{v_{A2} + v_{A1}} F(t - L/v_{A1} - (z - L)/v_{A2}). \quad (3.15)$$

Below the discontinuity ( $z < L$ ) the azimuthal component is given by

$$B_{\theta 1}(t, z) = F(t - z/v_{A1}) - \frac{v_{A2} - v_{A1}}{v_{A2} + v_{A1}} F(t + (z - 2L)/v_{A1}). \quad (3.16)$$

In this expression, the first term corresponds to the incident wave, and the second to the reflected wave. Recalling that  $F(t) = 0$  for  $t \leq 0$  and  $t \geq \tau$  we notice that the incident wave completely disappears for  $t > \tau + L/v_{A1}$ . The reflected wave first exists below the discontinuity only for  $L/v_{A1} < t < \tau + 2L/v_{A1}$ . In particular, it follows from these results that the azimuthal component of the magnetic field is zero everywhere below the discontinuity for  $t \geq \tau + 2L/v_{A1}$ .

Using Eq. (3.11), we arrive at

$$V_{\theta 1}(t, z) = - \begin{cases} \frac{v_{A1}}{B_0} \left( F(t - z/v_{A1}) + \frac{v_{A2} - v_{A1}}{v_{A2} + v_{A1}} F(t + (z - 2L)/v_{A1}) \right), \\ \frac{2v_{A1}v_{A2}}{B_0(v_{A2} + v_{A1})} F(t - L/v_{A1} - (z - L)/v_{A2}). \end{cases} \quad (3.17)$$

for  $z < L$  and  $z > L$ , respectively.

### 3.2.3 Second-order approximation

Although we are using a similar model to Chapter 2, there will be important differences here because now we do not neglect the waves travelling in the negative  $z$ -direction. The second-order perturbation  $V_{Z2}$ , that describes vertical plasma motion influenced by the primary torsional perturbation via the Lorentz force, may have a more complex form than in Chapter 2.

Collecting terms of the order of  $\epsilon^2$  in the  $z$ -component of Eq. (3.2), we obtain

$$\frac{\partial V_{Z2}}{\partial t} = -\frac{1}{2\mu\rho_0} \frac{\partial}{\partial z} (B_{\theta 1}^2) = -\frac{1}{B_0} B_{\theta 1} \frac{\partial V_{\theta 1}}{\partial t}, \quad (3.18)$$

noting that the right-hand side of the equation results from the  $z$ -component of the Lorentz force, which in this case is also the ponderomotive force. This result is consistent with Chapter 2. Let us now solve this equation separately below and above the discontinuity. First, we consider the region below the discontinuity and take  $z < L$ . Using Eqs. (3.16) and (3.17), we reduce Eq. (3.18) to

$$\frac{\partial V_{Z2}}{\partial t} = \frac{1}{\mu_0\rho_{01}v_{A1}} \left( F(t - z/v_{A1}) - \frac{v_{A2} - v_{A1}}{v_{A2} + v_{A1}} F(t + (z - 2L)/v_{A1}) \right) \quad (3.19)$$

$$\times \left( \frac{\partial F}{\partial t}(t - z/v_{A1}) + \frac{v_{A2} - v_{A1}}{v_{A2} + v_{A1}} \frac{\partial F}{\partial t}(t + (z - 2L)/v_{A1}) \right). \quad (3.20)$$

We look for the solution to this equation in the form

$$V_{Z2} = V_{Z2i}(t - z/v_{A1}) + V_{Z2r}(t + z/v_{A1}) + V_{Z2n}(t, z). \quad (3.21)$$

The first and second terms on the right-hand side of this equation correspond to the incoming and reflected waves, respectively. The third term,  $V_{Z2n}$ , describes the interaction between the incoming and reflected waves. The three terms on the right-hand side of Eq. (3.21) are defined by the expressions

$$\frac{\partial V_{Z2i}}{\partial t} = \frac{F(t - z/v_{A1})}{\mu_0\rho_{01}v_{A1}} \frac{\partial F}{\partial t}(t - z/v_{A1}), \quad (3.22)$$

$$\frac{\partial V_{Z2r}}{\partial t} = -\left( \frac{v_{A2} - v_{A1}}{v_{A2} + v_{A1}} \right)^2 \frac{F(t + (z - 2L)/v_{A1})}{\mu_0\rho_{01}v_{A1}} \frac{\partial F}{\partial t}(t + (z - 2L)/v_{A1}), \quad (3.23)$$

$$\begin{aligned} \frac{\partial V_{Z2n}}{\partial t} = & \frac{v_{A2} - v_{A1}}{\mu_0 \rho_{01} v_{A1} (v_{A2} + v_{A1})} \left( F(t - z/v_{A1}) \frac{\partial F}{\partial t}(t + (z - 2L)/v_{A1}) \right. \\ & \left. - F(t + (z - 2L)/v_{A1}) \frac{\partial F}{\partial t}(t - z/v_{A1}) \right). \end{aligned} \quad (3.24)$$

The functions of  $V_{Z2i}$ ,  $V_{Z2r}$ , and  $V_{Z2n}$  are not uniquely defined. In particular, we can impose any initial conditions on these functions satisfying the restriction that their sum is zero at  $t = 0$ . We impose the condition

$$V_{Z2i} = V_{Z2r} = V_{Z2n} = 0 \quad \text{at } t = 0. \quad (3.25)$$

Then, it immediately follows from Eqs. (3.22) and (3.23) that

$$V_{Z2i} = \frac{1}{2\mu_0 \rho_{01} v_{A1}} F^2(t - z/v_{A1}), \quad (3.26)$$

$$V_{Z2r} = -\frac{1}{2\mu_0 \rho_{01} v_{A1}} \left( \frac{v_{A2} - v_{A1}}{v_{A2} + v_{A1}} \right)^2 F^2(t + (z - 2L)/v_{A1}). \quad (3.27)$$

On the other hand, we cannot integrate Eq. (3.24) with arbitrary function  $F$ . To calculate  $V_{Z2n}$  we need to specify function  $F$ . It is straightforward to see that  $V_{Z2r} = 0$  for  $t \leq L/v_{A1}$ . Since the right-hand side of Eq. (3.24) is zero for  $t \leq L/v_{A1}$  and  $V_{Z2n} = 0$  at  $t = 0$ , it follows that  $V_{Z2n} = 0$  for  $t \leq L/v_{A1}$ . Hence,  $V_{Z2} = V_{Z2i}$  for  $t \leq L/v_{A1}$  as it can be expected.

Although we cannot obtain the general expression for  $V_{Z2n}$ , we can calculate this quantity at  $z = L$ . Since the right-hand side of Eq. (3.24) is zero at  $z = L$ , it follows that from the boundary condition Eq. (3.25) that  $V_{Z2n} = 0$  at  $z = L$ . Then it is straightforward to verify that  $V_{Z2n}$  is continuous at  $z = L$ , as it should be.

Now, we proceed to solving Eq. (3.18) above the discontinuity and take  $z > L$ . Using Eq. (3.15) we reduce Eq. (3.18) to

$$\begin{aligned} \frac{\partial V_{Z2}}{\partial t} = & \frac{4v_{A2}}{\mu_0 \rho_{01} (v_{A2} + v_{A1})^2} F(t - L/v_{A1} - (z - L)/v_{A2}) \\ & \times \frac{\partial F}{\partial t}(t - L/v_{A1} - (z - L)/v_{A2}). \end{aligned} \quad (3.28)$$

When deriving this equation we used the identity  $\rho_{01} v_{A1}^2 = \rho_{02} v_{A2}^2$ . Using the condition that  $V_{Z2} = 0$  for  $t \leq 0$  we obtain from Eq. (3.28)

$$V_{Z2} = \frac{2v_{A2}}{\mu_0 \rho_{01} (v_{A2} + v_{A1})^2} F^2(t - L/v_{A1} - (z - L)/v_{A2}), \quad z > L. \quad (3.29)$$

### 3.3 Mass flux

Next, let us calculate the relative mass transmitted through the discontinuity. The incoming mass flux is equal to the instantaneous mass flux at  $z = 0$  integrated over the time interval  $[0, \tau]$  and over the tube cross-section. As a result, we obtain that the total mass flux of the tube cross-section is

$$M_i = \rho_{01} \int_0^R r \int_0^\tau V_{Z2i} dt dr = \frac{1}{2\mu_0 v_{A1}} \int_0^R r \int_0^\tau F^2(t, r) dt dr. \quad (3.30)$$

To obtain the total transmitted mass flux we integrate the instantaneous mass flux at any  $z > L$  over the time interval  $(-\infty, \infty)$ , although, of course,  $V_{Z2t}$  is different from zero only on a finite time interval. Hence,

$$\begin{aligned} M_t &= \rho_{02} \int_0^R r \int_{-\infty}^{\infty} V_{Z2t} dt dr \\ &= \frac{2v_{A1}^2}{\mu_0 v_{A2} (v_{A2} + v_{A1})^2} \int_0^R r \int_0^\tau F^2(t, r) dt dr. \end{aligned} \quad (3.31)$$

The relative mass flux is

$$\frac{M_t}{M_i} = \frac{4v_{A1}^3}{v_{A2}(v_{A2} + v_{A1})^2}. \quad (3.32)$$

Shown in Figure 3.2 is a plot of the mass flux ratio given by Eq. (3.32), as a function of the Alfvén speed ratio. Note that this ratio does not depend on the specification of  $F$ . If we take as a typical value  $v_{A2}/v_{A1} = 10$ , then we obtain  $M_t/M_i \approx 0.0033$ , that is only about 0.33% of the incoming mass is transmitted through the discontinuity. Also shown in the figure is the 1% line, corresponding to the percentage of the mass flux of spicules estimated to be equal to the mass flux of the solar wind (De Pontieu et al., 2004). This value of transmitted mass flux is reached at  $v_{A2}/v_{A1} \approx 6.72$ .

### 3.4 Pulse example

In a similar way to Section 2.4.2, we now take  $F(t, r) = B_{\max} H(t)G(r)$ , where

$$H(t) = \sin(\pi t/\tau), \quad 0 \leq t \leq \tau, \quad (3.33)$$

$$G(r) = \sin(\pi (r/R_0)^\sigma), \quad 0 \leq r \leq R_0, \quad (3.34)$$

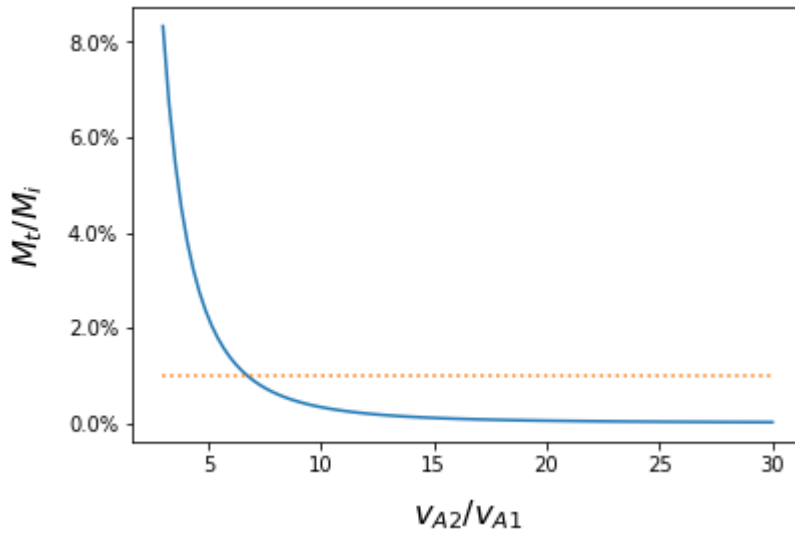


Figure 3.2: A plot of the mass flux ratio  $M_t/M_i$  as a function of the Alfvén speed ratio  $v_{A2}/v_{A1}$ . The range for the Alfvén speed ratio represents realistic values for the parameters, with smaller values excluded for clarity; we must have  $v_{A2} > v_{A1}$  (100% transmission is reached at  $v_{A2}/v_{A1} = 1$ ). The dotted line highlights the 1% transmission threshold which is reached at  $v_{A2}/v_{A1} \approx 6.72$ .

where  $H$  and  $G$  are zero otherwise,  $\tau$  is the characteristic time, and  $B_{\max}$  and  $\sigma = 0.25$  (chosen for the purpose of this example) are constants. This option of  $F(t, r)$  results in a localised perturbation.

Therefore, we have

$$B_{\theta 1i}(t - z/v_{A1}) = B_{\max} \sin\left(\frac{\pi}{\tau}(t - z/v_{A1})\right) \sin(\pi(r/R_0)^\sigma), \quad (3.35)$$

$$B_{\theta 1r}(t + z/v_{A1}) = \frac{B_{\max}(v_{A1} - v_{A2})}{v_{A1} + v_{A2}} \times \sin\left(\frac{\pi}{\tau}(t + (z - 2L)/v_{A1})\right) \sin(\pi(r/R_0)^\sigma), \quad (3.36)$$

so for  $z < L$ ,

$$B_{\theta 1} = B_{\max} \sin(\pi(r/R_0)^\sigma) \times \left( \sin\left(\frac{\pi}{\tau}(t - z/v_{A1})\right) + \frac{v_{A1} - v_{A2}}{v_{A1} + v_{A2}} \sin\left(\frac{\pi}{\tau}(t + (z - 2L)/v_{A1})\right) \right). \quad (3.37)$$

It follows from Eqs. (3.26) and (3.27) that

$$V_{Z2i} = \frac{B_{\max}^2}{2\mu_0\rho_{01}v_{A1}} \sin^2\left(\frac{\pi}{\tau}(t - z/v_{A1})\right) \sin^2(\pi(r/R_0)^\sigma), \quad (3.38)$$

$$V_{Z2r} = -\frac{B_{\max}^2}{2\mu_0\rho_{01}v_{A1}} \left(\frac{v_{A1} - v_{A2}}{v_{A1} + v_{A2}}\right)^2 \times \sin^2\left(\frac{\pi}{\tau}(t + (z - 2L)/v_{A1})\right) \sin^2(\pi(r/R_0)^\sigma), \quad (3.39)$$

and from Eq. (3.24),

$$\frac{\partial V_{Z2n}}{\partial t} = G^*(r) \left[ \sin\left(\frac{\pi}{\tau}(t - z/v_{A1})\right) \cos\left(\frac{\pi}{\tau}\left(t + \frac{z - 2L}{v_{A1}}\right)\right) - \sin\left(\frac{\pi}{\tau}\left(t + \frac{z - 2L}{v_{A1}}\right)\right) \cos\left(\frac{\pi}{\tau}(t - z/v_{A1})\right) \right], \quad (3.40)$$

where

$$G^*(r) = \frac{\pi B_{\max}^2}{\tau\mu_0\rho_{01}v_{A1}} \left(\frac{v_{A2} - v_{A1}}{v_{A1} + v_{A2}}\right) \sin^2(\pi(r/R_0)^\sigma). \quad (3.41)$$

Equation (3.40) is only valid when the following two inequalities are satisfied:

$$0 < t - \frac{z}{v_{A1}} < \tau, \quad 0 < t + \frac{z - 2L}{v_{A1}} < \tau. \quad (3.42)$$

When at least one of these inequalities is violated we have  $\partial V_{Z2n}/\partial t = 0$ . Then, after simple algebra, we obtain

$$\frac{\partial V_{Z2n}}{\partial t} = \begin{cases} G^*(r) \sin\left(\frac{2\pi(L-z)}{v_{A1}\tau}\right), & \frac{2L-z}{v_{A1}} < t < \frac{z}{v_{A1}} + \tau, \\ 0, & \text{otherwise.} \end{cases} \quad (3.43)$$

In particular, it follows from this equation that  $\partial V_{Z2n}/\partial t = 0$  for  $z < L - \frac{1}{2}\tau v_{A1}$ , because in this case  $(2L-z)/v_{A1} > z/v_{A1} + \tau$ . Then, it follows that for any time

$$V_{Z2n} = 0 \quad \text{for } z < L - \frac{\tau v_{A1}}{2}. \quad (3.44)$$

Next, for  $L - \frac{1}{2}\tau v_{A1} < z < L$  we obtain

$$V_{Z2n} = \begin{cases} 0, & t < \frac{2L-z}{v_{A1}}, \\ G^*(r) \sin\left(\frac{2\pi(L-z)}{v_{A1}\tau}\right) \left(t - \frac{2L-z}{v_{A1}}\right), & \frac{2L-z}{v_{A1}} < t < \frac{z}{v_{A1}} + \tau, \\ G^*(r) \sin\left(\frac{2\pi(L-z)}{v_{A1}\tau}\right) \left(\tau - \frac{2L-2z}{v_{A1}}\right), & t > \frac{z}{v_{A1}} + \tau. \end{cases} \quad (3.45)$$

### 3.5 Restrictions

A noteworthy result is that  $V_{Z2n}$  is non-zero and is independent of  $t$  for  $t > z/v_{A1} + \tau$  and  $L - \frac{1}{2}\tau v_{A1} < z < L$ . We show that because of these conditions, our solution is only valid on a finite time interval. We collect terms of the order of  $\epsilon^2$  in Eq. (3.1) to obtain

$$\frac{\partial \rho_2}{\partial t} + \frac{\rho_{01}}{r} \frac{\partial(rV_{R2})}{\partial r} + \rho_{01} \frac{\partial V_{Z2}}{\partial z} = 0. \quad (3.46)$$

We consider this equation for  $L - \frac{1}{2}\tau v_{A1} < z < L$  and  $t > (2L-z)/v_{A1} + \tau$ . The second inequality guarantees that  $V_{Z2i} = V_{Z2r} = 0$ . Now, we integrate Eq. (3.46) over a cross-section  $z = \text{const}$ . This yields

$$\frac{\partial}{\partial t} \int_0^R r \rho_2 dr = \frac{2\rho_{01}}{v_{A1}} W(z) - \rho_{01} R V_{R2}(t, R, z), \quad (3.47)$$

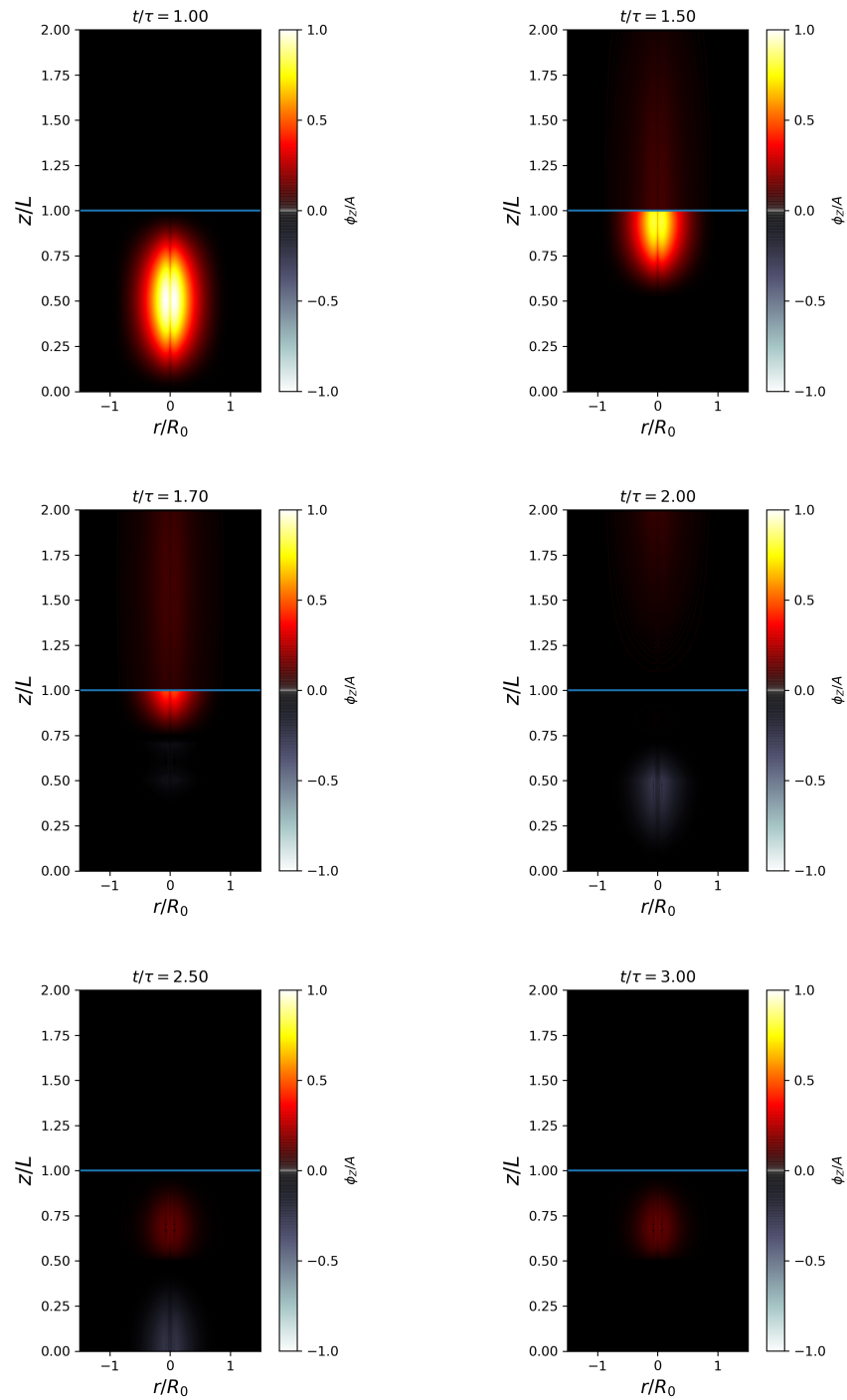


Figure 3.3: (Caption next page.)

Figure 3.3: (Previous page.) Contour plots at various times showing the relative mass flux  $\phi_z = \rho V_z$  for the given example — in this particular representation we have chosen  $L = v_{A1}\tau$ , for simplicity, and we have specified  $v_{A2}/v_{A1} = 3$  so that both the reflected and transmitted waves are visible. The value of the mass flux indicated by the colorbar is scaled relative to the maximum magnitude of the initial pulse, denoted  $A$ . The initial wave results in positive (upwards) mass flux shown in orange whilst the reflected wave results in negative (downwards) flux, potentially echoing the rising and falling behaviour of a spicule. In addition, the lower three images show the formation of the lingering mass flux which forms after the reflection, due to the non-linear interaction between the initial and reflected waves. An animation of this figure is available, showing the full evolution of the plasma perturbation leading up to and between the still images shown in the figure, from  $t/\tau = 0$  to  $t/\tau = 3$  where this duration has been scaled to 9 seconds.

where

$$W(z) = \left[ \pi \left( 1 - \frac{2L - 2z}{\tau v_{A1}} \right) \cos \left( \frac{2\pi(L - z)}{v_{A1}\tau} \right) - \sin \left( \frac{2\pi(L - z)}{v_{A1}\tau} \right) \right] \times \int_0^R G^*(r)r dr. \quad (3.48)$$

We note that the first term on the right-hand side of Eq. (3.47) is independent of time. If  $V_{R2}(t, R, z) \rightarrow 0$  as  $t \rightarrow \infty$  then it follows from Eq. (3.47) that  $\int_0^R r \rho_2 dr$  linearly grows with time for large  $t$ . This, in turn, implies that  $\rho_2$  is unbounded with respect to time. This conclusion is only incorrect if  $RV_{R2}(t, R, z) \rightarrow 2W(z)/v_{A1}$  as  $t \rightarrow \infty$ . Let us assume that this condition is satisfied. We consider the equation of the perturbed magnetic tube boundary  $r = R + \eta(t, z)$ . Next we write the kinematic boundary condition at the tube boundary,

$$V_R = \frac{\partial \eta}{\partial t} + V_Z \frac{\partial \eta}{\partial z}. \quad (3.49)$$

The quantity  $\eta$  can also be expanded in the power series of the form given by Eq. (3.4). Collecting term of the order of  $\epsilon^2$  in Eq. (3.49) yields

$$V_{R2} = \frac{\partial \eta_2}{\partial t}. \quad (3.50)$$

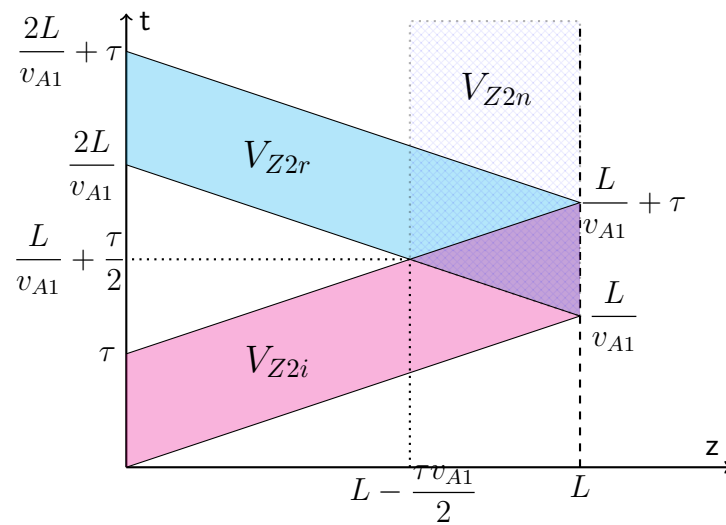


Figure 3.4: A diagram clarifying the interaction between the incoming and reflected waves. The velocity in the incoming wave is non-zero in the pink strip, and it is non-zero in the reflected wave in the blue strip. The dark lilac / crosshatched triangle is the region where the two waves interact. In this region the right-hand side of Eq. (3.43) is non-zero.  $V_{Z2n}$  is non-zero in this triangle as well as in the crosshatched vertical strip above it.

Since  $V_{R2}$  tends to a non-zero limit as  $t \rightarrow \infty$ , it follows that  $\eta_2$  grows linearly for large  $t$ .

Hence, we obtained that either  $\rho_2$  or  $\eta_2$  (or both of them) is unbounded for large  $t$ . When using the regular perturbation method with the expansion of all variables given by Eq. (3.4) we assumed that that any next term is much smaller than the previous one. In particular, this implies that our method fails when the coefficient at  $\epsilon^2$  becomes of the order of  $\epsilon^{-1}$  because in this case the term proportional to  $\epsilon^2$  becomes of the same order as the term proportional to  $\epsilon$ . We can give a rough estimate of the critical time  $t_c$  after which our solution becomes invalid,

$$t_c = \tau\epsilon^{-1}. \quad (3.51)$$

We need to have our analysis valid at least until the perturbation reaches the discontinuity. This condition gives  $t_c > L/v_{A1}$ , which is equivalent to  $\tau v_{A1} > \epsilon L$ .

### 3.6 Discussion

The mass flux is a second-order effect, driven by the Lorentz force resulting from the first-order Alfvén wave perturbation. The result complements the previous models in Oxley et al. (2020); Scalisi et al. (2021a) as we have the same initial mass flux, followed by the downwards flux provided by the reflected wave which makes the model potentially applicable to both Type I and II spicules as discussed in De Pontieu et al. (2007b). The example pulse given in Section 3.4 allows us to examine and visualise the complete secondary non-linear perturbation including the interaction term. It is straightforward to verify that  $V_{Z2} = V_{Z2i} + V_{Z2r} + V_{Z2n}$  is continuous in the region  $0 \leq z < L$  and for  $t \geq 0$  (see Appendix A). We can also verify that  $V_{Z2}$  is continuous at  $z = L$ .

Our analysis of the mass flux ratio in Section 3.2.3 may suggest that the distinction between spicule types could be attributed to localised differences in the relative densities of the chromosphere/transition region (equivalently, the difference in Alfvén speed). Spicules that do not simply fade away have

been observed to follow parabolic trajectories (De Pontieu et al., 2007b), with their maximum deceleration approximately matching their initial acceleration. We may theorise that, if this reflection effect is indeed related to spicule behaviour, then the reflected wave may correspond to parabolic spicule motion associated with Type I spicules. Considering our results, both the initial and reflected waves propagate at the (chromospheric) Alfvén speed in opposing directions, which can be estimated for the special case of our highly magnetic flux tube on the order of around  $10 \text{ km s}^{-1}$  (Beckers, 1968). The scale of the mass flux is difficult to estimate but we note that the relative magnitude of the initial and reflected wave is similar when the Alfvén speed ratio  $v_{A2}/v_{A1}$  is appropriately high.

In theory, a more strongly transmitted wave may correspond to Type II spicules which exhibit linear motion, or possibly might relate to jets that extend higher into the solar atmosphere such as macrospicules. The mass flux present above the discontinuity due to the transmitted wave, as a proportion of the mass flux resulting from the initial wave (our ‘mass flux ratio’) increases when the Alfvén speed ratio decreases. In that case, according to our model, we would expect these more linear jets to appear more commonly in regions where the change in atmospheric density at the transition region is smaller, i.e. where the Alfvén speed ratio is lower. However, there may be additional factors to consider that are beyond the scope of this model.

The time restriction for validity of our analysis is related to the fact that in the domain  $L - \frac{1}{2}\tau v_{A1} < z < L$  there is plasma flow with the velocity independent of time for  $t > z/v_{A1} + \tau$ . This flow results from the interaction of the incoming and reflected waves. This property of the two wave interaction is the direct consequence of neglecting the plasma pressure due to the zero-beta approximation. Taking account of plasma pressure would cause the decay of the velocity created by the wave interaction after the pulse had passed. However, in cases where wave reflection occurs and the magnetic pressure is strongly dominant, it is not unreasonable to suggest that a physical analogue of this hypothetical flow may exist — for example, jets are observed in the corona and upper chromosphere, and the flow may be related to these higher atmospheric jets. It is interesting that a similar prob-

lem of unbounded growth of perturbations caused by neglecting the plasma pressure arises in other problems of space physics. For example, Ruderman and Goossens (2014) studied non-linear kink oscillations of magnetic tubes in the cold plasma approximation. They obtained that the density perturbation linearly grows with time. To stop this unbounded growth the plasma pressure must be taken into account.

Although comparison with observations is useful, we can only speculate on some of the values used in our example due to the difficulty of obtaining accurate measurements of e.g. the density, in highly localised regions such as spicules. We are again left with the problem of the persistent mass flux resulting from the interaction term which may not be present if we considered gravity, more complex atmospheric stratification, dissipation / heating, or radiative losses — therefore these will need to be included in subsequent models. These factors are somewhat interconnected, for example the inclusion of gravity also requires atmospheric stratification, adding further complexity. We intentionally left gravity out of this model because we wanted to isolate and study the effect of the reflected Alfvén waves, in order to clearly understand what effect a discontinuity has on the generation of plasma perturbations. However, it is important to establish whether the proposed mechanism of a torsional Alfvén wave perturbation would be viable with these additional considerations.

## CHAPTER 4

---

### Effect of a Transitional Layer on Vertical Flows Generated by Torsional Alfvén Pulses

---

This chapter is based on Scalisi et al. (2023), published in *The Astrophysical Journal*.

In this chapter, we attempt to model the potential ability of spicules to affect the solar wind, by augmenting the existing model with the inclusion of a vertically stratified atmosphere in the form of a three-layered system representing the structure of the chromosphere. A finite transitional layer, in which the atmospheric density decreases exponentially, is sandwiched in between two constant-density layers which are similar to the model atmosphere in the previous chapters. This allows for more complexity and should create a more physical representation of the solar atmosphere, improving on our analytical investigation of solar jets.

Spicule activity in the chromosphere is modelled via the effect of a torsional Alfvén wave pulse propagating through plasma in a highly magnetic flux tube in the stratified atmosphere. The wave pulse is introduced at the lower boundary and interacts with the transitional layer, also being partially reflected. The total mass flux induced by the pulse, and the proportion of this that is reflected vs transmitted through the layer, is calculated and exam-

ined in the context of spicules and the solar wind, using an example solution. We find that the inclusion of the transitional layer results in more plasma flux being transferred into the upper solar atmosphere, when compared with the case of a discontinuity. We examine how varying the parameters of this transitional layer affects the ratio of the flux above and below the layer.

## 4.1 Background and motivation

Since spicules occur throughout the chromosphere (Sterling, 2000; Tsiropoula et al., 2012) — a region dominated by dynamic features and which separates the relatively cold, dense plasma of the photosphere from the extremely hot corona — the conditions in the local environment of such jets may be inhomogeneous.

Despite being relatively thin when compared to the extent of the corona or the scale of the solar interior, the chromosphere and transition region form an area of the solar atmosphere over which extreme changes occur e.g. in density (Makita, 2003). Plasma density is generally thought to decrease near-exponentially with height, ranging from the order of  $10^{-4}$  kg m<sup>-3</sup> at the level of the photosphere (Roberts, 2019) up to around  $10^{-11}$  kg m<sup>-3</sup> in the transition region (Priest, 2014). Models of the solar atmosphere as a whole have been able to take this density variation into account (Ferraro and Plumpton, 1958; Vernazza et al., 1981), however, more research is needed to determine how this affects the evolution of spicules and their effect on the outer solar atmosphere.

In Chapters 2 and 3, an analytical model was developed to investigate the influence of torsional waves on the generation and early evolution of spicules, and the effects of wave reflection from a discontinuity. However, the vertical stratification of the chromosphere from the footpoints of spicules up to their maximum height (a distance of several thousand kilometers — see Section 1.6.1), is also likely to affect their later evolution and decline. In this regard, here we continue our efforts to build a model which can take into account the inhomogeneous nature of the chromosphere, i.e. the variation in the properties of the atmospheric plasma that occurs as the height above the

photosphere increases.

Whereas Scalisi et al. (2021b) involved a discontinuity from which Alfvén waves were reflected, we now include a more realistic continuous density profile that may give significantly different results. Hence, we aim to investigate how the vertical mass flux resulting from a torsional perturbation is transferred from the chromosphere to the corona, and how this depends on the thickness of a transitional layer. This layer is intended to represent the fact that the most extreme variation of plasma density in the solar atmosphere occurs over a relatively thin region of the upper chromosphere. We are interested in how the stratification of the atmosphere affects the plasma flux into the outer atmosphere, i.e. the difference between the perturbation below and above the transitional layer. In the next section we describe the equilibrium state and present the governing equations of the model.

## 4.2 Transitional layer model

In this analytical model, beginning with the ideal MHD equations and following on from the method of Scalisi et al. (2021a), we consider a magnetic flux tube which acts as a waveguide for an Alfvén wave pulse. In this context, the vertical background magnetic field is assumed to be strong enough that magnetic forces dominate throughout the tube and thus the plasma beta is much less than unity (Jess et al., 2023). We therefore use the zero-beta approximation and neglect the plasma pressure in comparison with the magnetic forces. The perturbation in the magnetic field generates vertical plasma motion via the ponderomotive Lorentz force.

The structure of the atmosphere is modelled as a three-layered system, with the initial pulse generated in the lower region with constant plasma density, passing through the an intermediary transitional layer in which the density decreases, and finally propagating into another region with low constant density. We consider the plasma motion inside a vertical semi-infinite axisymmetric magnetic tube of radius  $r_0$ . We use cylindrical coordinates  $(r, \theta, z)$  with the  $z$ -axis vertical. The equilibrium magnetic field is in the  $z$ -direction and has a constant magnitude  $B_0$ . We consider the tube bound-

ary to be rigid and disregard the interaction of plasma motion inside the tube with the plasma surrounding it. The tube consists of three regions with different plasma densities inside them. The transitional layer is defined by  $L \leq z \leq L + \ell$ , i.e. it begins at some height  $L$  above the base of the chromosphere and has a vertical extent or thickness of  $\ell$ . We assume that the density  $\rho(z)$  in the transitional layer decreases exponentially, hence the equilibrium plasma density is given by

$$\rho_0(z) = \begin{cases} \rho_1, & 0 \leq z \leq L, \\ \rho_1 \exp((L - z)/H), & L < z < L + \ell, \\ \rho_2, & z \geq L + \ell. \end{cases} \quad (4.1)$$

Here,  $H$  is the scale height in the transitional layer, and  $\rho_1$  and  $\rho_2$  are constants related by  $\rho_2 = \rho_1 e^{-\ell/H}$ . The plasma motion is described by the ideal magnetohydrodynamic (MHD) equations for cold plasmas:

$$\frac{\partial \mathbf{v}}{\partial t} + (\mathbf{v} \cdot \nabla) \mathbf{v} = \frac{1}{\mu_0 \rho} (\nabla \times \mathbf{B}) \times \mathbf{B}, \quad (4.2)$$

$$\frac{\partial \mathbf{B}}{\partial t} = \nabla \times (\mathbf{v} \times \mathbf{B}), \quad (4.3)$$

where  $\mathbf{v} = (v_r, v_\theta, v_z)$  is the plasma velocity,  $\mathbf{B} = (B_r, B_\theta, B_z)$  the magnetic field,  $\rho$  the plasma density, and  $\mu_0$  the magnetic permeability of free space. The Alfvén speed,  $v_A$ , is defined by

$$v_A^2 = \frac{B_0^2}{\mu_0 \rho_0}, \quad v_A(z) = v_{A1} e^{(z-L)/2H}, \quad (4.4)$$

where  $v_{A1} = v_A(L)$  is the (constant) Alfvén speed below the transitional layer and  $H$  is the scale height. It follows that  $v_{A2} = v_{A1} e^{\ell/2H}$  is the Alfvén speed above the transitional layer.

Below, we consider the motion with small dimensionless amplitude  $\epsilon \ll 1$  and we look for a solution to the problem in the form of expansions

$$\mathbf{v} = \epsilon \mathbf{V}_1 + \epsilon^2 \mathbf{V}_2 + \dots, \quad \mathbf{B} = B_0 \mathbf{e}_z + \epsilon \mathbf{B}_1 + \epsilon^2 \mathbf{B}_2 + \dots, \quad (4.5)$$

where  $\mathbf{e}_z$  is the unit vector in the  $z$ -direction. We impose the boundary condition at the tube base

$$B_\theta = \epsilon F(t, r), \quad V_\theta = -\frac{\epsilon v_{A1}}{B_0} F(t, r) \quad \text{at } z = 0, \quad (4.6)$$

where  $F(t, r)$  is a function that defines a localised finite-duration pulse inside the flux tube. This will drive a torsional Alfvén wave propagating upwards in the first-order approximation; we will then investigate the effect that this has on the second-order quantities.

### 4.3 First-order approximation

In the first-order approximation, we collect the terms of the order of  $\epsilon$  and then look for the solution of obtained equations in the form of torsional wave. In this wave only  $V_{\theta 1}$  and  $B_{\theta 1}$  are non-zero, while other components of the velocity and magnetic field perturbation are zero. The torsional velocity and magnetic perturbations  $V_{\theta 1}$  and  $B_{\theta 1}$  are therefore related by the first-order equation of motion,

$$\frac{\partial V_{\theta 1}}{\partial t} - \frac{v_A^2}{B_0} \frac{\partial B_{\theta 1}}{\partial z} = 0, \quad (4.7)$$

as well as the first-order induction equation,

$$\frac{\partial B_{\theta 1}}{\partial t} = \frac{\partial V_{\theta 1}}{\partial z} B_0. \quad (4.8)$$

Combining Eqs. (4.7) and (4.8), the first-order velocity perturbation is then defined by the equation

$$\frac{\partial^2 V_{\theta 1}}{\partial t^2} - v_A^2(z) \frac{\partial^2 V_{\theta 1}}{\partial z^2} = 0. \quad (4.9)$$

The solution for the velocity below and above the transitional layer is given by

$$V_{\theta 1} = \begin{cases} V_{\theta 1i}(t - z/v_{A1}) + V_{\theta 1r}(t + z/v_{A1}), & z \leq L, \\ V_{\theta 1t}(t - z/v_{A2}), & z \geq L + \ell. \end{cases} \quad (4.10)$$

A similar solution for the magnetic field is

$$B_{\theta 1} = \begin{cases} B_{\theta 1i}(t - z/v_{A1}) + B_{\theta 1r}(t + z/v_{A1}), & z \leq L, \\ B_{\theta 1t}(t - z/v_{A2}), & z \geq L + \ell. \end{cases} \quad (4.11)$$

### 4.3.1 Fourier transform

To find a solution for Eq. (4.9) in the transitional layer we introduce the Fourier transform with respect to time,

$$\hat{f}(\omega) = \int_{-\infty}^{\infty} f(t)e^{-i\omega t} dt, \quad f(t) = \frac{1}{2\pi} \int_{-\infty}^{\infty} \hat{f}(\omega)e^{i\omega t} d\omega. \quad (4.12)$$

Applying this transform to Eq. (4.9) and using Eq. (4.4) yields

$$\frac{\partial^2 \hat{V}_{\theta 1}}{\partial z^2} + \frac{\omega^2 e^{-(z-L)/H}}{v_{A1}^2} \hat{V}_{\theta 1} = 0. \quad (4.13)$$

This equation is valid for  $L \leq z \leq L + \ell$ . Using the variable substitution,

$$u = \frac{2H\omega}{v_{A1}} \exp\left(-\frac{z-L}{2H}\right), \quad \frac{\partial u}{\partial z} = -\frac{u}{2H}, \quad \frac{\partial^2 u}{\partial z^2} = \frac{u}{4H^2}, \quad (4.14)$$

so that

$$\frac{\partial \hat{V}_{\theta 1}}{\partial z} = -\frac{u}{2H} \frac{\partial \hat{V}_{\theta 1}}{\partial u}, \quad \frac{\partial^2 \hat{V}_{\theta 1}}{\partial z^2} = \frac{u}{4H^2} \left( u \frac{\partial^2 \hat{V}_{\theta 1}}{\partial u^2} + \frac{\partial \hat{V}_{\theta 1}}{\partial u} \right), \quad (4.15)$$

then by substituting in (4.14) and (4.15) we reduce Eq. (4.13) to the Bessel equation

$$u^2 \frac{\partial^2 \hat{V}_{\theta 1}}{\partial u^2} + u \frac{\partial \hat{V}_{\theta 1}}{\partial u} + u^2 \hat{V}_{\theta 1} = 0. \quad (4.16)$$

The general solution to this equation for  $\hat{V}_{\theta 1}$  is

$$\hat{V}_{\theta 1} = C_1(\omega) J_0(u) + C_2(\omega) Y_0(u), \quad (4.17)$$

where  $J_0(u)$  and  $Y_0(u)$  are Bessel functions of the first and second type and the zero order.

After applying the Fourier transform to the induction equation (4.8), we obtain

$$\hat{B}_{\theta 1} = \frac{B_0}{i\omega} \frac{\partial \hat{V}_{\theta 1}}{\partial z} = \frac{i u B_0}{2H\omega} \frac{\partial \hat{V}_{\theta 1}}{\partial u}. \quad (4.18)$$

Using the relations

$$J'_0(u) = -J_1(u), \quad Y'_0(u) = -Y_1(u), \quad (4.19)$$

where  $J_1(u)$  and  $Y_1(u)$  are Bessel functions of the first and second type and the first order, and the prime indicates the derivative, we obtain from Eqs. (4.17) and (4.18)

$$\hat{B}_{\theta 1} = -\frac{i u B_0}{2 H \omega} [C_1(\omega) J_1(u) + C_2(\omega) Y_1(u)]. \quad (4.20)$$

Applying the Fourier transform to Eqs. (4.10) and (4.11) we obtain

$$\hat{V}_{\theta 1} = \begin{cases} e^{-i \omega z / v_{A1}} \hat{V}_{\theta 1 i}(\omega) + e^{i \omega z / v_{A1}} \hat{V}_{\theta 1 r}(\omega), & z \leq L, \\ e^{-i \omega z / v_{A2}} \hat{V}_{\theta 1 t}(\omega), & z \geq L + \ell. \end{cases} \quad (4.21)$$

$$\hat{B}_{\theta 1} = \begin{cases} e^{-i \omega z / v_{A1}} \hat{B}_{\theta 1 i}(\omega) + e^{i \omega z / v_{A1}} \hat{B}_{\theta 1 r}(\omega), & z \leq L, \\ e^{-i \omega z / v_{A2}} \hat{B}_{\theta 1 t}(\omega), & z \geq L + \ell. \end{cases} \quad (4.22)$$

We note that  $\hat{B}_{\theta 1}$  and  $\hat{V}_{\theta 1}$  are functions of  $z$  that depend on  $\omega$  and  $r$  as parameters.

The magnetic field and velocity must be continuous at the boundaries of the transitional layer. This condition results in

$$\begin{aligned} e^{-i \omega L / v_{A1}} \hat{V}_{\theta 1 i}(\omega) + e^{i \omega L / v_{A1}} \hat{V}_{\theta 1 r}(\omega) &= C_1(\omega) J_0(u_1) + C_2(\omega) Y_0(u_1), \\ e^{-i \omega (L + \ell) / v_{A2}} \hat{V}_{\theta 1 t}(\omega) &= C_1(\omega) J_0(u_2) + C_2(\omega) Y_0(u_2), \\ e^{-i \omega L / v_{A1}} \hat{B}_{\theta 1 i}(\omega) + e^{i \omega L / v_{A1}} \hat{B}_{\theta 1 r}(\omega) &= -\frac{i B_0}{v_{A1}} [C_1(\omega) J_1(u_1) + C_2(\omega) Y_1(u_1)], \\ e^{-i \omega (L + \ell) / v_{A2}} \hat{B}_{\theta 1 t}(\omega) &= \frac{-i B_0 e^{-\ell / 2H}}{v_{A1}} [C_1(\omega) J_1(u_2) + C_2(\omega) Y_1(u_2)], \end{aligned} \quad (4.23)$$

where

$$u_1 = u(z = L) = \frac{2 H \omega}{v_{A1}}, \quad u_2 = u(z = L + \ell) = \frac{2 H \omega}{v_{A1}} \exp\left(-\frac{\ell}{2 H}\right). \quad (4.24)$$

We impose the boundary condition

$$B_{\theta 1} = F(t, r) \quad \text{at } z = 0. \quad (4.25)$$

Using Eq. (4.7) and the definitions of  $B_{\theta 1}$  and  $V_{\theta 1}$  we obtain the relations

$$V_{\theta 1 i} = -\frac{v_{A1}}{B_0} B_{\theta 1 i}, \quad V_{\theta 1 r} = \frac{v_{A1}}{B_0} B_{\theta 1 r}, \quad V_{\theta 1 t} = -\frac{v_{A2}}{B_0} B_{\theta 1 t}. \quad (4.26)$$

The same relations are valid for the Fourier transforms of the velocity and magnetic field. Then, we transform the third and fourth equations in Eq. (4.23) to

$$e^{-i\omega L/v_{A1}}\hat{V}_{\theta 1i}(\omega) - e^{i\omega L/v_{A1}}\hat{V}_{\theta 1r}(\omega) = i[C_1(\omega)J_1(u_1) + C_2(\omega)Y_1(u_1)], \quad (4.27)$$

$$e^{-i\omega(L+\ell)/v_{A2}}\hat{V}_{\theta 1t}(\omega) = i[C_1(\omega)J_1(u_2) + C_2(\omega)Y_1(u_2)]. \quad (4.28)$$

We need to be able to write  $V_{\theta 1t}$  in terms of  $V_{\theta 1i}$  in order to find the mass flux ratio when we solve the second-order approximation for  $V_{Z2}$ . We obtain by adding Eq. (4.27) and the first equation in Eq. (4.23),

$$C_1(\omega)[J_0(u_1) + iJ_1(u_1)] + C_2(\omega)[Y_0(u_1) + iY_1(u_1)] = 2e^{-i\omega L/v_{A1}}\hat{V}_{\theta 1i}(\omega). \quad (4.29)$$

Subtracting Eq. (4.28) from the second equation in Eq. (4.23), we obtain

$$C_1(\omega)[J_0(u_2) - iJ_1(u_2)] + C_2(\omega)[Y_0(u_2) - iY_1(u_2)] = 0. \quad (4.30)$$

It follows from Eqs. (4.29) and (4.30) that

$$C_1(\omega) = 2e^{-i\omega L/v_{A1}}\hat{V}_{\theta 1i}(\omega) \frac{(Y_0(u_2) - iY_1(u_2))}{G(\omega)} \quad (4.31)$$

$$C_2(\omega) = -2e^{-i\omega L/v_{A1}}\hat{V}_{\theta 1i}(\omega) \frac{(J_0(u_2) - iJ_1(u_2))}{G(\omega)}, \quad (4.32)$$

where

$$G(\omega) = [J_0(u_1) + iJ_1(u_1)][Y_0(u_2) - iY_1(u_2)] - [J_0(u_2) - iJ_1(u_2)][Y_0(u_1) + iY_1(u_1)]. \quad (4.33)$$

Eliminating  $C_1$  and  $C_2$  from Eq. (4.28) and using the identity (from Abramowitz and Stegun (1964))

$$J_{\nu+1}(x)Y_\nu(x) - J_\nu(x)Y_{\nu+1}(x) \equiv \frac{2}{\pi x}, \quad (4.34)$$

yields

$$\hat{V}_{\theta 1t}(\omega) = \frac{2iv_{A2}\hat{V}_{\theta 1i}(\omega)}{\pi\omega HG(\omega)}e^{-i\omega T}, \quad (4.35)$$

where

$$T = \frac{L}{v_{A1}} - \frac{L+\ell}{v_{A2}}. \quad (4.36)$$

Equation (4.35) is then the Fourier-transformed first-order azimuthal velocity perturbation and is the solution to Eq. (4.13). We do not give the expression for  $\hat{V}_{\theta 1r}(\omega)$  because it is not used below.

### 4.3.2 Inverse Fourier transforms

Now, let us calculate the inverse Fourier transforms. In order to make analytical progress, we first assume that  $F(t, r) = 0$  for  $t \leq 0$  and  $t \geq \tau$ . This means that there is no perturbation before an initial time  $t = 0$  and that the driver of the pulse is active only for a finite duration  $\tau$ , after which there is again no perturbation in the first-order quantities. The leading edge of torsional Alfvén wave, driven by the perturbation at  $z = 0$ , arrives at the lower boundary of the transitional layer at  $t = L/v_{A1}$ . Before it arrives at this lower boundary, it has the form of a pulse of length  $\tau v_{A1}$ . We assume that this length is much larger than the thickness of the transitional layer and introduce the small parameter  $\delta = \ell/\tau v_{A1}$ .

The main contribution in  $\hat{F}(\omega, r)$ , which is the Fourier transform of the function defined in Eq. (4.6), comes from  $|\omega|$  smaller than or of the order of  $2\pi/\tau$ , while  $|\hat{F}(\omega, r)| \ll 1$  for  $|\omega| \gg 2\pi/\tau$ , so that it is enough to consider the Fourier transform only for  $|\omega| \lesssim 2\pi/\tau$ . Since  $\ell/H = 2 \ln(v_{A2}/v_{A1})$  we have  $H \lesssim \ell$ , i.e. the scale height is of the order of, or less than, the thickness of the transitional layer. This enables us to obtain the following estimates,

$$|u_1| = \frac{2H|\omega|}{v_{A1}} \lesssim \frac{4\pi H}{\tau v_{A1}} \lesssim \frac{\ell}{\tau v_{A1}} = \delta \ll 1. \quad (4.37)$$

Since  $|u_2| < |u_1|$ , it follows that  $|u_2| \lesssim \delta$ . Below, in all expressions, we only keep terms of the order of unity,  $\delta$ , and  $\delta^2$ , and neglect terms of higher orders with respect to  $\delta$ .

Now, we use the relations (Abramowitz and Stegun (1964), ref. 9.1)

$$\begin{aligned} J_0(x) &= 1 - \frac{x^2}{4} + \mathcal{O}(x^4), & J_1(x) &= \frac{x}{2} + \mathcal{O}(x^3), \\ Y_0(x) &= \frac{2}{\pi} \left( \ln \frac{x}{2} + \gamma \right) \left( 1 - \frac{x^2}{4} \right) + \frac{x^2}{2\pi} + \mathcal{O}(x^4 \ln |x|), \\ Y_1(x) &= -\frac{2}{\pi x} + \frac{x}{\pi} \ln \frac{x}{2} + \frac{x}{2\pi} (2\gamma - 1) + \mathcal{O}(x^3 \ln |x|), \end{aligned} \quad (4.38)$$

where  $\gamma$  is the Euler constant. With these relations, we obtain

$$G(\omega) \approx \frac{i(v_{A2} + v_{A1})}{\pi H \omega} - \frac{\chi}{\pi} \left[ 1 + \frac{iH\omega}{v_{A1}} (1 - e^{-\ell/2H}) \right], \quad (4.39)$$

where

$$\chi = \frac{\ell}{H} - \left( \frac{v_{A1}}{v_{A2}} - \frac{v_{A2}}{v_{A1}} \right) = \frac{\ell}{H} + 2 \sinh \frac{\ell}{2H} \sim \mathcal{O}(1). \quad (4.40)$$

Using Eq. (4.39) and the identity

$$\frac{1}{1+x} = 1 - x + x^2 - x^3 + \dots \quad (4.41)$$

valid for  $|x| \ll 1$ , which is the case for

$$x = \frac{i\chi H\omega (1 + iH\omega (1/v_{A1} + 1/v_{A2}))}{v_{A1} + v_{A2}} \lesssim \mathcal{O}(\delta), \quad (4.42)$$

and taking only the first three terms (up to the order of  $\delta^2$ , since  $\delta \ll 1$  and therefore further terms will be very small in magnitude), we obtain from Eq. (4.35),

$$\hat{V}_{\theta 1t}(\omega) = \frac{2v_{A2}\hat{V}_{\theta 1i}(\omega)}{v_{A1} + v_{A2}} \left( 1 - \frac{i\chi H\omega}{v_{A1} + v_{A2}} - \frac{\chi\ell H\omega^2}{(v_{A1} + v_{A2})^2} \right) e^{-i\omega T}. \quad (4.43)$$

Then, we can calculate the inverse Fourier transforms:

$$\begin{aligned} V_{\theta 1t}(t) &= \frac{1}{2\pi} \int_{-\infty}^{\infty} \hat{V}_{\theta 1t}(\omega) e^{i\omega t} d\omega \\ &= \frac{v_{A2}}{\pi(v_{A1} + v_{A2})} \int_{-\infty}^{\infty} \left( 1 - \frac{i\chi H\omega}{v_{A1} + v_{A2}} - \frac{\chi\ell H\omega^2}{(v_{A1} + v_{A2})^2} \right) \hat{V}_{\theta 1i}(\omega) e^{i\omega(t-T)} d\omega \\ &= \frac{v_{A2}}{\pi(v_{A1} + v_{A2})^2} \left( 1 - \frac{\chi H}{v_{A1} + v_{A2}} \frac{\partial}{\partial t} + \frac{\chi\ell H}{(v_{A1} + v_{A2})^2} \frac{\partial^2}{\partial t^2} \right) \int_{-\infty}^{\infty} \hat{V}_{\theta 1i}(\omega) e^{i\omega(t-T)} d\omega \\ &= \frac{2v_{A2}}{v_{A1} + v_{A2}} \left[ V_{\theta 1i}(t-T) - \frac{\chi H V'_{\theta 1i}(t-T)}{v_{A1} + v_{A2}} + \frac{\chi\ell H V''_{\theta 1i}(t-T)}{(v_{A1} + v_{A2})^2} \right], \end{aligned} \quad (4.44)$$

where the prime indicates the derivative. Thus we have an approximate solution for the first-order equation (4.9).

## 4.4 Second-order approximation

Next, we consider the second-order quantities in the MHD equations, which depend on the solutions we have found for the first-order quantities. This will introduce a vertical perturbation of the plasma due to the ponderomotive Lorentz force.

In the second-order approximation, we collect the terms of the order of  $\epsilon^2$  in the  $z$ -component in Eq. (4.2). This yields

$$\frac{\partial V_{z2}}{\partial t} = -\frac{1}{2\mu_0\rho_0(z)} \frac{\partial}{\partial z} (B_{\theta 1}^2). \quad (4.45)$$

The torsional Alfvén wave arrives at the transitional layer at  $t = L/v_{A1}$ . Before that time there is no reflected wave in the region  $z < L$ , i.e.  $V_{\theta 1} = V_{\theta 1i}$ . Hence, for  $t < L/v_{A1}$  we obtain using Eqs. (4.8), (4.26), and (4.45) that below the transitional layer,

$$\frac{\partial V_{Z2i}}{\partial t} = \frac{1}{2v_{A1}} \frac{\partial}{\partial t} (V_{\theta 1i}^2). \quad (4.46)$$

Since there are no perturbations for  $t \leq 0$  it follows from this equation that for  $t < L/v_{A1}$  there is only the initial wave, so

$$V_{Z2i} = \frac{1}{2v_{A1}} V_{\theta 1i}^2 (t - z/v_{A2}). \quad (4.47)$$

In the region above the transitional layer, there is only transmitted wave, as defined in Eq. (4.10). So, again using Eqs. (4.8), (4.26), and (4.45) but considering the region  $z > L + \ell$ , we have

$$\frac{\partial V_{Z2t}}{\partial t} = \frac{1}{2v_{A2}} \frac{\partial}{\partial t} (V_{\theta 1t}^2). \quad (4.48)$$

Since there are no perturbations for  $t \leq 0$ , we obtain from Eq. (4.48) using Eq. (4.44)

$$\begin{aligned} V_{Z2t} &= \frac{2v_{A2}}{(v_{A1} + v_{A2})^2} \left[ V_{\theta 1i}(\Theta) - \frac{\chi H V'_{\theta 1i}(\Theta)}{v_{A1} + v_{A2}} + \frac{\chi \ell H V''_{\theta 1i}(\Theta)}{(v_{A1} + v_{A2})^2} \right]^2 \\ &\approx \frac{2v_{A2}}{(v_{A1} + v_{A2})^2} \left\{ V_{\theta 1i}^2(\Theta) - \frac{2\chi H}{v_{A1} + v_{A2}} V_{\theta 1i}(\Theta) V'_{\theta 1i}(\Theta) \right. \\ &\quad \left. + \frac{\chi H}{(v_{A1} + v_{A2})^2} [\chi H (V'_{\theta 1i}(\Theta))^2 + 2\ell V_{\theta 1i}(\Theta) V''_{\theta 1i}(\Theta)] \right\}. \quad (4.49) \end{aligned}$$

Here,  $\Theta = t - T - z/v_{A2}$ .

## 4.5 Mass flux ratio

Now, we calculate the total mass flux through the tube cross-section below and above the transitional layer. We assume that the function  $F(t, r)$  is factorised and can be written as  $F(t, r) = \Phi(t)\Psi(r)$ . It is convenient to calculate the incoming mass flux at  $z = 0$ , which is then given by

$$M_i = 2\pi\rho_1 \int_0^{r_0} r \int_0^\tau V_{Z2i}(t) dt dr, \quad (4.50)$$

where  $r_0$  is the tube radius. Using Eqs. (4.6) and (4.47), we transform this expression to

$$M_i = \frac{\pi \epsilon^2 \rho_1 v_{A1}}{B_0^2} \int_0^{r_0} \Psi^2(r) r dr \int_0^\tau \Phi^2(t) dt. \quad (4.51)$$

The total mass flux through any tube cross-section above the transitional layer is the same at any  $z > L + \ell$ . It follows from Eq. (4.49) that  $V_{Z2t}$  is different from zero only for  $0 < \Theta < \tau$ , that is for  $T + z/v_{A2} < t < \tau + T + z/v_{A2}$ . Hence

$$M_t = 2\pi \rho_2 \int_0^{r_0} r \int_{T+z/v_{A2}}^{\tau+T+z/v_{A2}} V_{Z2t}(t) dt dr. \quad (4.52)$$

Although  $z$  is present in this expression, the result will be the same for any  $z > L + \ell$ . Using Eq. (4.49) and the integration variable substitution we obtain

$$\begin{aligned} I &\equiv \int_{T+z/v_{A2}}^{\tau+T+z/v_{A2}} V_{Z2t}(t) dt \\ &= \frac{2v_{A2}}{(v_{A1} + v_{A2})^2} \int_0^\tau \left\{ V_{\theta 1i}^2(\Theta) - \frac{2\chi H}{v_{A1} + v_{A2}} V_{\theta 1i}(\Theta) V'_{\theta 1i}(\Theta) \right. \\ &\quad \left. + \frac{\chi H}{(v_{A1} + v_{A2})^2} [\chi H (V'_{\theta 1i}(\Theta))^2 + 2\ell V_{\theta 1i}(\Theta) V''_{\theta 1i}(\Theta)] \right\} d\Theta. \end{aligned} \quad (4.53)$$

Using integration by parts and Eq. (4.40), we transform this expression to

$$\begin{aligned} I &= \frac{2v_{A2}}{(v_{A1} + v_{A2})^2} \int_0^\tau \left( V_{\theta 1i}^2(\Theta) \right. \\ &\quad \left. + \left[ H^2 \left( \frac{1}{v_{A1}} - \frac{1}{v_{A2}} \right)^2 - \frac{\ell^2}{(v_{A1} + v_{A2})^2} \right] (V'_{\theta 1i}(\Theta))^2 \right) d\Theta. \end{aligned} \quad (4.54)$$

Substituting this expression in Eq. (4.52) and using Eq. (4.6) yields

$$\begin{aligned} M_t &= \frac{4\epsilon^2 \pi \rho_2 v_{A2} v_{A1}^2}{B_0^2 (v_{A1} + v_{A2})^2} \int_0^{r_0} \Psi^2(r) r dr \left( \int_0^\tau \Phi^2(t) dt \right. \\ &\quad \left. + \left[ H^2 \left( \frac{1}{v_{A1}} - \frac{1}{v_{A2}} \right)^2 - \frac{\ell^2}{(v_{A1} + v_{A2})^2} \right] \int_0^\tau (\Phi'(t))^2 dt \right), \end{aligned} \quad (4.55)$$

where we changed the integration variable from  $\Theta$  to  $t$ . Note that  $H$  is proportional to  $\ell$  such that  $\ell/H = 2\ln(\alpha)$  is fixed when  $v_{A1}$  and  $v_{A2}$  are given, where  $\alpha = v_{A2}/v_{A1}$ . Thus we see that the term proportional to the thickness of the transitional layer squared ( $\ell^2$ , equivalently  $H^2$ ) in the square brackets in Eq. (4.55) gives the correction to  $M_t$  related to the substitution of the discontinuity by the smooth transitional layer, and since  $\alpha > 1$  it follows that this correction is always positive. We recover the total mass flux due to the transmitted wave in the case of a discontinuity by taking  $\ell = 0$  (equivalently  $H = 0$ ).

To give an example we take

$$\Phi(t) = A \left( 1 - \cos \frac{2\pi t}{\tau} \right), \quad 0 < t < \tau, \quad (4.56)$$

where  $A$  is a constant and  $\Phi(t)$  is otherwise zero. This represents the driver of the wave, which is active for a finite duration  $\tau$ , creating a wave pulse. Then we obtain

$$\int_0^\tau (\Phi(t))^2 dt = \frac{3\tau A^2}{2}, \quad \int_0^\tau (\Phi'(t))^2 dt = \frac{2\pi^2 A^2}{\tau}. \quad (4.57)$$

Using these results and considering Eq. (4.55), we find that the ratio of the second term (with the square brackets) to the first term of that equation is

$$\begin{aligned} \lambda &= \frac{4\pi^2}{3\tau^2} \left[ H^2 \left( \frac{1}{v_{A1}} - \frac{1}{v_{A2}} \right)^2 - \frac{\ell^2}{(v_{A1} + v_{A2})^2} \right] \\ &= \frac{4\pi^2}{3} \left( \frac{\ell}{v_{A1}\tau} \right)^2 \left[ \left( \frac{1 - \alpha}{2\alpha \ln(\alpha)} \right)^2 - \frac{1}{(1 + \alpha)^2} \right]. \end{aligned} \quad (4.58)$$

This ratio represents the proportion of the transmitted mass that is due to the effect of the transitional layer, compared to the case of the discontinuity. It is maximised at around  $\alpha = 5.082$ , when it is approximately equal to  $0.447(\ell/\tau v_{A1})^2 = 0.447\delta^2$ . Since we have  $\delta < 1$ , the additional transmitted mass due to the effect of the transitional layer must be much less than 44.7% of the total transmitted mass, for any feasible value of  $\alpha$ . If, in addition, we take  $\delta = 1/3$  as an example to satisfy the thin-layer requirement, then we obtain that the ratio of two terms is 0.0497. Hence, in this case the transmitted flux is greater by approximately 5% than in the case of discontinuity

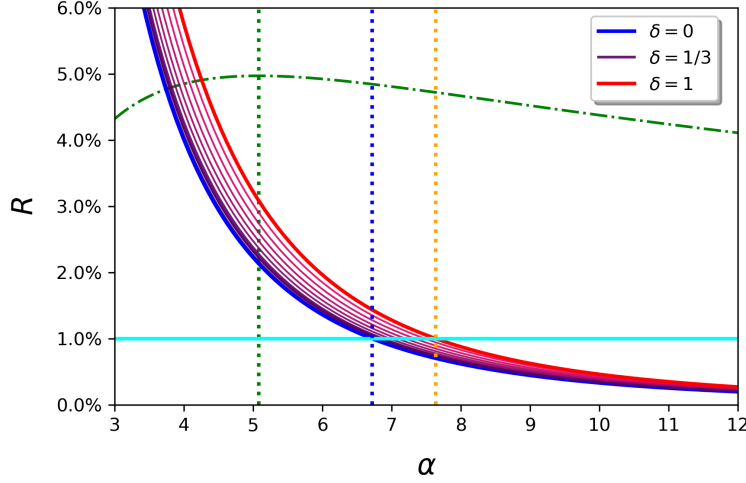


Figure 4.1: A plot of the mass flux ratio  $R$  against  $\alpha$ , showing the effect of varying  $\delta$  and thus the thickness of the transitional layer. Here, we consider multiple values of  $\delta$  in the range  $0 < \delta < 1$ . It should be noted that  $\delta = 1$  is included as an extreme case for the sake of comparison, but that the model requires a thin layer, i.e.  $\delta \ll 1$ . The one percent transmission threshold is shown as a cyan line which intersects with the  $\delta = 0$  curve of the ratio at  $\alpha = 6.717$  (blue dotted line), and with the  $\delta = 1$  curve of the ratio at  $\alpha = 7.638$  (orange dotted line). Also shown is the proportion of transmitted mass that is due to the effect of the transitional layer,  $\lambda$  (green dot-dashed curve) for  $\delta = 1/3$ , with the maximum indicated at  $\alpha = 5.082$  (green dotted line).

(illustrated in Fig. 4.1). This is encouraging because it suggests that the actual density-stratified solar atmosphere would most likely allow for some spicular material to pass through the chromosphere as a result of torsional Alfvén waves.

We can also find the ratio  $R$  of the relative mass flux, i.e. the ratio of the mass of plasma that moves due to the transmitted wave through a given surface  $z > L + \ell$  above the transitional layer, as a proportion of the plasma

that moves due to the initial wave through a surface  $z < L$ :

$$\begin{aligned}
 R &= \frac{M_t}{M_i} \\
 &= \frac{4}{\alpha(1+\alpha)^2} \left( 1 + \frac{4\pi^2}{3} \left( \frac{\ell}{v_{A1}\tau} \right)^2 \left[ \left( \frac{1-\alpha}{2\alpha \ln(\alpha)} \right)^2 - \frac{1}{(1+\alpha)^2} \right] \right). \quad (4.59)
 \end{aligned}$$

Notably, this is similar to the mass flux ratio found in Scalisi et al. (2021b) (see Chapter 3, Eq. (3.32)) but with an extra term proportional to  $\ell^2$ , hence it is clear that the inclusion of the transitional layer has had a quantifiable effect on the model. Since we defined  $\Psi(r)$  such that it does not depend on  $t$  or  $z$ , for the purpose of this example,  $R$  does not depend on  $\Psi$ . The ratio  $R$  is shown in Fig. 4.1. We now explore how the mass flux ratio changes due to the extra term introduced as a result of considering a transitional layer sandwiched between the chromosphere and the low corona, in the next section.

## 4.6 Discussion

The result from this model depends on how we specify  $v_{A1}$ ,  $\tau$ ,  $H$ , and  $\alpha$ , and specifying any one of these parameters may influence how we specify another. However, we are particularly interested in how the ratio changes depending on the thickness of the transitional layer  $\ell$  while the other variables remain constant (although we can consider various discrete cases). Therefore we will have different values for the scale height  $H = \ell/2 \ln(\alpha)$  when we vary  $\ell$ , while considering a particular value of  $\alpha$ . Since we will consider various cases, it may be helpful to explore physical constraints for the values of our parameters.

### 4.6.1 Alfvén speed and density

In strongly magnetic regions of the lower solar atmosphere inside a flux tube, the Alfvén speed would be on the order of  $10 \text{ km s}^{-1}$ , with some estimates suggesting values between  $7.7 \text{ km s}^{-1}$  (Roberts, 2019) and  $22 \text{ km s}^{-1}$  (Jess et al., 2009). Taking the latter value and using the definition of the Alfvén

speed in Eq. (4.4), this corresponds to an estimate for the density  $\rho_1$  in the lower layer of the model of around  $1.64 \times 10^{-8} \text{ g cm}^{-3}$ , with a kilogauss-strength background magnetic field. Higher in the atmosphere, the Alfvén speed increases by at least an order of magnitude (Vernazza et al., 1973), with estimates of  $1000 \text{ km s}^{-1}$  or more in the corona (Tomczyk et al., 2007; van Ballegoijen et al., 2011). However, our model is not intended to encompass the corona but rather the regions below it.

Values for the Alfvén speed of around  $556 \text{ km s}^{-1}$  are suggested by Okamoto and De Pontieu (2011) for the region corresponding to the extreme upper end of the range of spicule heights ( $15''$ , or around  $10.9 \text{ Mm}$ ). Using this value for the Alfvén speed in the upper layer, the corresponding density  $\rho_2$  can be estimated at around  $2.57 \times 10^{-11} \text{ g cm}^{-3}$ , again with a kilogauss-strength background magnetic field for the purposes of this model. Comparing the  $556 \text{ km s}^{-1}$  estimate and the  $22 \text{ km s}^{-1}$  estimate gives  $\alpha \approx 25$ . However, Okamoto and De Pontieu (2011) also suggest an Alfvén speed at the surface that is higher than previously mentioned estimates for the lower atmosphere, with their equivalent Alfvén speed ratio given as 3.39.

Informed by these sources, we will consider values for  $\alpha$  on the order of around 10, or equivalently a density ratio of around  $\rho_1/\rho_2 = 100$ . These estimates may be rather imprecise due to the highly variable nature of the solar atmosphere, especially in the vicinity of relatively small and dynamic features like spicules, hence the need to consider a range of values for these parameters. This range should give results that are compatible with the estimated ratio of the mass flux of the solar wind vs that of spicules (1%).

#### 4.6.2 Thickness of the transitional layer

The ratio  $R$  strictly increases proportional to  $\ell^2$ . This suggests that a wider transitional layer, in this case a more gentle gradient between the lower and upper regions in the model, results in stronger transmission of the wave. Note that if we take the limit as  $\ell \rightarrow 0$  then the ratio depends only on  $\alpha$ , hence this limit — equivalent to the case of the density discontinuity — gives the minimum value of the ratio for any particular value of  $\alpha$ . This minimum

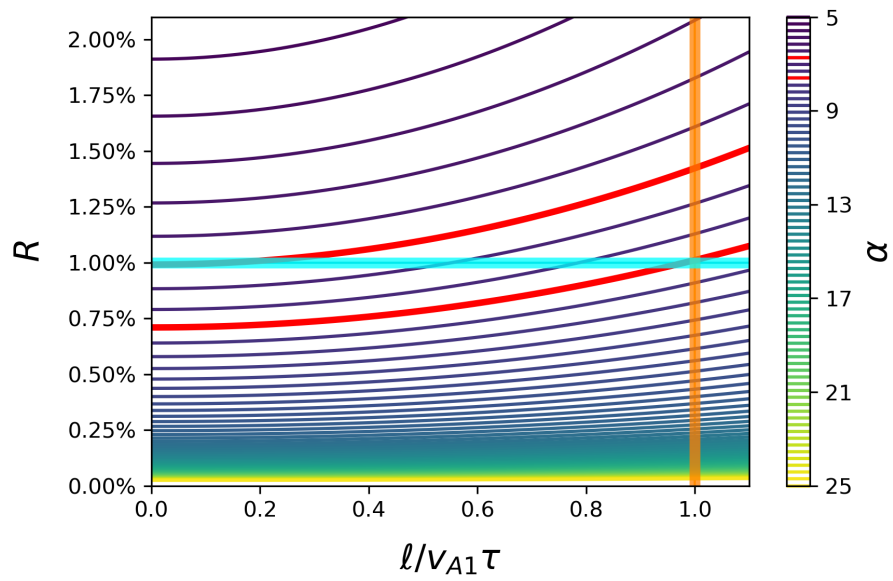


Figure 4.2: Plots of the mass flux ratio  $R$  against the thickness of the transitional layer  $\ell/v_{A1}\tau$  (scaled by the length of the pulse), illustrating the effect of varying  $\alpha$ . Here, we consider multiple values of  $\alpha$  in the range  $5 < \alpha < 25$ . The one percent transmission threshold is shown as a cyan line, and the line  $\ell = v_{A1}\tau$  as an orange line (note that  $\ell > v_{A1}\tau$  is beyond the scope of the model). Highlighted in red are the values of  $\alpha = 6.717$  and  $\alpha = 7.638$ .

ratio coincides with the result of Scalisi et al. (2021b); in particular, we find the minimum ratio matches the 1% estimate at  $\alpha \approx 6.717$ , just as in the example given in Chapter 3. In fact, for  $\alpha < 6.717$ , the one percent threshold is exceeded for all  $\ell$ . For  $\alpha > 7.638$ , the threshold is not reached for  $0 < \ell < v_{A1}\tau$ .

The minimum value of the ratio is on the order of  $\alpha^{-3}$  and so tends towards zero as  $\alpha \rightarrow \infty$ . Increasing the value of  $\alpha$  not only reduces this minimum value of  $R$  but also means that the ratio increases more slowly as  $\ell$  increases, as illustrated in Fig. 4.2. Hence we find that less of the mass would be transmitted above an arbitrarily thin transitional layer with a higher value of  $\alpha$ , and also that increasing the width of the transitional layer has less effect with a higher value of  $\alpha$  than it would with a lower value. This is, again, because the gradient in the transitional layer is more severe if there is a greater difference between the plasma density in the lower and upper regions.

### 4.6.3 Length of the pulse

Note that we assumed earlier in our calculations (see Section 4.3.2) that the transitional layer was thin compared to the length of the pulse. An effect of this stipulation is that the travel time for the pulse to cross the transitional layer is negligible. As a result, we should focus on the results for the range  $\ell < v_{A1}\tau$  to avoid loss of accuracy of the model. We are able to specify how the pulse is driven via the boundary conditions; in Scalisi et al. (2021a) we suggested that a pulse driven for around 150s could reach a maximum vertical extent matching the height of spicules, and this is within the range of the average period of torsional Alfvén waves in MBPs (where our hypothetical wave driver is located) given by Jess et al. (2023). So for example if  $\tau = 150$  s, along with an estimate of  $v_{A1} = 10 \text{ km s}^{-1}$ , we could consider  $\ell < 1500$  km. However, this may not be considered “thin” in comparison to the height of the chromosphere.

We may want to consider shorter pulses — these would still propagate at the Alfvén speed, reaching the height of observed spicules within a few minutes,

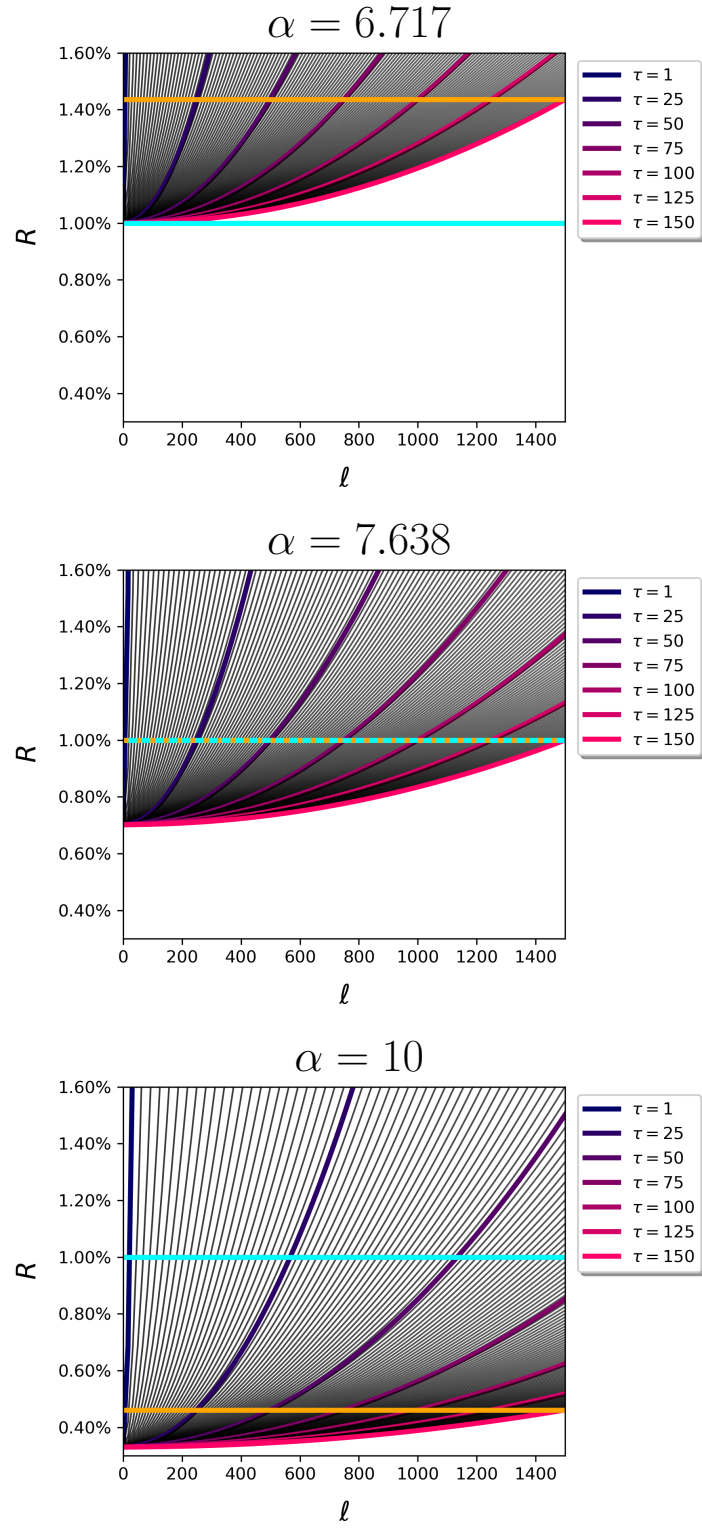


Figure 4.3: (Caption next page.)

Figure 4.3: (Previous page.) Plots of the mass flux ratio  $R$  against the thickness of the transitional layer  $\ell$  (in meters), illustrating the effect of varying pulse duration. Each curve represents a pulse with a different discrete value of the pulse duration (in seconds)  $\tau$  between  $\tau_{\min} = 1\text{s}$  and  $\tau_{\max} = 150\text{s}$ , all with constant  $v_{A1} = 10$ . Here,  $\ell$  is only shown between 0 and the maximum length of any of the pulses within the chosen range, i.e.  $v_{A1}\tau_{\max} = 1500\text{m}$ . Each curve intersects the orange line at its distinct value of  $v_{A1}\tau$  so, according to our assumptions about the thickness of the transitional layer, the range of  $\ell$  that the model encompasses for each curve is represented below and to the left of that intersection. The cyan line represents the one percent transmission threshold  $R = 0.01$ . We consider different values of  $\alpha$ : (a)  $\alpha = 6.717$ ; (b)  $\alpha = 7.638$ ; (c)  $\alpha = 10$ .

but would themselves be shorter in length than spicules. It is unclear whether the pulse needs to be driven continuously during the spicule’s ‘rising’ phase. If the driver is, for example, related to a photospheric or chromospheric swirl (Liu et al., 2019c,a) then it is likely that the duration would be shorter than the lifespan of a spicule since these features are observed to have average lifetimes of under 30s - although this is only slightly less than the lifespan of certain kinds of jets such as Type II spicules or RBEs (Kuridze et al., 2015). Again, it is useful to consider a range of possible values.

For a particular value of  $\alpha$ , if the pulse duration  $\tau$  is reduced then the mass flux ratio increases faster as  $\ell$  increases, i.e. a thinner transitional layer is required to reach the same ratio of transmitted mass. Regardless of the pulse duration we find the same value of the ratio for a given  $\alpha$  is always reached at  $\ell = v_{A1}\tau$ , the upper limit of the range of  $\ell$  that we consider valid for this model. This maximum value of the ratio varies with  $\alpha$  in a similar way to the minimum value (at  $\ell = 0$ ), i.e. on the order of  $\alpha^{-3}$ , and reaches 1% at  $\alpha \approx 7.638$ .

The effect of varying  $\tau$  is illustrated in Figure 4.3, for three discrete values of  $\alpha$  representing different cases. In case (a), for  $\alpha = 6.717$ , the one percent transmission threshold (cyan line) is met at  $\ell = 0$  regardless of the pulse

duration, and at  $\ell = v_{A1}\tau$  (orange line), the ratio is always just under 1.5%. In case (b), for  $\alpha = 7.638$ , the one percent threshold is always met at  $\ell = v_{A1}\tau$  regardless of the pulse duration (cyan and orange lines are superimposed at the same value of  $R = 0.01$ ). In case (c), we consider  $\alpha > 7.638$ , taking  $\alpha = 10$  as an example; here the ratio at  $\ell = v_{A1}\tau$  is less than 0.5% regardless of the pulse duration, hence the mass flux present above the transitional layer in the higher solar atmosphere would be even less than one percent of the initial flux (for all values of  $\ell < v_{A1}\tau$  satisfying our assumptions). This is acceptable in a physical context, since the one percent threshold refers to the total mass flux of spicules versus that of the solar wind, and spicules are of course not the only potential source of the solar wind. Therefore, one percent could be considered as the upper limit for the proportion of spicule material that may contribute to the solar wind. It follows that (c) is likely to be the most realistic of the three given cases. This is in line with the estimated values of the Alfvén speeds discussed earlier in this section.

#### 4.6.4 Limitations

There are some caveats concerning the physical interpretation of the results. For example, although the model is not intended to include the corona, in reality the transitional layer does not end at a region of constant plasma density and the Alfvén speed may continue to increase with height above the photosphere. Therefore it is likely that even less mass flux from the perturbations we describe will be present higher up in the atmosphere, and in the solar wind. However it is true that the greatest change in density by far in the solar atmosphere occurs over a small length scale in the transition region, such that the corona can be modelled with constant Alfvén speed for the purposes of this work.

In addition, it is difficult to predict with this model what will happen to the plasma that has already been lifted. It is possible that a spicule's later trajectory would be influenced by both gravity and the effect of waves being repeatedly reflected, since many jets' trajectories are not purely ballistic (De Pontieu et al., 2007a; Loboda and Bogachev, 2017) and the plasma is likely to be affected by the waves in a different way at the top of the spicule compared

to the at the base (Okamoto and De Pontieu, 2011). The model could be improved if we could account for this complex plasma behaviour.

## CHAPTER 5

---

### Conclusions and future work

---

In this final chapter, the conclusions of the combined research are reviewed and presented, including that of the published papers and other work presented in this thesis. The results and their significance are discussed, and the progression of the research as a whole is explained. Finally, I will suggest the next steps for any further research that myself or others may decide to conduct into this area of study.

#### **5.1 Conclusions**

The model presented in this thesis was developed with the intention of using analytical methods to study the mechanisms that generate solar jets. We aimed to explore how spicules may be affected by torsional waves that originate in photospheric magnetic bright points and propagate through the chromosphere. In addition, we made considerable efforts to determine the effect that these features may have on the outer solar atmosphere and estimate their potential to influence the solar wind.

Our initial investigation involved determining a suitable method to model solar jets analytically. In Chapter 2, we introduced the cylindrical flux tube and utilised a perturbation method, allowing us to begin to add complexity

to the model and examine the nature of vertically propagating waves and their effect on the motion of the plasma in the context of spicules. After consideration of the general case of the model in Section 2.3, we adapted the model to the physical conditions of the plasma specific to the environment that we intended to study, resulting in our employment of the zero-beta approximation.

The results of Scalisi et al. (2021a) presented in Chapter 2 suggest that a torsional perturbation in the lower solar atmosphere can cause vertical excitation of plasma by the Lorentz force, which is comparable to the motion of solar jets. A torsional Alfvén pulse propagating at speed of  $10\text{--}20\text{ km s}^{-1}$  is able to generate mass flux on the scale of a spicule, reaching heights of several megameters within the span of a few minutes. The consistency of the model with observed properties of spicules served as proof of concept and motivated the further development of the model to include additional atmospheric effects.

In Scalisi et al. (2021b), presented in Chapter 3, we began to improve our characterisation of the higher solar atmosphere by way of the inclusion of a discontinuity in density at an upper boundary in the flux tube model. In this way, we introduced stratification of the atmosphere representing the physical variation that has been observed to occur in the upper chromosphere and transition region. Studying the propagation and subsequent partial reflection of a torsional Alfvén pulse in this environment allowed us to model the later evolution of a spicule. We utilised this model to estimate the the mass flux that may be present in the higher atmosphere due to the component of the wave that is transmitted through the discontinuity, as a proportion of the initial mass flux. The results suggest that there would be plasma flux present in the upper region on the order of 1% of the flux due to the initial pulse, in accordance with estimates.

With the three-layered system of Scalisi et al. (2023) explored in Chapter 4, we expanded the model to investigate whether mass flux would be generated due to a transmitted Alfvén wave in the solar atmosphere above a transitional layer, and to examine the differences between this and the discontinuity case. By introducing this additional complexity in the system we presented a more

authentic representation of the atmosphere than the discontinuity case. This also allowed us to confirm that our previous results are consistent with the more physically accurate model. We found good agreement when comparing the results with properties of spicules and the solar wind, and found that in comparison to the case of a discontinuity there is a slight increase of the mass flux in the upper region. This also allowed us to consider appropriate ranges for the parameters of the atmosphere described by the model.

The development of our model has suggested several things about spicules: primarily, that the generation of jet-like motion can be driven or influenced by magnetic perturbations in the form of torsional Alfvén waves originating in strongly magnetic photospheric regions. In addition, we found that these waves are restricted in the extent that they are able to propagate out into the atmosphere, putting a limit on the maximum height to which jets may be driven by them and suggesting that almost all of the mass lifted by this process will remain in the lower solar atmosphere rather than being ejected into the corona, as expected. However, despite that limit, we suggest that some material from the jets may be carried higher into the atmosphere by the transmitted portion of the waves that are present during the formation of the jets, although only a small amount of this may eventually contribute to the solar wind.

Overall the model is a useful diagnostic tool, making use of established analytical methods but applying them in a novel way to investigate the feasibility and compatibility of a proposed mechanism of solar jet generation. This research has enabled us to explore the processes occurring in the lower solar atmosphere, and has provided some insight into the scale of the influence that spicules can have on the solar atmosphere beyond the chromosphere.

## 5.2 Future work

Although the model we have developed here has given us some idea of the process behind jet formation and the potential role of torsional Alfvén waves in spicule evolution, it is clear that there are limitations in this analytical method due to the rapid increase in the complexity of the system as we ap-

proach more physically realistic conditions. The MHD system is nonlinear and so, therefore, is the problem of modelling solar jets — hence the popularity of numerical modelling and simulation when considering plasma and jet dynamics. It would be useful to undertake a more detailed comparison of our results with models that are based on these methods, or to build our own equivalent.

The analysis presented so far does not explicitly consider the variation of the background magnetic field with height, although — since the magnetic field strength is proportional to the Alfvén speed — it is indirectly taken into account by the current model and the effect of this variation can be inferred. However, tube expansion higher in the atmosphere will occur with the decreasing magnetic field strength inside the flux tube and may affect our estimates. A more thorough analysis of this effect could be the subject of a future study, building on the framework of the model presented here.

Our investigations have allowed us to make estimates of physical parameters, so another useful endeavour would be to make observations to check that these estimates are in the correct range. In addition, we would like to explicitly observe the evolution of torsional Alfvén waves in the context of spicules. We would then be able to directly measure the effects of these waves on plasma flux and compare with our predictions. Finally, we would also expand the scope of the study to other solar jets such as coronal jets and macropicules. A long-term observational study over a full 11-year solar cycle may uncover new patterns in the behaviour of these jets.

# Appendices



## APPENDIX A

---

### Verification of continuity of $V_{Z2}$

---

To check the continuity of  $V_{Z2}$  we must also consider the region above the density discontinuity. Using Equations (3.11), (3.15), and (3.18), we find that for  $z > L$ ,

$$\frac{\partial V_{\theta 1}}{\partial t} = -\frac{2v_{A1}v_{A2}}{B_0(v_{A1} + v_{A2})} \frac{\partial}{\partial t} F(t - L/v_{A1} - (z - L)/v_{A2}), \quad (\text{A.1})$$

and so

$$\frac{\partial V_{Z2}}{\partial t} = -\frac{1}{B_0} B_{\theta 1} \frac{\partial V_{\theta 1}}{\partial t} \quad (\text{A.2})$$

$$= \frac{2v_{A1}^2 v_{A2}}{B_0^2 (v_{A1} + v_{A2})^2} \frac{\partial}{\partial t} (F^2(t - L/v_{A1} - (z - L)/v_{A2})). \quad (\text{A.3})$$

Therefore, we define for  $L/v_{A1} + (z - L)/v_{A2} < t < L/v_{A1} + (z - L)/v_{A2} + \tau$ ,

$$V_{Z2} = V_{Z2t} = \frac{2v_{A2}}{\mu_0 \rho_{01} (v_{A1} + v_{A2})^2} F^2(t - L/v_{A1} - (z - L)/v_{A2}), \quad z > L. \quad (\text{A.4})$$

Using our example pulse in Section 3.4, and evaluating at  $z = L$ , we obtain

$$V_{Z2t}(z = L) = \frac{2B_{\max}^2 v_{A2}}{\mu_0 \rho_{01} (v_{A1} + v_{A2})^2} \sin^2(\pi (r/R_0)^\sigma) \sin^2\left(\frac{\pi}{\tau}(t - L/v_{A1})\right). \quad (\text{A.5})$$

For  $0 < z < L$  we have  $V_{Z2} = V_{Z2i} + V_{Z2r} + V_{Z2n}$ , where  $V_{Z2i}$  is only non-zero for  $z/v_{A1} < t < z/v_{A1} + \tau$ ,  $V_{Z2r}$  is only non-zero for  $(2L - z)/v_{A1} < t < (2L - z)/v_{A1} + \tau$ , and  $V_{Z2n}$  is defined as in Eq. (3.45).

For  $t < z/v_{A1}$ ,  $V_{Z2i} = V_{Z2r} = V_{Z2n} = 0$  by definition. At  $t = z/v_{A1}$ ,

$$V_{Z2i} = \frac{B_{\max}^2}{2\mu_0\rho_{01}v_{A1}} \sin^2(\pi(r/R_0)^\sigma) \sin^2\left(\frac{\pi}{\tau}(z/v_{A1} - z/v_{A1})\right) = 0. \quad (\text{A.6})$$

For  $t < (2L - z)/v_{A1}$ ,  $V_{Z2r} = V_{Z2n} = 0$  by definition so  $V_{Z2} = V_{Z2i}$ . At  $t = (2L - z)/v_{A1}$ ,

$$V_{Z2i} = \frac{B_{\max}^2}{2\mu_0\rho_{01}v_{A1}} \sin^2(\pi(r/R_0)^\sigma) \sin^2\left(\frac{2\pi}{\tau}\left(\frac{L - z}{v_{A1}}\right)\right), \quad (\text{A.7})$$

$$V_{Z2r} = -\frac{B_{\max}^2}{2\mu_0\rho_{01}v_{A1}} \left(\frac{v_{A1} - v_{A2}}{v_{A1} + v_{A2}}\right)^2 \times \sin^2(\pi(r/R_0)^\sigma) \sin^2\left(\frac{\pi}{\tau}\left(\frac{2L - z}{v_{A1}} + \frac{z - 2L}{v_{A1}}\right)\right) \equiv 0, \quad (\text{A.8})$$

$$V_{Z2n} = G^*(r) \sin\left(\frac{2\pi(L - z)}{v_{A1}\tau}\right) \left(\frac{2L - z}{v_{A1}} - \frac{2L - z}{v_{A1}}\right) \equiv 0, \quad (\text{A.9})$$

and note that here  $V_{Z2i}$  is equal to zero at  $z = L$ .

For  $(2L - z)/v_{A1} < t < z/v_{A1} + \tau$ , all three wave components may be non-zero below the discontinuity and we also have the transmitted wave  $V_{Z2t}$ . Therefore for  $z < L$ ,

$$\begin{aligned} V_{Z2} &= V_{Z2i} + V_{Z2r} + V_{Z2n} \\ &= \frac{B_{\max}^2}{2\mu_0\rho_{01}v_{A1}} \sin^2(\pi(r/R_0)^\sigma) \left[ \sin^2\left(\frac{\pi}{\tau}(t - z/v_{A1})\right) \right. \\ &\quad \left. - \left(\frac{v_{A1} - v_{A2}}{v_{A1} + v_{A2}}\right)^2 \sin^2\left(\frac{\pi}{\tau}\left(t + \frac{z - 2L}{v_{A1}}\right)\right) \right] \\ &\quad + G^*(r) \sin\left(\frac{2\pi(L - z)}{v_{A1}\tau}\right) \left(t - \frac{2L - z}{v_{A1}}\right). \end{aligned} \quad (\text{A.10})$$

At  $z = L$  we find

$$V_{Z2} = \frac{2B_{\max}^2 v_{A2}}{\mu_0\rho_{01}(v_{A1} + v_{A2})^2} \sin^2(\pi(r/R_0)^\sigma) \sin^2\left(\frac{\pi}{\tau}(t - L/v_{A1})\right), \quad (\text{A.11})$$

which matches the transmitted wave at  $z = L$  as in (A.5).

Finally, for  $t > z/v_{A1} + \tau$ , we have defined  $V_{Z2i} = 0$  so  $V_{Z2} = V_{Z2r} + V_{Z2n}$  for  $z < L$ . At  $t = z/v_{A1} + \tau$ , we have

$$V_{Z2i} = \frac{B_{\max}^2}{2\mu_0\rho_{01}v_{A1}} \sin^2(\pi(r/R_0)^\sigma) \sin^2\left(\frac{\pi}{\tau}\left(\frac{z}{v_{A1}} + \tau - \frac{z}{v_{A1}}\right)\right) \equiv 0, \quad (\text{A.12})$$

$$V_{Z2r} = -\frac{B_{\max}^2}{2\mu_0\rho_{01}v_{A1}} \left(\frac{v_{A1} - v_{A2}}{v_{A1} + v_{A2}}\right)^2 \times \sin^2(\pi(r/R_0)^\sigma) \sin^2\left(\frac{\pi}{\tau}\left(\frac{2z - 2L}{v_{A1}} + \tau\right)\right), \quad (\text{A.13})$$

$$V_{Z2n} = G^*(r) \sin\left(\frac{2\pi(L - z)}{v_{A1}\tau}\right) \left(\tau + \frac{2z - 2L}{v_{A1}}\right), \quad (\text{A.14})$$

and note that here  $V_{Z2r} = V_{Z2n} = 0$  at  $z = L$ .



---

## References

---

- Mark J. Ablowitz and Athanassios S. Fokas. Complex Variables: Introduction and Applications. Cambridge Texts in Applied Mathematics. Cambridge University Press, 2 edition, 2003. doi: 10.1017/CBO9780511791246.
- M. Abramowitz and I. A. Stegun. Handbook of Mathematical Functions. U.S. Government Printing Office, National Bureau of Standards, 1964.
- L. Adhikari, G. P. Zank, and L. L. Zhao. Does Turbulence Turn off at the Alfvén Critical Surface? Astrophysical Journal, 876(1):26, May 2019. doi: 10.3847/1538-4357/ab141c.
- H. Alfvén. On the Existence of Electromagnetic-Hydrodynamic Waves. Arkiv for Matematik, Astronomi och Fysik, 29B:1–7, January 1943.
- C. E. Alissandrakis. Where is the base of the Transition Region? Evidence from TRACE, SDO, IRIS and ALMA observations. arXiv e-prints, art. arXiv:2207.03159, July 2022.
- Matthew Mark Allcock. Asymmetric Magnetohydrodynamic Waves of the Solar Atmosphere. PhD thesis, University of Sheffield, September 2020. URL <https://etheses.whiterose.ac.uk/28737/>.
- P. Antolin and K. Shibata. The Role Of Torsional Alfvén Waves in Coronal Heating. Astrophysical Journal, 712(1):494–510, March 2010. doi: 10.1088/0004-637X/712/1/494.

- Markus J. Aschwanden. Physics of the Solar Corona. An Introduction with Problems and Solutions. Springer Berlin, Heidelberg, 2005.
- R. G. Athay and T. E. Holzer. The role of spicules in heating the solar atmosphere. Astrophysical Journal, 255:743–752, April 1982. doi: 10.1086/159873.
- T. Ayres, H. Uitenbroek, G. Cauzzi, K. Reardon, T. Berger, C. Schrijver, B. de Pontieu, P. Judge, S. McIntosh, S. White, and S. Solanki. The Solar Chromosphere: Old Challenges, New Frontiers. In astro2010: The Astronomy and Astrophysics Decadal Survey, volume 2010, page 9, January 2009.
- W. Bate, D. B. Jess, V. M. Nakariakov, S. D. T. Grant, S. Jafarzadeh, M. Stangalini, P. H. Keys, D. J. Christian, and F. P. Keenan. High-frequency Waves in Chromospheric Spicules. Astrophysical Journal, 930(2):129, May 2022. doi: 10.3847/1538-4357/ac5c53.
- Andrea Francesco Battaglia, José Roberto Canivete Cuissa, Flavio Calvo, Aleksi Antoine Bossart, and Oskar Steiner. The Alfvénic nature of chromospheric swirls. Astronomy and Astrophysics, 649:A121, May 2021. doi: 10.1051/0004-6361/202040110.
- J. M. Beckers. Solar Spicules (Invited Review Paper). SoPh, 3(3):367–433, March 1968. doi: 10.1007/BF00171614.
- T. E. Berger, C. J. Schrijver, R. A. Shine, T. D. Tarbell, A. M. Title, and G. Scharmer. New Observations of Subarcsecond Photospheric Bright Points. Astrophysical Journal, 454:531, November 1995. doi: 10.1086/176504.
- T. E. Berger, L. Rouppe van der Voort, and M. Löfdahl. Contrast Analysis of Solar Faculae and Magnetic Bright Points. Astrophysical Journal, 661(2):1272–1288, June 2007. doi: 10.1086/517502.
- J. D. Bohlin, S. N. Vogel, J. D. Purcell, Jr. Sheeley, N. R., R. Tousey, and M. E. Vanhoosier. A newly observed solar feature: macrospicules in He

- II 304 Å. Astrophysical Journal, Letters, 197:L133–L135, May 1975. doi: 10.1086/181794.
- T. M. Brown and J. Christensen-Dalsgaard. Accurate determination of the solar photospheric radius. The Astrophysical Journal, 500(2):L195, jun 1998. doi: 10.1086/311416. URL <https://dx.doi.org/10.1086/311416>.
- Il-Hyun Cho, Yong-Jae Moon, Valery M. Nakariakov, Dae Jung Yu, Jin-Yi Lee, Su-Chan Bong, Rok-Soon Kim, Kyung-Suk Cho, Yeon-Han Kim, and Jae-Ok Lee. Seismological Determination of the Alfvén Speed and Plasma Beta in Solar Photospheric Bright Points. Astrophysical Journal, Letters, 871(1):L14, January 2019. doi: 10.3847/2041-8213/aafe0a.
- J. W. Cirtain, L. Golub, A. R. Winebarger, B. de Pontieu, K. Kobayashi, R. L. Moore, R. W. Walsh, K. E. Korreck, M. Weber, P. McCauley, A. Tittle, S. Kuzin, and C. E. Deforest. Energy release in the solar corona from spatially resolved magnetic braids. Nature, 493(7433):501–503, January 2013. doi: 10.1038/nature11772.
- A. Claverie, G. R. Isaak, C. P. McLeod, H. B. van der Raay, and T. Roca Cortes. Solar structure from global studies of the 5-minute oscillation. Nature, 282:591–594, December 1979. doi: 10.1038/282591a0.
- S. R. Cranmer and A. A. van Ballegoijen. On the Generation, Propagation, and Reflection of Alfvén Waves from the Solar Photosphere to the Distant Heliosphere. Astrophysical Journal, Supplement, 156(2):265–293, February 2005. doi: 10.1086/426507.
- P. J. Crockett, M. Mathioudakis, D. B. Jess, S. Shelyag, F. P. Keenan, and D. J. Christian. The Area Distribution of Solar Magnetic Bright Points. Astrophysical Journal, Letters, 722(2):L188–L193, October 2010. doi: 10.1088/2041-8205/722/2/L188.
- B. De Pontieu, V. H. Hansteen, L. Rouppe van der Voort, M. van Noort, and M. Carlsson. High-Resolution Observations and Modeling of Dynamic Fibrils. Astrophysical Journal, 655(1):624–641, January 2007a. doi: 10.1086/509070.

- B. De Pontieu, S. W. McIntosh, M. Carlsson, V. H. Hansteen, T. D. Tarbell, P. Boerner, J. Martinez-Sykora, C. J. Schrijver, and A. M. Title. The Origins of Hot Plasma in the Solar Corona. *Science*, 331(6013):55, January 2011. doi: 10.1126/science.1197738.
- B. De Pontieu, M. Carlsson, L. H. M. Rouppe van der Voort, R. J. Rutten, V. H. Hansteen, and H. Watanabe. Ubiquitous Torsional Motions in Type II Spicules. *Astrophysical Journal, Letters*, 752(1):L12, June 2012. doi: 10.1088/2041-8205/752/1/L12.
- B. De Pontieu, A. M. Title, J. R. Lemen, G. D. Kushner, D. J. Akin, B. Allard, T. Berger, P. Boerner, M. Cheung, C. Chou, J. F. Drake, D. W. Duncan, S. Freeland, G. F. Heyman, C. Hoffman, N. E. Hurlburt, R. W. Lindgren, D. Mathur, R. Rehse, D. Sabolish, R. Seguin, C. J. Schrijver, T. D. Tarbell, J. P. Wülser, C. J. Wolfson, C. Yanari, J. Mudge, N. Nguyen-Phuc, R. Timmons, R. van Bezooijen, I. Weingrod, R. Brookner, G. Butcher, B. Dougherty, J. Eder, V. Knagenhjelm, S. Larsen, D. Mansir, L. Phan, P. Boyle, P. N. Cheimets, E. E. DeLuca, L. Golub, R. Gates, E. Hertz, S. McKillop, S. Park, T. Perry, W. A. Podgorski, K. Reeves, S. Saar, P. Testa, H. Tian, M. Weber, C. Dunn, S. Eccles, S. A. Jaeggli, C. C. Kankelborg, K. Mashburn, N. Pust, L. Springer, R. Carvalho, L. Kleint, J. Marmie, E. Mazmanian, T. M. D. Pereira, S. Sawyer, J. Strong, S. P. Worden, M. Carlsson, V. H. Hansteen, J. Leenaarts, M. Wiesmann, J. Aloise, K. C. Chu, R. I. Bush, P. H. Scherrer, P. Brekke, J. Martinez-Sykora, B. W. Lites, S. W. McIntosh, H. Uitenbroek, T. J. Okamoto, M. A. Gummin, G. Auken, P. Jerram, P. Pool, and N. Waltham. The Interface Region Imaging Spectrograph (IRIS). *SoPh*, 289(7):2733–2779, July 2014. doi: 10.1007/s11207-014-0485-y.
- Bart De Pontieu, Robert Erdélyi, and Stewart P. James. Solar chromospheric spicules from the leakage of photospheric oscillations and flows. *Nature*, 430(6999):536–539, July 2004. doi: 10.1038/nature02749.
- Bart De Pontieu, Scott McIntosh, Viggo H. Hansteen, Mats Carlsson, Carolus J. Schrijver, Theodore D. Tarbell, Alan M. Title, Richard A. Shine, Yoshinori Suematsu, Saku Tsuneta, Yukio Katsukawa, Kiyoshi Ichimoto,

- Toshifumi Shimizu, and Shin'ichi Nagata. A Tale of Two Spicules: The Impact of Spicules on the Magnetic Chromosphere. PASJ, 59:S655, November 2007b. doi: 10.1093/pasj/59.sp3.S655.
- Alfred De Wijn, J. Stenflo, and Saku Tsuneta. Small-scale solar magnetic fields. Space Sci. Rev., 144, 01 2009. doi: 10.1007/s11214-008-9473-6.
- C. E. DeForest, T. A. Howard, and D. J. McComas. Inbound Waves in the Solar Corona: A Direct Indicator of Alfvén Surface Location. Astrophysical Journal, 787(2):124, June 2014. doi: 10.1088/0004-637X/787/2/124.
- R. J. Defouw. Wave propagation along a magnetic tube. Astrophysical Journal, 209:266–269, October 1976. doi: 10.1086/154717.
- Sahel Dey, Piyali Chatterjee, Murthy O. V. S. N., Marianna B. Korsós, Jiajia Liu, Christopher J. Nelson, and Robertus Erdélyi. Polymeric jets throw light on the origin and nature of the forest of solar spicules. Nature Physics, 18(5):595–600, March 2022. doi: 10.1038/s41567-022-01522-1.
- Fionnlagh Mackenzie Dover, Rahul Sharma, Marianna B. Korsós, and Robertus Erdélyi. Signatures of Cross-sectional Width Modulation in Solar Spicules due to Field-aligned Flows. Astrophysical Journal, 905(1):72, December 2020. doi: 10.3847/1538-4357/abc349.
- Yadan Duan, Yuandeng Shen, Hechao Chen, Zehao Tang, Chenrui Zhou, Xinpeng Zhou, and Song Tan. Macrospicules and Their Connection to Magnetic Reconnection in the Lower Solar Atmosphere. Astrophysical Journal, Letters, 942(1):L22, January 2023. doi: 10.3847/2041-8213/acac2b.
- Richard B. Dunn and Jack B. Zirker. The Solar Filigree. SoPh, 33(2):281–304, December 1973. doi: 10.1007/BF00152419.
- P. M. Edwin and B. Roberts. Wave Propagation in a Magnetically Structured Atmosphere - Part Three - the Slab in a Magnetic Environment. SoPh, 76(2):239–259, March 1982. doi: 10.1007/BF00170986.

- P. M. Edwin and B. Roberts. Wave Propagation in a Magnetic Cylinder. SoPh, 88(1-2):179–191, October 1983. doi: 10.1007/BF00196186.
- Walter M. Elsässer. Hydromagnetic Dynamo Theory. Reviews of Modern Physics, 28(2):135–163, April 1956. doi: 10.1103/RevModPhys.28.135.
- Robert Erdélyi. Chapter 5: Waves and Oscillations in the Solar Atmosphere. In B. N. Dwivedi and U. Narain, editors, Physics of the Sun and its Atmosphere, pages 61–108. 2008. doi: 10.1142/9789812832726\_0005.
- V. Fedun, S. Shelyag, G. Verth, M. Mathioudakis, and R. Erdélyi. Mhd waves generated by high-frequency photospheric vortex motions. Annales Geophysicae, 29(6):1029–1035, 2011. doi: 10.5194/angeo-29-1029-2011. URL <https://angeo.copernicus.org/articles/29/1029/2011/>.
- C. A. Ferraro and C. Plumpton. Hydromagnetic Waves in a Horizontally Stratified Atmosphere. V. Astrophysical Journal, 127:459, March 1958. doi: 10.1086/146474.
- A. J. Finley, A. S. Brun, M. Carlsson, M. Szydlarski, V. Hansteen, and M. Shoda. Stirring the base of the solar wind: On heat transfer and vortex formation. Astronomy and Astrophysics, 665:A118, September 2022. doi: 10.1051/0004-6361/202243947.
- E. Fossat, P. Boumier, T. Corbard, J. Provost, D. Salabert, F. X. Schmider, A. H. Gabriel, G. Grec, C. Renaud, J. M. Robillot, T. Roca-Cortés, S. Turck-Chièze, R. K. Ulrich, and M. Lazrek. Asymptotic g modes: Evidence for a rapid rotation of the solar core. Astronomy and Astrophysics, 604:A40, August 2017. doi: 10.1051/0004-6361/201730460.
- J. P. Hans Goedbloed and Stefaan Poedts. Principles of Magnetohydrodynamics. Cambridge University Press, 2004. doi: 10.1017/CBO9781139195560.
- J. J. González-Avilés, F. S. Guzmán, V. Fedun, G. Verth, S. Shelyag, and S. Regnier. I. Jet Formation and Evolution Due to 3D Magnetic Reconnection. Astrophysical Journal, 856(2):176, April 2018. doi: 10.3847/1538-4357/aab36f.

- Michael L. Goodman. Acceleration of Type II Spicules in the Solar Chromosphere. *Astrophysical Journal*, 757(2):188, October 2012. doi: 10.1088/0004-637X/757/2/188.
- Gerhard Haerendel. Weakly damped Alfvén waves as drivers of solar chromospheric spicules. *Nature*, 360(6401):241–243, November 1992. doi: 10.1038/360241a0.
- V. H. Hansteen, B. De Pontieu, L. Rouppe van der Voort, M. van Noort, and M. Carlsson. Dynamic Fibrils Are Driven by Magnetoacoustic Shocks. *Astrophysical Journal, Letters*, 647(1):L73–L76, August 2006. doi: 10.1086/507452.
- D. H. Hathaway, J. G. Beck, S. Han, and J. Raymond. Radial Flows in Supergranules. *SoPh*, 205(1):25–38, January 2002. doi: 10.1023/A:1013881213279.
- R. L. Hewitt, S. Shelyag, M. Mathioudakis, and F. P. Keenan. Plasma properties and Stokes profiles during the lifetime of a photospheric magnetic bright point. *Astronomy and Astrophysics*, 565:A84, May 2014. doi: 10.1051/0004-6361/201322882.
- J. Heyvaerts. Coronal Heating Mechanisms. In P. Murdin, editor, *Encyclopedia of Astronomy and Astrophysics*, page 2269. 2000. doi: 10.1888/0333750888/2269.
- E. J. Hinch. *Perturbation methods*. Cambridge University Press, 1991. doi: 10.1017/CBO9781139172189.
- J. V. Hollweg. Alfvén waves in the solar atmosphere. *SoPh*, 56(2):305–333, February 1978. doi: 10.1007/BF00152474.
- J. V. Hollweg. Alfvén Waves in the Solar Atmosphere - Part Two - Open and Closed Magnetic Flux Tubes. *SoPh*, 70(1):25–66, March 1981. doi: 10.1007/BF00154391.
- J. V. Hollweg. On the origin of solar spicules. *Astrophysical Journal*, 257:345–353, June 1982. doi: 10.1086/159993.

- J. V. Hollweg, S. Jackson, and D. Galloway. Alfvén Waves in the Solar Atmospheres - Part Three - Nonlinear Waves on Open Flux Tubes. SoPh, 75(1-2):35–61, January 1982. doi: 10.1007/BF00153458.
- Joseph V. Hollweg. Density fluctuations driven by Alfvén waves. J. Geophys. Res., 76(22):5155, January 1971. doi: 10.1029/JA076i022p05155.
- Joseph V. Hollweg. Alfvénically Driven Slow Shocks in the Solar Chromosphere and Corona. Astrophysical Journal, 389:731, April 1992. doi: 10.1086/171246.
- D. E. Innes, B. Inhester, W. I. Axford, and K. Wilhelm. Bi-directional plasma jets produced by magnetic reconnection on the Sun. Nature, 386(6627):811–813, April 1997. doi: 10.1038/386811a0.
- S. P. James and R. Erdélyi. Spicule formation by ion-neutral damping. Astronomy and Astrophysics, 393:L11–L14, October 2002. doi: 10.1051/0004-6361:20021126.
- S. P. James, R. Erdélyi, and B. De Pontieu. Can ion-neutral damping help to form spicules? Astronomy and Astrophysics, 406:715–724, August 2003. doi: 10.1051/0004-6361:20030685.
- D. B. Jess, D. J. Pascoe, D. J. Christian, M. Mathioudakis, P. H. Keys, and F. P. Keenan. The Origin of Type I Spicule Oscillations. Astrophysical Journal, Letters, 744(1):L5, January 2012a. doi: 10.1088/2041-8205/744/1/L5.
- D. B. Jess, S. Shelyag, M. Mathioudakis, P. H. Keys, D. J. Christian, and F. P. Keenan. Propagating Wave Phenomena Detected in Observations and Simulations of the Lower Solar Atmosphere. Astrophysical Journal, 746(2):183, February 2012b. doi: 10.1088/0004-637X/746/2/183.
- D. B. Jess, R. J. Morton, G. Verth, V. Fedun, S. D. T. Grant, and I. Gligkiozis. Multiwavelength Studies of MHD Waves in the Solar Chromosphere. An Overview of Recent Results. SSRv, 190(1-4):103–161, July 2015. doi: 10.1007/s11214-015-0141-3.

- David B. Jess, Mihalis Mathioudakis, Robert Erdélyi, Philip J. Crockett, Francis P. Keenan, and Damian J. Christian. Alfvén Waves in the Lower Solar Atmosphere. *Science*, 323(5921):1582, March 2009. doi: 10.1126/science.1168680.
- David B. Jess, Shahin Jafarzadeh, Peter H. Keys, Marco Stangalini, Gary Verth, and Samuel D. T. Grant. Waves in the lower solar atmosphere: the dawn of next-generation solar telescopes. *Living Reviews in Solar Physics*, 20(1):1, December 2023. doi: 10.1007/s41116-022-00035-6.
- P. H. Keys, M. Mathioudakis, D. B. Jess, S. Shelyag, P. J. Crockett, D. J. Christian, and F. P. Keenan. The Velocity Distribution of Solar Photospheric Magnetic Bright Points. *Astrophysical Journal, Letters*, 740(2):L40, October 2011. doi: 10.1088/2041-8205/740/2/L40.
- P. H. Keys, M. Mathioudakis, D. B. Jess, S. Shelyag, D. J. Christian, and F. P. Keenan. Tracking magnetic bright point motions through the solar atmosphere. *MNRAS*, 428(4):3220–3226, February 2013. doi: 10.1093/mnras/sts268.
- Peter Keys. *The dynamic properties of magnetic bright points*. PhD thesis, Queens University Belfast, Ireland, January 2013.
- Peter H. Keys, Aaron Reid, Mihalis Mathioudakis, Sergiy Shelyag, Vasco M. J. Henriques, Rebecca L. Hewitt, Dario Del Moro, Shahin Jafarzadeh, David B. Jess, and Marco Stangalini. The magnetic properties of photospheric magnetic bright points with high-resolution spectropolarimetry. *MNRAS*, 488(1):L53–L58, September 2019. doi: 10.1093/mnras/slz097.
- T. S. Kiss, N. Gyenge, and R. Erdélyi. Systematic Variations of Macrospicule Properties Observed by SDO/AIA over Half a Decade. *Astrophysical Journal*, 835(1):47, January 2017. doi: 10.3847/1538-4357/aa5272.
- Tamas Sandor Kiss. *Chromospheric Macrospicules: Connection to the Solar Dynamo?* PhD thesis, University of Sheffield, 2019. URL <https://etheses.whiterose.ac.uk/25342/>.

- I. N. Kitiashvili, A. G. Kosovichev, N. N. Mansour, and A. A. Wray. Dynamics of magnetized vortex tubes in the solar chromosphere. The Astrophysical Journal Letters, 751(1):L21, may 2012. doi: 10.1088/2041-8205/751/1/L21. URL <https://dx.doi.org/10.1088/2041-8205/751/1/L21>.
- P. Kohutova, E. Verwichte, and C. Froment. First direct observation of a torsional Alfvén oscillation at coronal heights. Astronomy and Astrophysics, 633:L6, January 2020. doi: 10.1051/0004-6361/201937144.
- Takahiro Kudoh and Kazunari Shibata. Alfvén Wave Model of Spicules and Coronal Heating. Astrophysical Journal, 514(1):493–505, March 1999. doi: 10.1086/306930.
- D. Kuridze, R. J. Morton, R. Erdélyi, G. D. Dorrian, M. Mathioudakis, D. B. Jess, and F. P. Keenan. Transverse Oscillations in Chromospheric Mottles. Astrophysical Journal, 750(1):51, May 2012. doi: 10.1088/0004-637X/750/1/51.
- D. Kuridze, V. Henriques, M. Mathioudakis, R. Erdélyi, T. V. Zaqarashvili, S. Shelyag, P. H. Keys, and F. P. Keenan. The Dynamics of Rapid Redshifted and Blueshifted Excursions in the Solar  $H\alpha$  Line. Astrophysical Journal, 802(1):26, March 2015. doi: 10.1088/0004-637X/802/1/26.
- Kenneth R. Lang. The Cambridge Encyclopedia of the Sun. 2001.
- Robert B. Leighton, Robert W. Noyes, and George W. Simon. Velocity Fields in the Solar Atmosphere. I. Preliminary Report. Astrophysical Journal, 135:474, March 1962. doi: 10.1086/147285.
- Jiajia Liu, Mats Carlsson, Chris J. Nelson, and Robert Erdélyi. Co-spatial velocity and magnetic swirls in the simulated solar photosphere. Astronomy and Astrophysics, 632:A97, December 2019a. doi: 10.1051/0004-6361/201936882.
- Jiajia Liu, Chris J. Nelson, and Robertus Erdélyi. Automated Swirl Detection Algorithm (ASDA) and Its Application to Simulation and Observational

- Data. *Astrophysical Journal*, 872(1):22, February 2019b. doi: 10.3847/1538-4357/aabd34.
- Jiajia Liu, Chris J. Nelson, Ben Snow, Yuming Wang, and Robert Erdélyi. Evidence of ubiquitous Alfvén pulses transporting energy from the photosphere to the upper chromosphere. *Nature Communications*, 10:3504, August 2019c. doi: 10.1038/s41467-019-11495-0.
- Yanxiao Liu, Yongyuan Xiang, Robertus Erdélyi, Zhong Liu, Dong Li, Zongjun Ning, Yi Bi, Ning Wu, and Jun Lin. Studies of Isolated and Non-isolated Photospheric Bright Points in an Active Region Observed by the New Vacuum Solar Telescope. *Astrophysical Journal*, 856(1):17, March 2018. doi: 10.3847/1538-4357/aab150.
- I. P. Loboda and S. A. Bogachev. Plasma dynamics in solar macrospicules from high-cadence extreme-UV observations. *Astronomy and Astrophysics*, 597:A78, January 2017. doi: 10.1051/0004-6361/201527559.
- Norbert Magyar, Dominik Utz, Robertus Erdélyi, and Valery M. Nakariakov. Could Switchbacks Originate in the Lower Solar Atmosphere? I. Formation Mechanisms of Switchbacks. *Astrophysical Journal*, 911(2):75, April 2021. doi: 10.3847/1538-4357/abec49.
- Mitsugu Makita. Chromospheric structure derived from flash spectra of the total solar eclipse. *Publications of the National Astronomical Observatory of Japan*, 7(1):1–24, March 2003.
- Eckart Marsch. Kinetic Physics of the Solar Corona and Solar Wind. *Living Reviews in Solar Physics*, 3(1):1, July 2006. doi: 10.12942/lrsp-2006-1.
- J. Martínez-Sykora, B. De Pontieu, V. H. Hansteen, L. Rouppe van der Voort, M. Carlsson, and T. M. D. Pereira. On the generation of solar spicules and Alfvénic waves. *Science*, 356(6344):1269–1272, June 2017. doi: 10.1126/science.aah5412.

- M. Mathioudakis, D. B. Jess, and R. Erdélyi. Alfvén Waves in the Solar Atmosphere. From Theory to Observations. *SSRv*, 175(1-4):1–27, June 2013. doi: 10.1007/s11214-012-9944-7.
- Takuma Matsumoto and Kazunari Shibata. Nonlinear Propagation of Alfvén Waves Driven by Observed Photospheric Motions: Application to the Coronal Heating and Spicule Formation. *Astrophysical Journal*, 710(2):1857–1867, February 2010. doi: 10.1088/0004-637X/710/2/1857.
- Scott W. McIntosh, Bart de Pontieu, Mats Carlsson, Viggo Hansteen, Paul Boerner, and Marcel Goossens. Alfvénic waves with sufficient energy to power the quiet solar corona and fast solar wind. *Nature*, 475(7357):477–480, July 2011. doi: 10.1038/nature10235.
- R. Mitalas and K. R. Sills. On the Photon Diffusion Time Scale for the Sun. *Astrophysical Journal*, 401:759, December 1992. doi: 10.1086/172103.
- R. J. Morton, G. Verth, A. Hillier, and R. Erdélyi. The Generation and Damping of Propagating MHD Kink Waves in the Solar Atmosphere. *Astrophysical Journal*, 784(1):29, March 2014. doi: 10.1088/0004-637X/784/1/29.
- Valery M. Nakariakov and Erwin Verwichte. Coronal Waves and Oscillations. *Living Reviews in Solar Physics*, 2(1):3, May 2005. doi: 10.12942/lrsp-2005-3.
- Takenori J. Okamoto and Bart De Pontieu. Propagating Waves Along Spicules. *Astrophysical Journal, Letters*, 736(2):L24, August 2011. doi: 10.1088/2041-8205/736/2/L24.
- William Oxley, Joseph Scalisi, Michael S. Ruderman, and Róbert Erdélyi. Formation of Chromospheric Spicules in Magnetic Bright Points: An Analytical Approach Using Cartesian Slab Geometry. *Astrophysical Journal*, 905(2):168, December 2020. doi: 10.3847/1538-4357/abcafe.
- E. N. Parker. Dynamics of the Interplanetary Gas and Magnetic Fields. *Astrophysical Journal*, 128:664, November 1958. doi: 10.1086/146579.

- Jay M. Pasachoff, William A. Jacobson, and Alphonse C. Sterling. Limb Spicules from the Ground and from Space. SoPh, 260(1):59–82, November 2009. doi: 10.1007/s11207-009-9430-x.
- T. M. D. Pereira, B. De Pontieu, M. Carlsson, V. Hansteen, T. D. Tarbell, J. Lemen, A. Title, P. Boerner, N. Hurlburt, J. P. Wülser, J. Martínez-Sykora, L. Kleint, L. Golub, S. McKillop, K. K. Reeves, S. Saar, P. Testa, H. Tian, S. Jaeggli, and C. Kankelborg. An Interface Region Imaging Spectrograph First View on Solar Spicules. Astrophysical Journal, Letters, 792(1):L15, September 2014. doi: 10.1088/2041-8205/792/1/L15.
- Tiago M. D. Pereira, Bart De Pontieu, and Mats Carlsson. Quantifying Spicules. Astrophysical Journal, 759(1):18, November 2012. doi: 10.1088/0004-637X/759/1/18.
- Tiago M. D. Pereira, Bart De Pontieu, and Mats Carlsson. The Effects of Spatio-temporal Resolution on Deduced Spicule Properties. Astrophysical Journal, 764(1):69, February 2013. doi: 10.1088/0004-637X/764/1/69.
- Eric Priest. Magnetohydrodynamics of the Sun. Cambridge University Press, 2014. doi: 10.1017/CBO9781139020732.
- H. A. Priestley. Introduction to complex analysis. Oxford University Press, Oxford, England, second edition. edition, 2005. ISBN 0-19-103720-6.
- R. Rankin, P. Frycz, V. T. Tikhonchuk, and J. C. Samson. Nonlinear standing shear Alfvén waves in the Earth’s magnetosphere. J. Geophys. Res., 99(A11):21291–21302, November 1994. doi: 10.1029/94JA01629.
- B. Roberts. Spicules: The resonant response to granular buffeting? SoPh, 61(1):23–34, February 1979. doi: 10.1007/BF00155443.
- B. Roberts. Wave Propagation in a Magnetically Structured Atmosphere - Part One - Surface Waves at a Magnetic Interface. SoPh, 69(1):27–38, January 1981a. doi: 10.1007/BF00151253.

- B. Roberts. Wave Propagation in a Magnetically Structured Atmosphere - Part Two - Waves in a Magnetic Slab. SoPh, 69(1):39–56, January 1981b. doi: 10.1007/BF00151254.
- B. Roberts and A. R. Webb. Vertical motions in an intense magnetic flux tube. SoPh, 56(1):5–35, January 1978. doi: 10.1007/BF00152630.
- B. Roberts and A. R. Webb. Vertical Motions in an Intense Magnetic Flux Tube - Part Three - on the Slender Flux Tube Approximation. SoPh, 64(1):77–92, November 1979. doi: 10.1007/BF00151117.
- Bernard Roberts. MHD waves in the solar atmosphere. Cambridge University Press, 2019.
- L. Rouppe van der Voort, J. Leenaarts, B. de Pontieu, M. Carlsson, and G. Vissers. On-disk Counterparts of Type II Spicules in the Ca II 854.2 nm and H $\alpha$  Lines. Astrophysical Journal, 705(1):272–284, November 2009. doi: 10.1088/0004-637X/705/1/272.
- M. S. Ruderman and M. Goossens. Nonlinear Kink Oscillations of Coronal Magnetic Loops. SoPh, 289:1999–2020, 2014. doi: 10.1007/s11207-013-0446-x.
- M. S. Ruderman, D. Berghmans, M. Goossens, and S. Poedts. Direct excitation of resonant torsional Alfvén waves by footpoint motions. Astronomy and Astrophysics, 320:305–318, April 1997.
- Margarita Ryutova. Physics of Magnetic Flux Tubes, volume 417. Springer-Verlag Berlin Heidelberg, 2015. ISBN 978-3-662-45242-4. doi: 10.1007/978-3-662-45243-1.
- Tanmoy Samanta, Hui Tian, Vasyl Yurchyshyn, Hardi Peter, Wenda Cao, Alphonse Sterling, Robertus Erdélyi, Kwangsu Ahn, Song Feng, Dominik Utz, Dipankar Banerjee, and Yajie Chen. Generation of solar spicules and subsequent atmospheric heating. Science, 366(6467):890–894, November 2019. doi: 10.1126/science.aaw2796.

- J. Sánchez Almeida, J. A. Bonet, B. Viticchié, and D. Del Moro. Magnetic Bright Points in the Quiet Sun. *Astrophysical Journal, Letters*, 715(1): L26–L29, May 2010. doi: 10.1088/2041-8205/715/1/L26.
- Joseph Scalisi, William Oxley, Michael S. Ruderman, and Robertus Erdélyi. Propagation of Torsional Alfvén Pulses in Zero-beta Flux Tubes. *Astrophysical Journal*, 911(1):39, April 2021a. doi: 10.3847/1538-4357/abe8db.
- Joseph Scalisi, Michael S. Ruderman, and Robertus Erdélyi. Reflection and Evolution of Torsional Alfvén Pulses in Zero-beta Flux Tubes. *Astrophysical Journal*, 922(2):118, December 2021b. doi: 10.3847/1538-4357/ac2509.
- Joseph Scalisi, Michael S. Ruderman, and Robertus Erdélyi. Generation of Vertical Flows by Torsional Alfvén Pulses in Zero-beta Tubes with a Transitional Layer. *Astrophysical Journal*, 951(1):60, 2023. doi: 10.3847/1538-4357/acd9ae. URL <https://iopscience.iop.org/article/10.3847/1538-4357/acd9ae>.
- Angelo Secchi. *L’astronomia in Roma nel pontificato DI Pio IX*. Tipografia della Pace, Roma, 1877.
- S. Shelyag, M. Mathioudakis, F. P. Keenan, and D. B. Jess. A photospheric bright point model. *Astronomy and Astrophysics*, 515:A107, June 2010. doi: 10.1051/0004-6361/200913846.
- Juie Shetye, Erwin Verwichte, Marco Stangalini, and J. G. Doyle. The Nature of High-frequency Oscillations Associated with Short-lived Spicule-type Events. *Astrophysical Journal*, 921(1):30, November 2021. doi: 10.3847/1538-4357/ac1a12.
- K. Shibata and Y. Uchida. A magnetodynamic mechanism for the formation of astrophysical jets. I - Dynamical effects of the relaxation of nonlinear magnetic twists. *PASJ*, 37(1):31–46, January 1985.

- K. Shibata and Y. Uchida. Sweeping Magnetic Twist Mechanism for the Acceleration of Jets in the Solar Atmosphere. *SoPh*, 103(2):299–310, February 1986. doi: 10.1007/BF00147831.
- Kazunari Shibata, Yoshinori Ishido, Loren W. Acton, Keith T. Strong, Tadashi Hirayama, Yutaka Uchida, Alan H. McAllister, Ryoji Matsumoto, Saku Tsuneta, Toshifumi Shimizu, Hirohisa Hara, Takashi Sakurai, Kiyoshi Ichimoto, Yohei Nishino, and Yoshiaki Ogawara. Observations of X-Ray Jets with the YOHKOH Soft X-Ray Telescope. *PASJ*, 44:L173–L179, October 1992.
- Michael D. Smith. *Astrophysical Jets and Beams*. Cambridge University Press, 2012. ISBN 9780511994562. doi: 10.1017/CBO9780511994562.
- Roberto Soler, Jaume Terradas, Ramón Oliver, and José Luis Ballester. Energy Transport and Heating by Torsional Alfvén Waves Propagating from the Photosphere to the Corona in the Quiet Sun. *Astrophysical Journal*, 871(1):3, January 2019. doi: 10.3847/1538-4357/aaf64c.
- H. C. Spruit. Equations for thin flux tubes in ideal MHD. *Astronomy and Astrophysics*, 102(1):129–133, September 1981.
- H. C. Spruit. Propagation Speeds and Acoustic Damping of Waves in Magnetic Flux Tubes. *SoPh*, 75(1-2):3–17, January 1982. doi: 10.1007/BF00153456.
- A. K. Srivastava, J. L. Ballester, P. S. Cally, M. Carlsson, M. Goossens, D. B. Jess, E. Khomenko, M. Mathioudakis, K. Murawski, and T. V. Zaqarashvili. Chromospheric Heating by Magnetohydrodynamic Waves and Instabilities. *Journal of Geophysical Research (Space Physics)*, 126(6):e029097, June 2021. doi: 10.1029/2020JA029097.
- Abhishek Kumar Srivastava, Juie Shetye, Krzysztof Murawski, John Gerard Doyle, Marco Stangalini, Eamon Scullion, Tom Ray, Dariusz Patryk Wójcik, and Bhola N. Dwivedi. High-frequency torsional Alfvén waves as an energy source for coronal heating. *Scientific Reports*, 7:43147, March 2017. doi: 10.1038/srep43147.

- Marco Stangalini, Robertus Erdélyi, Callum Boocock, David Tsiklauri, Christopher J. Nelson, Dario Del Moro, Francesco Berrilli, and Marianna B. Korsós. Torsional oscillations within a magnetic pore in the solar photosphere. Nature Astronomy, May 2021. doi: 10.1038/s41550-021-01354-8.
- J. O. Stenflo. Magnetic-Field Structure of the Photospheric Network. SoPh, 32(1):41–63, September 1973. doi: 10.1007/BF00152728.
- A. C. Sterling and J. V. Hollweg. Alfvénic resonances on solar spicules. Astrophysical Journal, 285:843–850, October 1984. doi: 10.1086/162563.
- Alphonse C. Sterling. Solar Spicules: A Review of Recent Models and Targets for Future Observations - (Invited Review). SoPh, 196(1):79–111, September 2000. doi: 10.1023/A:1005213923962.
- Y. Suematsu. Numerical Hydrodynamic Simulations of Spicules. In F. Moriyama and J. C. Henoux, editors, Japan-France Seminar on Solar Physics, page 66. Tokyo Astronomical Observatory, The University of Tokyo, January 1980.
- Y. Taroyan and R. Erdélyi. Heating Diagnostics with MHD Waves. SSRv, 149(1-4):229–254, December 2009. doi: 10.1007/s11214-009-9506-9.
- S. Tomczyk, S. W. McIntosh, S. L. Keil, P. G. Judge, T. Schad, D. H. Seeley, and J. Edmondson. Alfvén Waves in the Solar Corona. Science, 317(5842):1192, August 2007. doi: 10.1126/science.1143304.
- Y. Tsap and Y. Kopylova. On the Reflection of Torsional Alfvén Waves from the Solar Transition Region. Solar Physics, 296(5), January 2021. doi: 10.1007/s11207-020-01753-6.
- G. Tsiropoula and K. Tziotziou. The role of chromospheric mot-tles in the mass balance and heating of the solar atmosphere. Astronomy and Astrophysics, 424:279–288, September 2004. doi: 10.1051/0004-6361:20035794.

- G. Tsiropoula, K. Tziotziou, I. Kontogiannis, M. S. Madjarska, J. G. Doyle, and Y. Suematsu. Solar Fine-Scale Structures. I. Spicules and Other Small-Scale, Jet-Like Events at the Chromospheric Level: Observations and Physical Parameters. *SSRv*, 169(1-4):181–244, September 2012. doi: 10.1007/s11214-012-9920-2.
- A. A. van Ballegooijen, M. Asgari-Targhi, S. R. Cranmer, and E. E. DeLuca. Heating of the Solar Chromosphere and Corona by Alfvén Wave Turbulence. *Astrophysical Journal*, 736(1):3, July 2011. doi: 10.1088/0004-637X/736/1/3.
- Santiago Vargas Domínguez and Dominik Utz. Interaction of convective plasma and small-scale magnetic fields in the lower solar atmosphere. *Reviews of Modern Plasma Physics*, 6(1):33, December 2022. doi: 10.1007/s41614-022-00094-0.
- J. E. Vernazza, E. H. Avrett, and R. Loeser. Structure of the solar chromosphere. III. Models of the EUV brightness components of the quiet sun. *Astrophysical Journal, Supplement*, 45:635–725, April 1981. doi: 10.1086/190731.
- Jorge E. Vernazza, Eugene H. Avrett, and Rudolf Loeser. Structure of the Solar Chromosphere. Basic Computations and Summary of the Results. *Astrophysical Journal*, 184:605–632, September 1973. doi: 10.1086/152353.
- E. Verwichte, V. M. Nakariakov, and A. W. Longbottom. On the evolution of a nonlinear Alfvén pulse. *Journal of Plasma Physics*, 62(2):219–232, August 1999. doi: 10.1017/S0022377899007771.
- Yi Wang, Robert W. Noyes, Theodore D. Tarbell, and Alan M. Title. Vorticity and Divergence in the Solar Photosphere. *Astrophysical Journal*, 447: 419, July 1995. doi: 10.1086/175886.
- S. Wedemeyer-Böhm and L. Rouppe van der Voort. Small-scale swirl events in the quiet Sun chromosphere. *Astronomy and Astrophysics*, 507(1):L9–L12, November 2009. doi: 10.1051/0004-6361/200913380.

- Sven Wedemeyer-Böhm, Eamon Scullion, Oskar Steiner, Luc Rouppe van der Voort, Jaime de La Cruz Rodriguez, Viktor Fedun, and Robert Erdélyi. Magnetic tornadoes as energy channels into the solar corona. *Nature*, 486 (7404):505–508, June 2012. doi: 10.1038/nature11202.
- G. L. Withbroe, D. T. Jaffe, P. V. Foukal, M. C. E. Huber, R. W. Noyes, E. M. Reeves, E. J. Schmahl, J. G. Timothy, and J. E. Vernazza. Extreme-ultraviolet transients observed at the solar pole. *Astrophysical Journal*, 203:528–532, January 1976. doi: 10.1086/154108.
- George L. Withbroe and Robert W. Noyes. Mass and energy flow in the solar chromosphere and corona. *Annual Review of Astronomy and Astrophysics*, 15(1):363–387, 1977. doi: 10.1146/annurev.aa.15.090177.002051. URL <https://doi.org/10.1146/annurev.aa.15.090177.002051>.
- N. Yadav, R. H. Cameron, and S. K. Solanki. Vortex flow properties in simulations of solar plage region: Evidence for their role in chromospheric heating. *Astronomy and Astrophysics*, 645:A3, January 2021. doi: 10.1051/0004-6361/202038965.
- T. V. Zaqarashvili and R. Erdélyi. Oscillations and Waves in Solar Spicules. *SSRv*, 149(1-4):355–388, December 2009. doi: 10.1007/s11214-009-9549-y.
- Y. Z. Zhang, K. Shibata, J. X. Wang, X. J. Mao, T. Matsumoto, Y. Liu, and J. T. Su. Revision of Solar Spicule Classification. *Astrophysical Journal*, 750(1):16, May 2012. doi: 10.1088/0004-637X/750/1/16.
- J. B. Zirker. Coronal Heating. *SoPh*, 148(1):43–60, November 1993. doi: 10.1007/BF00675534.